Quantum Mechanics Studies of Fuel Cell Catalysts and Proton Conducting Ceramics with Validation by Experiment

Thesis by
Ho-Cheng Tsai

In Partial Fulfillment of the Requirements for the degree
of
Doctor of Philosophy

CALIFORNIA INSTITUTE OF TECHNOLOGY
Pasadena, California
2015
(Defended April 20, 2015)

ACKNOWLEDGEMENTS

First, I would like to express my deep appreciation for my advisor, Prof. William A. Goddard III, for his guidance in the past 5 years at Caltech. His generosity and great patience gave me the best support during my academic career; his intelligence and brilliance always pointed in another direction away from the depression and maze that I encountered, and reinflamed my enthusiasm for research. I could not even image how I could complete my PhD degree without his kind help and wise suggestions. He made my PhD study a pleasurable period and I will never forget my life at Caltech.

I would also like to acknowledge our Materials and Process Simulation Center (MSC) fuel-cell subgroup director, Dr. Boris. V Merinov, for his extensive help in progress discussion, manuscript revision, and project collaboration. He also taught me how to respond to the stringent reviewers' questions and always be confident to myself. I am so lucky to have had such a nice team leader and to have worked with him for the past five years.

I would like to express my gratitude to my mentor, Prof. Ted H. Yu. His step-by-step teaching of how to use computation software helped me transfer from an experimentalist to a computational theorist. His selfless sharing of his experiences, scripts, data, and related literatures also saved me a lot of time. We now have three joint publication but I believe that there will be more in the future. In addition, I also want to thank the MSC colleagues, especially Dr. Hai Xiao, Dr. Qi An, Dr. Tao Chen, Dr. Wei-Guang Liu, Dr. Mu-Jeng Cheng, Dr. Yao Sha, Mr. Fan Liu, and Mrs. Shirley Wu, for their counsel and help.

I would like to thank my scholarship from the ministry of education, Taiwan. With this financial help, I could complete my dreams of studying abroad at one of the top universities in the world. The project funding from Ford, Samsung, National Science Foundation (NSF), National Science Council (NSC at Taiwan), Defense Advanced Research Projects Agency (DARPPA) is also appreciated. My thanks for our collaborators, Dr. Yu-Chi Hsieh, Mr. Yi-Juey Lee, Dr. Yue-Han Wu, Prof. Pu-Wei Wu, Prof. San-Yuan Chen, Prof. Chia-Ming Yang, Dr. Chih-Kai Yang, Dr. Hays, and Dr. Pezhman Shirvanian for discussions and experiment help. My thanks also to Prof. Morozov at South Ural State University for the powerful supercomputers which speeded up our calculations. And thanks to Dr. Peter A. Schultz at Sandia National Laboratories for helping solve Seqquest related issues.

I would like to thank my thesis committee, Prof. Harry B. Gray, Prof. William L. Johnson, and Prof. Sossina M. Haile. It's my honor to have the top scientists as my thesis committee and to give me advice.

My thanks to my roommate and classmates, Hsieh-Chen Tsai, Wen-Hao Lee, Chun-Jen Hsueh,

Tiffany Wang, Yinglu Tang, Yulia Tolstova, Min-Feng Tu, and Yu-Hung Lai. Solving problem sets with you guys together is my most miserable but unforgettable memory at Caltech. Also, my thanks to the Association of Caltech Taiwanese (ACT) friends. My life at Caltech became much easier and more fun with your company.

Last but not least, I would like to thank my family and also the love of my life, Yingying. Because of your support and devotion, I could be completely involved in my research and study for the past five years.

ABSTRACT

We carried out quantum mechanics (QM) studies aimed at improving the performance of hydrogen fuel cells. This led to predictions of improved materials, some of which were subsequently validated with experiments by our collaborators.

In part I, The challenge was to find a replacement for the Pt cathode that would lead to improved performance for the Oxygen Reduction Reaction (ORR) while remaining stable under operational conditions and decreasing cost. Our design strategy was to find an alloy with composition Pt_3M that would lead to surface segregation such that the top layer would be pure Pt, with the second and subsequent layers richer in M. Under operating conditions we expect the surface to have significant O and/or OH chemisorbed on the surface, and hence we searched for M that would remain segregated under these conditions. Using QM we examined surface segregation for 28 Pt_3M alloys, where M is a transition metal. We found that only Pt_3Os and Pt_3Ir showed significant surface segregation when O and OH are chemisorbed on the catalyst surfaces. This result indicates that Pt_3Os and Pt3Ir favor formation of a Pt-skin surface layer structure that would resist the acidic electrolyte corrosion during fuel cell operation environments. We chose to focus on Os because the phase diagram for Pt-Ir indicated that Pt-Ir could not form a homogeneous alloy at lower temperature. To determine the performance for ORR, we used QM to examine all intermediates, reaction pathways, and reaction barriers involved in the processes for which protons from the anode reactions react with O_2 to form H_2O. These QM calculations used our Poisson-Boltzmann implicit solvation model include the effects of the solvent (water with dielectric constant 78 with pH 7 at 298K). We found that the rate determination step (RDS) was the O_{ad} hydration reaction ($O_{ad} + H_2O_{ad} \rightarrow OH_{ad} + OH_{ad}$) in both cases, but that the barrier for pure Pt of 0.50 eV is reduced to 0.48 eV for Pt_3Os, which at $80^{O}C$ would increase the rate by 218%. We collaborated with the Pu-Wei Wu's group to carry out experiments, where we found that the dealloying process-treated Pt_2Os catalyst showed two-fold higher activity at

$25^{O}C$ than pure Pt and that the alloy had 272% improved stability, validating our theoretical predictions.

We also carried out similar QM studies followed by experimental validation for the Os/Pt core-shell catalyst fabricated by the underpotential deposition (UPD) method. The QM results indicated that the RDS for ORR is a compromise between the OOH formation step (0.37 eV for Pt, 0.23 eV for Pt_{2ML}/Os core-shell) and H_2O formation steps (0.32 eV for Pt, 0.22 eV for Pt_{2ML}/Os core-shell). We found that Pt_{2ML}/Os has the highest activity (compared to pure Pt and to the Pt_3Os alloy) because the 0.37 eV barrier decreases to 0.23 eV. To understand what aspects of the core shell structure lead to this improved performance, we considered the effect on ORR of compressing the alloy slab to the dimensions of pure Pt. However this had little effect, with the same RDS barrier 0.37 eV. This shows that the ligand effect (the electronic structure modification resulting from the Os substrate) plays a more important role than the strain effect, and is responsible for the improved activity of the core-shell catalyst. Experimental materials characterization proves the core-shell feature of our catalyst. The electrochemical experiment for Pt_{2ML}/Os/C showed 3.5 to 5 times better ORR activity at 0.9V (vs. NHE) in 0.1M $HClO_4$ solution at $25^{O}C$ as compared to those of commercially available Pt/C. The excellent correlation between experimental half potential and the OH binding energies and RDS barriers validate the feasibility of predicting catalyst activity using QM calculation and a simple Langmuir–Hinshelwood model.

In part II, we used QM calculations to study methane stream reforming on a Ni-alloy catalyst surfaces for solid oxide fuel cell (SOFC) application. SOFC has wide fuel adaptability but the coking and sulfur poisoning will reduce its stability. Experimental results suggested that the Ni_4Fe alloy improves both its activity and stability compared to pure Ni. To understand the atomistic origin of this, we carried out QM calculations on surface segregation and found that the most stable configuration for Ni_4Fe has a Fe atom distribution of (0%, 50%, 25%, 25%, 0%) starting at the bottom

layer. We calculated that the binding of C atoms on the Ni_4Fe surface is 142.9 Kcal/mol, which is about 10 Kcal/mol weaker compared to the pure Ni surface. This weaker C binding energy is expected to make coke formation less favorable, explaining why Ni_4Fe has better coking resistance. This result confirms the experimental observation. The reaction energy barriers for CH_x decomposition and C binding on various alloy surface, Ni_4X (X=Fe, Co, Mn, and Mo), showed Ni_4Fe, Ni_4Co, and Fe_4Mn all have better coking resistance than pure Ni, but that only Ni_4Fe and Fe_4Mn have (slightly) improved activity compared to pure Ni.

In part III, we used QM to examine the proton transport in doped perovskite-ceramics. Here we used a 2x2x2 supercell of perovskite with composition $Ba_8X_7M_1(OH)_1O_{23}$ where X=Ce or Zr and M=Y, Gd, or Dy. Thus in each case a 4^+ X is replace by a 3^+ M plus a proton on one O. Here we predicted the barriers for proton diffusion allowing both includes intra-octahedron and inter-octahedra proton transfer. Without any restriction, we only observed the inter-octahedra proton transfer with similar energy barrier as previous computational work but 0.2 eV higher than experimental result for Y doped zirconate. For one restriction in our calculations is that the O_{donor}-$O_{acceptor}$ atoms were kept at fixed distances, we found that the barrier difference between cerates/zirconates with various dopants are only 0.02~0.03 eV. To fully address performance one would need to examine proton transfer at grain boundaries, which will require larger scale ReaxFF reactive dynamics for systems with millions of atoms. The QM calculations used here will be used to train the ReaxFF force field.

TABLE OF CONTENTS

Section I

DFT Study of ORR on Pt-Os Catalyst Surfaces Validated by Experiment

Chapter 1

Introduction

A proton exchange membrane fuel cell (PEMFC) is considered to be a potential technology for use in automotive applications, stationary/portable power supply, and as a part of hybrid energy systems[1-4] due to its low pollution emission and high efficiency advantages compared to currently used petroleum-based energy production.[1,2,5] However, the PEMFC performance is limited by the sluggish oxygen reduction reaction (ORR) at cathode,[6-8] which is much slower and more complicated than the hydrogen oxidation reaction (HOR) at anode.[8]

ORR mechanisms and electronic structures of ORR catalysts are widely discussed in the literature. For example, Hammer and Nørskov discussed the surface catalysis by considering the interaction between local density of states of adsorbates and d-bands of surfaces.[9] A similar d-band center theory was used by Xin et al. to screen potential alloy catalysts for ORR.[10,11] Holewinski and Linic applied DFT to simulate the OH/H_2O surface coverage and explained the deviation from ideal Tafel kinetics by microkinetic modeling.[12] Similar microkinetic modeling starting with surface coverage was used to calculate the ORR mechanism and Tafel kinetics for Pt[13] and surface corrosion and kinetics for the Au-modified Pt system.[14,15] Jacob et al. considered current theoretical methods for surface reaction simulations and performed DFT calculations to elucidate the complex ORR mechanism by different pathways.[16,17]

Various types of cathode catalysts, including Pt-based alloys and non-precious metal catalysts, have been widely studied in the past few years in order to improve the ORR efficiency and reduce the catalyst cost.[2,18-21] For example, Pt based catalysts, which are alloyed with transition elements

such as Ni,[22-25] Co,[22-24] Ti,[22-24] Zr,[22] Y,[22,26] Fe,[23,24] V,[23,24] Sc,[26] and Cu,[27,28] were reported in virtue of better ORR activities than pure Pt. In our previous study,[29] some Pt_3M catalysts, where M is a transition metal, show Pt segregation with formation of so-called Pt-skin on the surface, which improves the catalytic activity of these materials compared to pure Pt.[24] However, it was reported that the components of Pt alloys would be dissolved into electrolyte at the PEMFC operation environment,[30,31] which helps form the Pt-skeleton structure,[32,33] but could possibly deteriorate because of Ostwald ripening or diffusion.[30-33] This would result in descending activity of the catalysts.[31,34-36]

Stabilities of Pt-alloys have been studied by different theoretical and experimental methods. For instance, Ma et al.[37] and Chen et al.[38] carried out DFT studies of the Pt_3M alloy surface segregation with and without adsorbates. Wei et al.[39] evaluated the Pt_xMo alloy stability using DFT to calculate the Gibbs free energy change of the surface corrosion. Nørskov with co-authors[26,40] computed the heat of formation to evaluate the stability of Pt-alloys and verified the stability of Pt_3Y and Pt_3Sc by experiment. The same concept was applied by Hwang et al.[22] to explain the experimental results on the stability of Pt_3M (M=Y, Zr, Ti, Ni, and Co). Dai et al.[41] combined surface segregation, heat of formation, and d-band center shift calculations to show that PtW alloys may have both better activity and superior stability. Pt-skin formed after annealing or Pt-skeleton structures built after acid-treatment or oxide-leaching after ORR cycling are responsible for the improved catalytic activity and long-term stability of the above-mentioned materials.[42-44] Our segregation study of Pt_3M alloy bare surfaces[29] indicates that a few alloys show a good segregation energy favoring the Pt-skin formation. However, the situation may change when the catalyst is under ORR environment and its surface is exposed to ORR adsorbates, such as O or OH. In poorly segregated alloy surfaces, the non-noble metal component may diffuse onto the surface with a risk of leaching out into the electrolyte with subsequent degradation of PEMFC performance. Widely discussed in literature, Pt_3Co, Pt_3Ni, Pt_3Fe

alloys are not stable under the fuel cell conditions and leach out into the electrolytes.[45,46] This experimental observation is supported by a theoretical study[47] as well.

With the potential to reduce the cost, non-precious metal (NPM) catalysts became attractive recently. For example, Bashyam and Zelenay reported a cobalt-polypyrrole-carbon (Co-PPY-C) catalyst;[19] Wu et al. described polyaniline (PANI) derived catalysts.[48] However, the mass transport loss and stability issues are unsatisfactory for NPM catalysts.[21] Therefore, to achieve the desirable high activity, low cost, and durability, new advanced Pt group metal (PGM) ORR catalyst design approaches are still required.[49]

In recent years, core-shell and core-shell-like structures of Pt-based alloys have attracted significant attention due to their much better catalytic activity than pure Pt.[23-26,29,50-64] For example, Yang et al. reported that Ru/Pt core-shell catalyst has ~4 times better activity than pure Pt.[61] The combined experimental and theoretical work of Fribel et al. compared H_{ad} and O/OH_{ad} adsorption on 2D and 3D Pt/Rh(111) surfaces and found that the $H/O/OH_{ad}$ are destabilized in the smooth 2D structure because of the ligand/strain effect of the Rh substrate. However, the geometry effect (both the higher thickness and increased number of defects) balanced the strain/ligand effect and increased the H/O/OH adsorption for the 3D structure derived from the wetting process.[63] Brimaud et al. analyzed the surface character and compared the ORR activity of $Pt_{x\text{-ML}}$/Ru(0001) and Pt_xRu_{1-x}/Ru(0001) with Pt(111) and found that their ORR activity could exceed the pure Pt ORR activity by modifying the Pt surface content of the Pt_xRu_{1-x}/Ru(0001) alloy or adjusting the thickness of the Pt film to the thickness of $Pt_{x\text{-ML}}$/Ru(0001).[62] Jackson et al. used core-shell Ru/Pt as an example to prove the feasibility of improving the activity by tailoring the nanostructure.[64]

To our knowledge, Os and its alloys have rarely been studied as ORR catalysts. Most of the literature on Os and its alloys is focused on methanol[65-70] or formic acid[71] oxidation in fuel cell

systems. Only $Os_{0.2}Pt_{0.8}$/Pd(111) was considered as a possible electrocatalyst for ORR,[72] but the corresponding work does not include a complete report. Therefore, we paid our attention to Pt_3Os as a catalyst because of its good bare surface segregation result,[29] as well as the shorter surface Pt-Pt bond distance, which may reduce the O/OH binding energy due to the strain effect and thus improve its ORR catalytic activity. In addition to the Pt_3Os alloy, a study of the core-shell Os/Pt catalyst was also performed in order to investigate the ORR activity of this catalyst.

In this section, we will discuss our theoretical predictions and experimental validation for the Pt-Os catalysts. All methodologies, including both theoretical and experimental methods, are explained in Chapter 2. The computational study of the Pt_3Os catalyst, our efforts on synthesis of the Pt_3Os catalyst, materials characterization, and electrochemical evaluation are discussed in Chapter 3. Here, we examined the segregation energy for 28 Pt_3M alloys with adsorbed O_{ad} and OH_{ad} on the surface using quantum mechanics (QM) calculations. Looking ahead, we say that our calculations revealed surface segregation to become energetically unfavorable for Pt_3Co and Pt_3Ni, as well as for most other Pt binary alloys, in the presence of adsorbed O_{ad} and OH_{ad}. However, Pt_3Os and Pt_3Ir remain surface segregated and show the best energy preference among the alloys studied for both adsorbed species on the surface. PtIr materials have been studied earlier (see, for instance, Refs 73, 74), and Ir could not mix Pt well to form a homogeneous alloy at lower temperature. Therefore we selected the Pt_3Os system for further theoretical investigation. Binding energies of various ORR intermediates and reaction energy barriers for various pathways of different ORR mechanisms on the $Pt_3Os(111)$ surface were calculated, analyzed, and discussed. Furthermore, our collaborators synthesized the Pt-Os catalyst by using the dealloying process, and performed materials characterization and electrochemical evaluation.

In Chapter 4, our QM calculations on periodic slabs to predict catalytic activity of the Os/Pt core-shell catalysts are analyzed. Perfect hcp (0001) and fcc (111) slabs were applied for Os, Pt, and Pt/Os surfaces. Full kinetic modeling of complex reactions, such as ORR, on nanoparticles still remains a challenge for atomistic first-principles simulations. Although a slab model applied in our calculations is mostly relevant for extended surfaces and neglects natural strain, morphology, or any defects such as edge and kink sites, multiple terraces and corners, and other peculiarities observed in nanoparticles, several fundamental issues of the surface ORR can be analyzed using the methodology applied, because the highly coordinated (111) facets are most conducive to the ORR on small nanoparticles.[75] Although the above-mentioned features of nanoparticles may change binding energies of the ORR intermediates and reaction barriers compared to those on extended surfaces, the slab approach is still sufficient enough to predict ORR trends. Moreover, reported experimental results indicate that the higher catalytic activity of Pt_3M alloy extended surfaces compared to that of Pt is reproduced qualitatively on surfaces of Pt_3M alloy nanoparticles.[76-81] To validate our theoretical predictions, we used the UPD method for the core-shell catalyst fabrication[49,55,76-81] with succeeding analysis of ORR activity of the fabricated Os/Pt core-shell catalysts.

Conclusions are in Chapter 5.

Chapter 2

Methodology

2.1 Computational

In our theoretical study, we used QM calculations to investigate surface metal segregation, unique binding-site preferences due to the placement of sublayer alloying atoms for all intermediates involved in the ORR on the Pt, $Pt_3Os(111)$, and Os(0001)/Pt surfaces, and the consequent changes in the reaction barriers and ORR mechanisms.

All QM calculations were carried out using the SeqQuest software[82] with optimized double zeta plus polarization quality Gaussian-type orbitals and the Perdew-Becke-Ernzehof (PBE)[83] functional of DFT in the generalized gradient approximation (GGA).[84,85] Small core Norm-conserving angular momentum projected pseudopotentials[86-90] were employed in our calculations. All calculations were performed with spin optimization. The reciprocal space grid was 5×5×0 for the slab calculations and 12×12×12 for the bulk lattice constant calculations. We used 4 layer 2×2 cell slabs for the alloy segregation study, while 6 layer 2×2 Pt_3Os cell slabs were applied for the binding energy and most reaction barrier calculations. Therefore, each layer contains 4 atoms and the surface coverage is ~1/4. We consider the 1/4 coverage to be large enough to avoid irrelevant cross cell interaction, while still keeping the unique properties of the segregated Pt_3Os surface. For the O hydration step, 3×3 and 2×4 cell slabs were used for Pt and Pt_3Os, respectively, to avoid artificial hydrogen bonding. The periodic cell parameter of the slab corresponds to that of the optimized Pt_3Os bulk structure with the lattice

constant of 3.94 Å, slightly smaller than 3.98 Å for Pt. All charges were obtained from the Mulliken population analysis.

For Os/Pt core-shell catalysts, a 3×3 supercell (9 atoms per layer) with 3 to 5 layer Os slabs were used as the core structure. 1 to 3 additional layers of Pt atoms on this core structure (the total number of layers in all slabs was 6) were used to simulate the Os/Pt core-shell catalyst structures. In all calculations, we fixed the coordinates of 9 Os atoms in the bottom layer and relax all other atoms in the geometry optimization. For comparison, similar calculations were carried out on 6 layer Pt and Os slabs. The obtained Os-Os and Pt-Pt bond lengths are 2.75 and 2.81 Å, respectively. We used the lowest-energy surfaces in our calculations: the (0001) surface of the hexagonal closed-packed (hcp) structure for Os and the (111) surface of the face-centered cubic (fcc) structure for Pt.

To represent the effects of solvent polarization, an implicit model[91] based on the Poisson-Boltzmann approximation was applied.[92-94] We showed that our implicit solvation model correctly reproduces the solvation energies of O_{ad}, H_{ad}, OH_{ad}, and H_2O_{ad} calculated using explicit water layers.[91] The Mulliken charges were used as inputs to our solvation model.

The binding energies (BE) are calculated as the energy gain for species to adsorb to the surface, i.e.,

$$BE_{gas} = E_{surf + A, gas} - E_{surf, gas} - E_{A, gas}$$

where A is an adsorbate. For the solution phase, the solvent stabilization is added directly to the binding energy in order to isolate the influence of water. This leads to

$$BE_{solv} = E_{surf + A, solv} - E_{surf, solv} - E_{A, gas}$$

The solvent phase binding energy does not include the solvent effect of the adsorbate itself, because most of the species are radicals that do not have well-defined solvation energies for comparison. The lack of these energy data for radical species does not affect the barrier calculations since the reactants, products, and transition states are all surface species and the differences in individual solvation energies eventually cancel out.

All barriers are calculated as the energy difference between a transition state and surface reactant sites, using the nudged elastic band (NEB) method.[95,96] We disregard the energy that reactants need to migrate from the globally preferred sites to the reacting sites, as these barriers would correspond only to very low surface coverage. This condition is not typical for the conventional fuel cell operation. However, to avoid misunderstanding and show certain details of the ORR mechanism, the spontaneous O migration step has been added to some of our figures, representing possible ORR mechanisms. While both Langmuir–Hinshelwood and Eley–Rideal mechanisms (see, for instance, Refs 97, 98) may occur in ORR at electrode potentials near 1.23 eV (the reduction potential of the ORR established by the Nernst equation),[99] our Os/Pt core-shell computation results confirmed that the conclusions derived from Langmuir-Hinshelwood type reactions are similar to the ones derived from Eley–Rideal mechanisms.

In our calculations, zero point energy (ZPE) and entropy contributions were neglected, because our conclusions about ORR activity are based on the rate-determining step (RDS) barriers, which are energy differences between transition states and initial states. In this case, the above-mentioned contributions may be cancelled.

2.2 Experimental Section for Dealloyed Pt_2Os Catalyst

2.2.1 *Pt_2Os Synthesis*

Carbon-supported Pt_2Os nanoparticles were prepared in a chemical reduction route. First, 80 mg of carbon powders (particle size <50 nm, Sigma Aldrich) were suspended in 50 mL of deionized water at 80 °C. Next, 36 mg of $H_2PtCl_6 \cdot 6H_2O$ (UniRegion Bio-Tech) and 17 mg of K_2OsCl_6 (Sigma-Aldrich) were dissolved in 50 mL of deionized water (molar ratio of Pt/Os = 2), and the solution was added to the carbon suspension. Subsequently, 21 mg of citric acid was added as a chelating agent. The mixture was stirred for 30 min at 80 °C in an argon flow under reflux to produce a homogeneous suspension. Afterward, 76 mg of $NaBH_4$ was added to serve as a reducing agent, and the mixture underwent further stirring for 2 hr at 80 °C in an argon flow under reflux to ensure the complete reduction of Pt and Os ions, and the formation of Pt_2Os nanoparticles impregnated on the carbon powders. The as-synthesized sample was labeled as Pt_2Os/C. Next, the Pt_2Os/C powders were filtered and washed to remove residual chloride ions. After drying at 25 °C in air for 8 hr, a reduction treatment at 250 °C in a hydrogen flow (100% H_2) was performed for 2 hr. The effective metal loading of the Pt_2Os nanoparticles was 20 wt% of the Pt_2Os/C sample.

2.2.2 *Electrochemical Analysis*

10 mg of Pt_2Os/C powders underwent an ultrasonication mixing for 5 min in a solution containing 3 mL of deionized water, 2 mL of ethanol, and 2 μL of 5 wt% Nafion ionomer solution (Sigma-Aldrich) to render a uniform ink dispersion. Subsequently, 15 μL of the ink dispersion was deposited on a glassy-carbon rotation disk electrode (RDE) serving as a working electrode (Pine Research, electrode diameter is 5 mm and the electrode area is 0.1963 cm^2). To initiate the selective

dissolution of Os atoms from the Pt_2Os nanoparticles, known as a dealloying process, multiple cyclic voltammetry (CV) scans were imposed between -0.2 and 0.8 V at 50 mV s^{-1} in 50 mL of deaerated 0.1 M aqueous $HClO_4$ solution. After the dealloying process, the sample was labeled as DA-Pt_2Os/C. The coulombic charge associated with the hydrogen underpotential deposition region (-0.2 to 0.2 V vs. Ag/AgCl) was estimated and divided by 210 μC cm_{Pt}^{-2} [100,101] to obtain the electrochemical active surface area (ECSA) for the Pt_2Os/C and DA-Pt_2Os/C. To explore the electrocatalytic activities for ORR, CV scans between -0.2 and 0.8 V were performed at 10 mV s^{-1} in 50 mL of 0.1 M aqueous $HClO_4$ solution. Prior to the ORR experiments, the $HClO_4$ aqueous solution was bubbled with oxygen for 30 min to ensure it was fully saturated with the oxygen. Durability tests were performed using CV scans at 50 mV s^{-1} between 0.36 and 0.76 V in 50 mL of 0.1 M aqueous $HClO_4$ solution. The durability test lasted for 10,000 cycles and the electrolyte was exposed to the ambient air throughout the entire cycles. The electrochemical measurements were performed at 25 °C in a three-electrode arrangement using a Solartron 1287A electrochemical interface. A Ag/AgCl and Pt foil (15 cm^2) were used as the reference and counter electrodes, respectively. The potential for the reversible hydrogen electrode (RHE) was -0.289 V (vs. Ag/AgCl). In our figures, all potentials were plotted against the RHE. Lastly, identical electrochemical tests were performed on commercially available Pt/C (20 wt% Pt on Vulcan XC72R, BASF) for comparison purposes.

2.2.3 *Materials Characterization*

A high-resolution transmission electron microscope (HRTEM; JEOL JEM3000F) was employed to observe the morphologies, sizes, and distributions of the Pt_2Os/C and DA-Pt_2Os/C. The structures and composition profiles of the Pt_2Os and DA-Pt_2Os nanoparticles were obtained

using a JEOL spherical aberration corrected scanning transmission electron microscope (ARM 200F) with an Oxford energy dispersive spectrometer (EDS) in which the L_α and M_α signals from the EDS were recorded to determine the spatial distribution of the Pt and Os atoms in the Pt_2Os and DA-Pt_2Os nanoparticles. A scanning electron microscope (SEM; JEOL JSM6500F) and a total reflection X-ray fluorescence spectrometer (TRXF; Bruker S2-PICOFOX) were employed to estimate the atomic ratio of Pt/Os in the Pt_2Os and DA-Pt_2Os nanoparticles. The exact Pt amount in our samples was determined using an inductively coupled plasma mass spectrometer (ICP-MS; Agilent 7500ce). An X-ray diffractometer (XRD; Bruker D2 Phaser) equipped with a Cu Kα radiation source (λ =1.54 Å) was used to identify relevant phases and crystal sizes for both Pt_2Os/C and DA-Pt_2Os/C.

2.3 Experimental Section for Os/Pt Core-Shell Catalysts

2.3.1 *Os Synthesis*

Carbon-supported Os nanoparticles (Os/C) were prepared in a chemical reduction route. First, 50 mg of carbon powders (Ketjen Black) and 19.5 mg of $OsCl_3$ were mixed in 100 mL of ethanol at 25°C. Next, the temperature of the mixture was raised to 110°C for 2 hr to reach a uniform dispersion. Subsequently, 2.63 ml of 100 mM aqueous KOH solution was added. The mixture underwent further stirring for 30 min and cooled to 25°C to filter out the Os/C. The dried Os/C was subjected to a reduction treatment at 450°C for 1 hr in an atmosphere of 15% H_2 and 85% Ar. The effective metal loading of the Os nanoparticles was 20 wt% of the Os/C sample.

2.3.2 *Preparation of Os/Pt Core-Shell Nanoparticles*

We used the UPD method to prepare Os/Pt core-shell nanoparticles. In this method, a monolayer of a sacrificial metal is deposited on the substrate at a potential which is more positive than the reduction potential. Then a more noble metal substitutes the sacrificial metal using galvanic displacement.

5 mg of Os/C powders underwent an ultrasonication mixing for 5 min in a solution containing 5 mL of ethanol, and 1 μL of 5 wt% Nafion ionomer solution (Sigma-Aldrich) to render homogeneous ink dispersion. Next, 15 μL of the ink dispersion was deposited on a glassy-carbon rotation disk electrode (RDE) serving as a working electrode (Pine Research, electrode diameter is 5 mm and the electrode area is 0.1963 cm^2). Subsequently, the working electrode was immersed in a deaerated aqueous solution of 50 mM $CuSO_4$ and 50 mM H_2SO_4 for 20 CV scans with a scan rate of 20 mV/s in a potential window of 0.31 and 0.9 V (vs. RHE). The purpose for these CV scans was to precondition the sample and identify the suitable potential for the Cu UPD process. Afterward, a Cu UPD was imposed in which the potential was kept at 0.35 V to allow the Cu to deposit onto the surface of the Os nanoparticles as a monolayered film. Once the depositing current was subdued and stabilized, the sample was removed from the Cu plating solution and immersed immediately in a deaerated aqueous solution containing 1 mM K_2PtCl_4 and 50 mM H_2SO_4. At this stage, a displacement reaction took place in which the Cu atoms on the Os surface were oxidatively dissolved whereas the Pt ions in the electrolyte were reduced and deposited onto the Os nanoparticles. The sample undergoing a single Cu-UPD/displacement reaction cycle was labeled Pt_{1ML}/Os/C and the sample undergoing consecutive Cu-UPD/displacement reaction cycles was labeled Pt_{2ML}/Os/C. We should emphasize here that Pt_{1ML}/Os/C does not necessarily mean a completely perfect Pt monolayer

deposited on the Os substrate; more details are reported in Chapter 4. The Os/Pt core-shell catalysts production procedure is summarized in Figure 1.

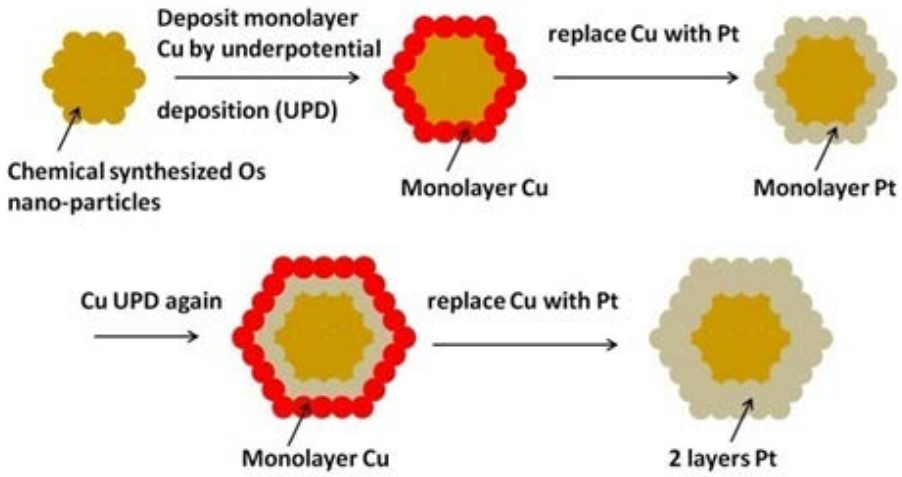

Figure 1. The procedure for Os/Pt core-shell catalyst preparation.

To determine the ECSA, multiple CV scans were imposed between 0.05 and 1.0 V (vs. RHE) at 20 mV/s in a 50 mL of deaerated 0.1 M aqueous $HClO_4$ solution. The Coulomb charge associated with the hydrogen adsorption was integrated and divided by 210 μC cm_{Pt}^{-2} to obtain the ECSA value for the Pt/C, Pt_{1ML}/Os/C, and Pt_{2ML}/Os/C, respectively. To explore the electrocatalytic activities for the ORR, CV scans between 0.1 and 1.05 V (vs. RHE) were performed at 20 mV/s in 50 mL of 0.1 M aqueous $HClO_4$ solution. Prior to the ORR experiments, the $HClO_4$ aqueous solution was bubbled with oxygen for 30 min to ensure it was fully saturated with the oxygen. The electrochemical synthesis and ORR measurements were performed at 25°C in a three-electrode arrangement using a Solartron 1287A electrochemical interface. Ag/AgCl and Pt foils (15 cm^2) were used as the reference and counter electrodes, respectively. In our figures, all potentials were plotted against the RHE.

Lastly, identical electrochemical tests were performed on commercially available carbon-supported Pt (Pt/C; 20 wt% Pt on Vulcan XC72R, BASF) for comparison purposes.

2.3.3 *Materials Characterization*

HRTEM (JEOL JEM3000F) and high angle angular dark field (HAADF) techniques were employed to observe the morphologies, sizes, and distributions of the Os nanoparticles. The structures and composition profiles of Pt_{1ML}/Os/C and Pt_{2ML}/Os/C were obtained using a JEOL spherical aberration corrected scanning transmission electron microscope (ARM 200F) with an Oxford EDS in which the Lα and Mα signals from the EDS were recorded to determine the spatial distribution of the Pt and Os atoms. The exact Pt amount in our samples was determined using an ICP-MS (Agilent 7500ce).

Chapter 3

Results and Discussion for Pt_3Os Catalyst

3.1 Surface Segregation Effect

We have performed QM calculations to examine 28 Pt binary alloys and identify good segregating alloys that maintain the favorable segregating property when the oxidative species, O_{ad} and OH_{ad}, are adsorbed on the surface. For calculating the segregation energy, we used the lowest energy O_{ad} and OH_{ad} surface binding sites from our previous Pt_3Ni study.[59]

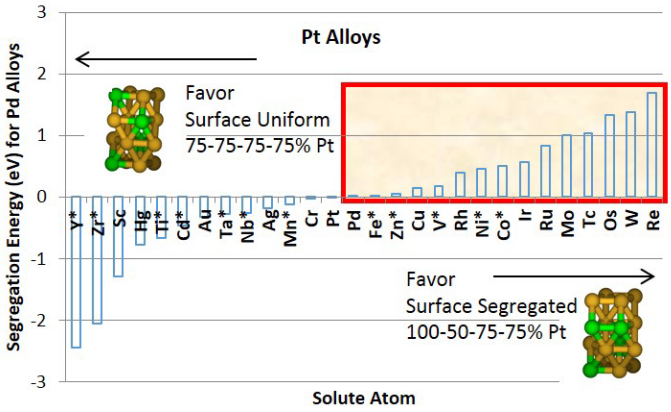

Figure 2. Surface segregation of Pt_3M binary alloys.[29]

Figure 2 summarizes our previous bare surface segregation calculations for Pt_3M alloys.[29] The results showed that Re, W, Os, Tc, Mo, Ru, Ir, Co, Ni, Rh, V, Cu, Zn, Fe, and Pd could form surface segregated Pt_3M alloys. Figure 3 displays the segregation energy of the different alloy catalysts with adsorbed O_{ad} and OH_{ad} on the surface. In case of OH adsorbed on the surface, six solute metals, showing favorable segregation energies for the corresponding Pt_3M alloys, are Os, Re, Ir, Ru, Tc, and Rh. For the O_{ad} adsorbed surface, only two solute metals, Ir and Os, show favorable segregation energies. All of these solute metals are considered difficult to oxidize and have more positive reduction potential versus hydrogen. All but one (Tc) are considered noble metals. As a general rule, segregation becomes unfavorable when O_{ad} and OH_{ad} are adsorbed on a metal which is easily oxidized.

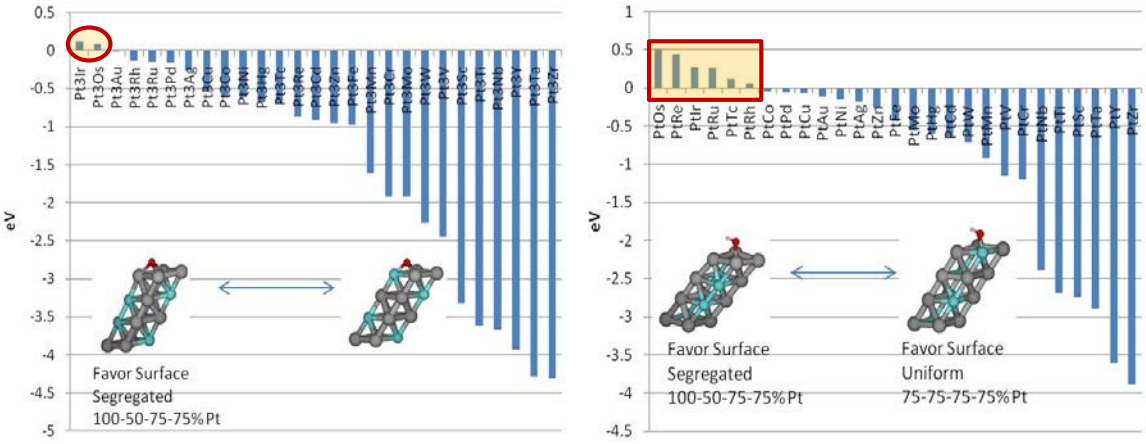

Figure 3. Surface segregation energy with adsorbed O (left) and OH (right).

The segregation energy can vary significantly when O_{ad} or OH_{ad} is adsorbed on the surface. For example, without adsorbed species, the best five segregation energies were Pt alloyed with Re, W, Os, Tc, and Mo.[29] However, the segregation energy of Pt_3W and Pt_3Mo changes from strongly

favorable to strongly unfavorable with adsorbed O_{ad} and OH_{ad}, as both W and Mo are known to easily react to form oxides. Our segregation result is consistent with results of other theoretical investigations, in which a similar approach was used to study some Pt-based alloy and core-shell catalysts,[73,74] as well as with the experimental results obtained by Abrams et al. for Pt deposit on the Au foil.[102] They found that the Au atoms migrated to the surface because of a lower Au surface energy. However, exposing the sample to air makes the deactivated sample become partially reactive again. This reactivation was ascribed to the adsorbed O from the air, which favor the Pt to segregate back to the surface (adsorbate-induced surface segregation). Our calculation on the Pt_3Au alloy also indicates that Pt shows better segregation property with adsorbed O on the surface (see Figure 3). We found only a few Pt binary alloys with favorable surface segregation energy in the presence of adsorbed O_{ad} or OH_{ad}. Out of them, only Pt_3Os and Pt_3Ir show surface segregation in the presence of both adsorbed species. Therefore, these alloys are predicted to be more resistant to solute metal leaching than Pt_3Co or Pt_3Ni. However, according to the Pt-Os phase diagram,[103] only 20% Os can be mixed into the Pt structure, whereas Ir cannot be mixed into the Pt structure at all.[104] Despite this disappointing information, synthesis of Pt-Os nanoparticles even with the molar ratio of 1:1[105] and PtIr nanoparticles with the molar ratio of 3:1[58,106] were reported. In this study, we carried out computations of binding energies and energy barriers of the ORR intermediates on the $Pt_3Os(111)$ alloy surface.

3.2 Binding Energy of ORR Intermediates

3.2.1 *Binding Site Notation*

Generally, the closest packed (111) surface of fcc structured metals has four types of sites:

1. On-top, bonded to one Pt (μ_1), denoted as t,
2. Bridging, between two Pt μ_2), denoted as b,
3. Bridging, between three Pt (μ_3-fcc) but in the fcc position (not above atoms of the top or second layer), denoted as f, and
4. Bridging, between three Pt (μ_3-hcp) but in the hcp position (above atoms of the second layer), denoted as h.

However, due to strong segregation, the Pt_3Os(111) surface has 100% Pt in the first layer, 50% Os and 50% Pt in the second layer, and 25% Os and 75% Pt in the four remaining layers. We find that the binding energies of the ORR intermediates to the pure Pt layer strongly depend on the nature of the second layer atoms. Figure 4 shows notations of these sites and details of the differences between various sites.

For the first and second layers, there are two types of top sites: t_1 with one Os neighbor in the second layer and t_2 with two Os neighbors. Considering also the third layer, we can distinguish t_{1a} with no Os in the third layer directly beneath the surface and t_{1b} with one Os. All t_2 sites are the same (see Figure 4).

For the top two layers, there are four μ_2 bridge sites, depending on the number of Os atoms underneath: b_0, b_1, b_2, and b_3 with 0, 1, 2, and 3 Os atoms in the second layer. When the third layer

is added, there appear two subtypes for b_1, b_2, and b_3, depending on the distance to the Os atom in the third layer. We denote the subtypes closer to the third layer Os as b_{1a}, b_{2a}, and b_{3a}, and the others as b_{1b}, b_{2b}, and b_{3b}, respectively (Figure 4).

When we consider only the top two layers, two fcc sites can be distinguished, f_1 and f_2, with one and two Os atoms in the sublayer triangle, but adding the third layer splits f_1 into f_{1a} and f_{1b} with f_{1a} on top of the third layer Os and f_{1b} on top of the third layer Pt.

Similarly, there are two hcp sites related to the two top layers: h_1 and h_2. Here h_1 is on top of the Os sublayer, while h_2 is on top of the Pt sublayer. Adding the third layer splits the h_1 site into h_{1a} and h_{1b} with one Os atom and without Os atoms in the projected triangle of the third layer atoms, as shown in Figure 4.

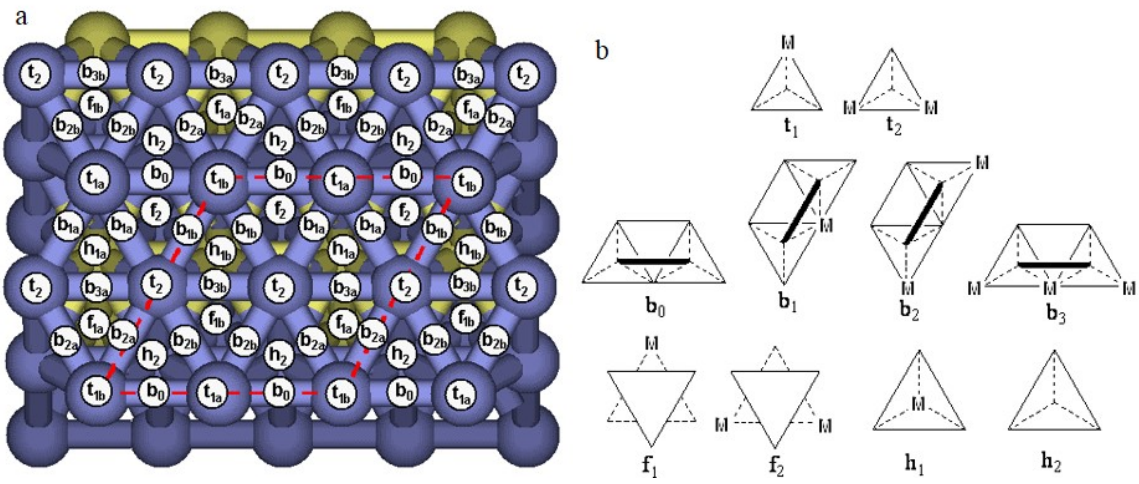

Figure 4. Binding sites on the $Pt_3Os(111)$ surface (a). For top sites t_1 and t_2, the triangle indicates the sublayer atoms (b). t_1 has one Os atom beneath it, while t_2 has two. For bridge sites, the bridge itself is shown as the thick black line, while the two terminals of the black line connect the two surface atoms, forming the bridge site. The trapezoid beneath is the sublayer atoms. b_0-b_3 have from

0 to 3 Os atoms in the sublayer. An fcc site is in the center of a surface triangle (shown as a solid triangle). f_1 and f_2 differ in the sublayer triangle beneath the surface triangle: f_1 has one Os atom beneath, while f_2 has two. An hcp site is also in the center of a surface triangle; it has one sublayer atom beneath: for h_1 it is Os, while for h_2 it is Pt.

3.2.2 *Binding Energies of ORR Intermediates*

First, we studied the preference of H_{ad}, O_{ad}, OH_{ad}, H_2O_{ad}, O_{2ad}, OOH_{ad}, and $HOOH_{ad}$ ORR intermediates on various binding sites shown in Figure 4. Tables 1 and 2 list binding energies of the above-mentioned intermediates on the $Pt_3Os(111)$ alloy surface in gas phase and solution, respectively. It should be noted that when considering energetics (binding energies and reaction barriers) related to ORR on the $Pt_3Os(111)$ surface and comparing them with ORR energetics on pure Pt, more attention should be paid to the solvation phase, because this phase better corresponds to the PEMFC operating conditions than the gas phase.

H binding. For the pure Pt surface, the binding energy of H_{ad} is 2.70−2.80 eV in gas phase and 2.81−2.87 eV in solvated phase. The strongest binding energy corresponds to the top site.

The preferred binding site for H_{ad} on the $Pt_3Os(111)$ surface is also the top site, t_{1b}, in gas phase, with a binding energy of 2.65 eV, followed by t_2 and t_{1a} with a binding energy of 2.57 and 2.55 eV, respectively. Under solvation, the preferred site becomes t_2 with a binding energy of 2.84 eV, followed by t_{1b}, b_{2b}, b_{3b}, t_{1a}, f_{1a}, b_{3a}, f_2, and b_0 with binding energies of 2.63−2.79 eV. Thus, for Pt_3Os, H_{ad} can migrate relatively easily in all directions to react with other ORR species.

O binding. On pure Pt, O_{ad} binds strongly to the fcc site with a net energy of 3.66 eV in the gas phase and 4.36 eV in the solvated phase. The huge solvation stabilization arises from electrostatics

due to the appearance of the strong dipole at surface O_{ad} atoms.

For Pt_3Os in gas phase, the strongest binding of O_{ad} is at the f_{1a} site, 3.55 eV, followed by the f_2 site with a binding energy of 3.48 eV. With solvent, the f_2 and f_{1b} sites become dominant with stronger binding energies of 5.18 and 4.97 eV, respectively. All other binding sites are significantly less stable than f_2. This means that O_{ad}, formed from O_{2ad} dissociation strongly prefers to occupy the f_2 site, and most probably no further migration occurs to other sites.

Table 1. Binding energies (eV) of various ORR species at different sites on Pt_3Os and Pt[59] in gas phase.

Pt_3Os							
Site	H	O	OH	O_2[a]	OOH[b]	H_2O[c]	H_2O_2[a]
t_{1a}	-2.55	-2.33	-1.86		-0.95 (-0.94)	-0.16	
t_{1b}	**-2.65**	-2.50	-1.95		**-1.06** (-0.94)	**-0.19**	
t_2	-2.57	-2.57	-2.03		-1.02 (-0.84)	-0.17	
b_0	-2.53	-3.05	-1.84	-0.49			-0.25
b_{1a}	-2.49	-3.03	-1.87	-0.36			-0.33
b_{1b}	-2.51	-3.02	-1.91	-0.39			-0.26
b_{3a}	-2.46	-3.02	-2.16	-0.53			-0.37
b_{3b}	-2.38	-2.87	-2.06	-0.47			**-0.38**
b_{2a}	-2.48	-3.11	**-2.20**	**-0.59**			-0.37
b_{2b}	-2.44	-3.02	-1.99	-0.44			-0.32
f_2	-2.52	-3.48	-1.86	-0.29			
f_{1a}	-2.49	**-3.55**	-2.17	-0.50			
f_{1b}	-2.42	-3.34	-2.04	-0.30			
h_{1a}	-2.45	-3.07	-2.12	-0.36			

h_{1b}	-2.40	-3.05	-2.02	-0.31			
h_2	-2.48	-3.21	-1.90	-0.34			
Best	**-2.65**	**-3.55**	**-2.20**	**-0.59**	**-1.06**	**-0.19**	**-0.38**
Pt							
T	**-2.80**	-2.50	-2.23		**-1.06**	**-0.22**	
b	-2.70	-3.10	-2.25	-0.40			**-0.27**
f	-2.72	**-3.66**	-2.22	**-0.46**			
h	-2.70	-3.28	**-2.28**	-0.35			
Best	**-2.80**	**-3.66**	**-2.28**	**-0.46**	**-1.06**	**-0.22**	**-0.27**

[a]The center of the O−O bond is used to denote the binding sites of O_2 and H_2O_2. Thus, b means that two O atoms are located approximately on the top of the surface atoms with the O−O bond center at the b site. The f and h binding sites are defined as one O atom located at the top site and the other at the b site with the O−O bond center at the f or h site, respectively.

[b]The position of the first O atom is used to denote the binding sites of OOH with the second O atom close to the b site. The numbers in parentheses correspond to the OOH binding at the t_{1a}, t_{1b}, and t_2 sites with the second O atom close to the f_{1b}, f_{1a}, and f_2 sites.

[c]The position of the O atom is used to denote the binding sites of H_2O with the O atom at the top site of Pt and two O−H bonds parallel to the surface.

Table 2. Binding energies (eV) of various ORR species at different sites on Pt_3Os and Pt[59] in solution.

Pt_3Os							
Site	H	O	OH	O_2[a]	OOH[b]	H_2O[c]	H_2O_2[a]

t_{1a}	-2.67	-3.08	-2.40		-1.46 **(-1.67)**	-0.45	
t_{1b}	-2.79	-3.18	-2.46		-1.61 (-1.44)	-0.49	
t_2	**-2.84**	-3.34	**-2.63**		-1.61 (-1.32)	**-0.52**	
b_0	-2.63	-3.75	-2.32	-0.77			-0.53
b_{1a}	-2.57	-4.36	-2.36	-0.68			-0.58
b_{1b}	-2.59	-4.78	-2.37	-0.84			-0.52
b_{3a}	-2.64	-3.87	-2.50	-0.85			-0.62
b_{3b}	-2.68	-4.24	-2.34	-0.74			-0.60
b_{2a}	-2.62	-3.86	-2.60	-0.94			**-0.62**
b_{2b}	-2.69	-4.46	-2.34	-0.77			-0.54
f_2	-2.63	**-5.18**	-2.41	-0.77			
f_{1a}	-2.66	-4.25	-2.56	**-1.06**			
f_{1b}	-2.54	-4.97	-2.59	-0.79			
h_{1a}	-2.58	-4.21	-2.56	-0.75			
h_{1b}	-2.42	-4.63	-2.39	-0.59			
h_2	-2.63	-3.88	-2.32	-0.74			
Best	**-2.84**	**-5.18**	**-2.63**	**-1.06**	**-1.67**	**-0.52**	**-0.62**
Pt							
t	**-2.87**	-3.09	**-2.77**		**-1.52**	**-0.58**	
b	-2.82	-3.73	-2.63	-0.73			**-0.61**
f	-2.85	**-4.36**	-2.57	**-0.87**			
h	-2.81	-3.92	-2.64	-0.70			
Best	**-2.87**	**-4.36**	**-2.77**	**-0.87**	**-1.52**	**-0.58**	**-0.61**

[a]The center of the O-O bond is used to denote the binding sites of O_2 and H_2O_2. Thus, b means that two O atoms are located approximately on the top of the surface atoms with the O−O bond

center at the b site. The f and h binding sites are defined as one O atom located at the top site and the other at the b site with the O−O bond center at the f or h site, respectively.

[b]The position of the first O atom is used to denote the binding sites of OOH with the second O atom close to the b site. The numbers in parentheses correspond to the OOH binding at the t_{1a}, t_{1b}, and t_2 sites with the second O atom close to the f_{1b}, f_{1a}, and f_2 sites.

[c]The position of the O atom is used to denote the binding sites of H_2O with the O atom at the top site of Pt and two O−H bonds parallel to the surface.

OH binding. On pure Pt, OH_{ad} has almost the same binding energy at all sites, with 2.22−2.28 eV in the gas phase and 2.57−2.77 eV in solution.

For Pt_3Os, the most preferred site in gas phase is b_{2a} followed by f_{1a}, b_{3a}, h_{1a}, and b_{3b}, with binding energies of 2.06−2.20 eV. In solution t_2 is the most preferred site, with a binding energy of 2.63 eV, followed by slightly weaker binding at the b_{2a} (2.60 eV), f_{1b} (2.59 eV), f_{1a} and h_{1a} (both 2.56 eV), and b_{3a} (2.50 eV). The binding energy of OH at all possible sites ranges within ~0.2 and 0.4 eV for Pt and Pt_3Os, respectively. This probably indicates the ability for easier OH_{ad} migration on pure Pt and harder OH_{ad} migration on the Pt_3Os surface.

In gas phase, both O and OH binding on Pt_3Os are weaker than on Pt, 3.55 vs. 3.66 eV and 2.20 vs. 2.28 eV, respectively. In solution, OH still binds more weakly on the Pt_3Os (111) surface (2.63 vs. 2.77 eV), whereas the O binding becomes stronger (5.18 vs. 4.36 eV). A possible reason for this change in solution might be a strong dependence of the solvent effect on a charge dipole. The dipole related to the O binding on Pt_3Os is obviously stronger than that related to the OH binding (Figure 5). Furthermore, the charge dipole between Os and Pt makes the solvent effect for Pt_3Os more significant than for an almost uniformly distributed slab of pure Pt.

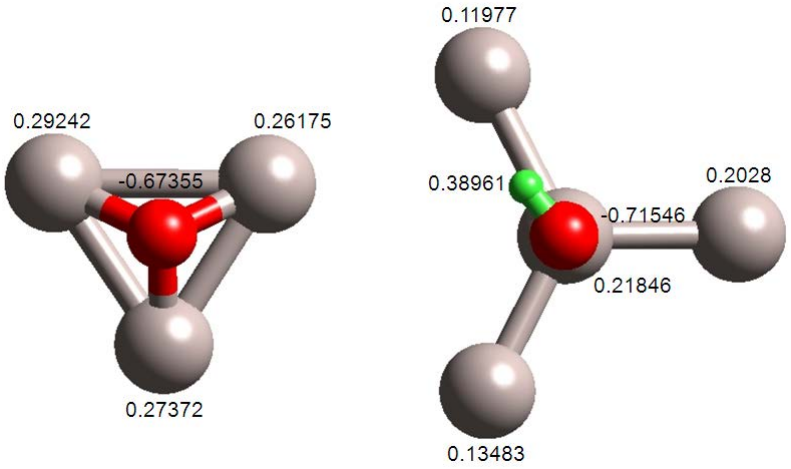

Figure 5. Charge dipoles related to the O and OH binding on $Pt_3Os(111)$ surface.

O_2 binding. For pure Pt, we find that the binding energy of O_{2ad} is 0.46 eV in gas phase and 0.87 eV in solution, with the difference for various sites ranging within 0.11 and 0.17 eV for gas phase and solution, respectively.

For Pt_3Os, O_{2ad} prefers to bind to the surface at the b_{2a} site with a binding energy of 0.59 eV in gas phase followed by b_{3a}, f_{1a}, b_0, and b_{3b} with similar binding energies of 0.53, 0.50, 0.49, and 0.47 eV, respectively. Overall, the corresponding binding energies vary from 0.29 to 0.59 eV. In the solvated Pt_3Os phase, the strongest binding energy, 1.06 eV, is for the f_{1a} site of O_2. The following energetically favored sites are b_{2a} (0.94 eV), b_{3a} and b_{1b} (0.85 and 0.84 eV, respectively), and f_{1b} (0.79 eV). Such a strong binding of O_{2ad} at the f_{1a} site should impede O_{2ad} migration to other sites.

OOH binding. For pure Pt, OOH_{ad} binds to the top sites with the terminal O bonded to the Pt and the OOH_{ad} plane parallel to the surface. OOH_{ad} prefers to have the O−O bond heading to an adjacent Pt atom. This leads to a binding energy of 1.06 eV in the gas phase and 1.52 eV in solution.

On the $Pt_3Os(111)$ surface, OOH_{ad} binds to the surface at the t_{1b} site with a similar strength, 1.06 eV, in gas phase, as in pure Pt. The corresponding binding energy of OOH_{ad} at other stable binding sites, t_{1a} and t_2, are 0.95 and 1.02 eV, respectively. In solution, OOH_{ad} binds to the $Pt_3Os(111)$ surface significantly stronger than in gas phase at all stable binding sites, by 0.5~0.6 eV. The preferred site is t_2 with a binding energy of 1.67 eV which is by ~0.15 eV stronger than the corresponding binding energy for pure Pt. It should also be noted that the OOH_{ad} binding at the t_2 site with the O-O bond toward f_2 is more stable than heading to another Pt atom, but the first O atom still binds to the t_2 top site. It is unstable for the first O atom to bind to other sites. Thus, once formed, OOH_{ad} will probably not migrate on the surface, but the O−O bond could be differently orientated.

H_2O binding. Similar to the case of pure Pt, H_2O_{ad} binds only to the top sites (t_{1a}, t_{1b}, and t_2) on the $Pt_3Os(111)$ surface with very similar binding energies, 0.16−0.19 eV in gas phase, and 0.45−0.52 eV in solution. These values are very close to the corresponding values for pure Pt, 0.22 eV in gas phase and 0.58 eV in solution. The difference between the binding energies in gas phase and solution is close to the value of the solvent stabilization of bulk H_2O_{ad}, 0.40 eV. Since the surface H_2O_{ad} does not bind to bridge, fcc, or hcp sites, migration of H_2O_{ad} from one top site to the others is through adsorption and dissociation. The migration barrier can be estimated to be 0.10~0.20 eV (the 0.50~0.60 eV binding energy minus the 0.40 eV solvation of H_2O_{ad}, H_2O is considered always solvated).

HOOH binding. Only the bridge sites are available for the $HOOH_{ad}$ binding on the Pt(111) and $Pt_3Os(111)$ surfaces. Two oxygen atoms bind to two neighboring top sites with the O−O bond parallel to the Pt-Pt bond. For Pt_3Os, the binding energies vary from 0.25 to 0.38 eV and 0.52 to 0.62 eV in gas phase and solution, respectively. Both are close to the $HOOH_{ad}$ binding energy of pure Pt, 0.27 eV in gas phase and 0.61 eV in solution.

Summarizing this section, we can say that the Pt_3Os binding energies show strong site dependence. However, we do not find any obvious trend for the binding energies of the O-containing species, in particular for the O and OH binding energy in solution. Thus, in the case of the $Pt_3Os(111)$ alloy surface, it is hard to decide whether Pt_3Os is a good ORR catalyst based only on the binding energies of the ORR intermediates. Reaction barrier calculations might help to make a more thorough conclusion.

3.3 Reaction Barriers and Possible ORR Mechanisms

Generally, eight fundamental steps (Figure 6) for the Langmuir–Hinshelwood mechanism of the ORR can be considered:

(1) H_2 dissociation: $H_{2ad} \rightarrow 2H_{ad}$

(2) O_2 dissociation: $O_{2ad} \rightarrow 2O_{ad}$

(3) OH formation: $O_{ad} + H_{ad} \rightarrow OH_{ad}$

(4) O hydration: $O_{ad} + H_2O_{ad} \rightarrow 2OH_{ad}$

(5) OOH formation: $O_{2ad} + H_{ad} \rightarrow OOH_{ad}$

(6) OOH dissociation: $OOH_{ad} \rightarrow OH_{ad} + O_{ad}$

(7) H - OOH dissociation: $OOH_{ad} + H_{ad} \rightarrow 2OH_{ad}$

(8) H_2O formation: $OH_{ad} + H_{ad} \rightarrow H_2O_{ad}$

By including these fundamental steps into an overall ORR mechanism, we distinguish three chemical processes:[107]

O−O bond activation, which can occur via two mechanisms: O_2 dissociation (2) and OOH formation (5) followed by OOH dissociation (6).

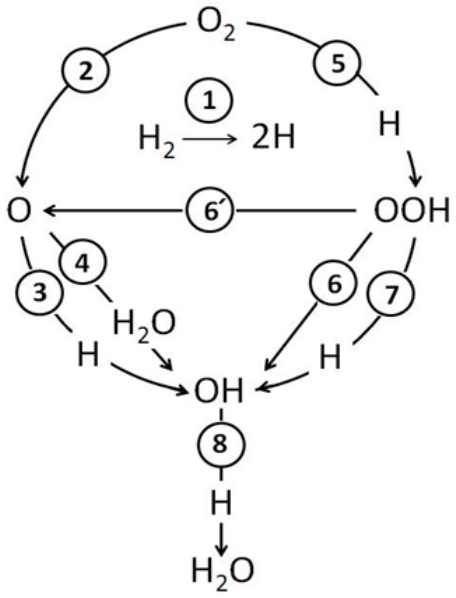

Figure 6. Eight ORR fundamental steps.

OH formation proceeds via three mechanisms: OH formation (3), O hydration (4), and H−OOH dissociation (7).

OH consumption: There is only one mechanism (H_2O formation (8)) for this process. A good catalyst must provide low barriers for all three of these processes and for pathways connecting them.

Starting from the preferred sites, we calculated the barriers for all eight steps on the $Pt_3Os(111)$ surface in gas phase and solution. These barriers and the corresponding barriers for pure Pt[59] are shown in Tables 3 and 4. The pathway with the lowest reaction barriers is used for the final determination of the ORR mechanism. The potential energy surface, including barriers and geometry insets for the OOH-form-hydr mechanism and O_2-diss-hydr mechanism[108] for Pt_3Os and Pt, is shown in Figure 7.

3.4 Reaction Barriers and ORR Mechanisms for Pt_3Os in Gas Phase

O-O bond activation. For pure Pt, OOH_{ad} formation with a barrier of 0.28 eV is followed by OOH_{ad} dissociation with a lower barrier of 0.14 eV, whereas the barrier for the direct dissociation is 0.58 eV.

In the Pt_3Os case, the OOH_{ad} formation barrier is 0.34 eV and the barrier for the OOH_{ad} dissociation is only 0.09 eV, whereas the barrier for the direct O_{2ad} dissociation is 1.36 eV, much higher than the barrier for the OOH_{ad} formation. Thus, it is preferable for the ORR pathway to proceed via the OOH formation step.

OH formation. The barrier for the direct OH_{ad} formation is 0.72 and 0.57 eV for Pt and Pt_3Os, respectively. This is significantly higher compared to the OH_{ad} formation via the O hydration step, 0.29 and 0.23 eV for Pt and Pt_3Os, respectively.

OH consumption. The H_2O_{ad} formation step proceeds with a small barrier of 0.11 eV for Pt and 0.09 eV for Pt_3Os.

Summarizing these three processes, we propose the following ORR mechanism for Pt and Pt_3Os in gas phase:

$O_2 + H \rightarrow OOH$ (E_a = 0.28 eV for Pt and 0.34 for Pt_3Os)

$OOH \rightarrow O + OH$ (E_a = 0.14 eV for Pt and 0.09 eV for Pt_3Os)

$O + H_2O \rightarrow 2OH$ (E_a = 0.29 eV for Pt and 0.23 eV for Pt_3Os)

$OH + H \rightarrow H_2O$ (E_a = 0.11 eV for Pt and 0.09 eV for Pt_3Os)

Table 3. Reaction barriers (eV) for Pt^{59} and Pt_3Os in gas phase.

Reaction Barriers	**Pt**	**Pt_3Os**
H_2 Dissociation	0.00	0.03
O_2 Dissociation	0.58	1.36
OH Formation	0.72	0.57
O Hydration	0.29	0.23
OOH Formation	0.28	0.34
OOH Dissociation	0.14	0.09
H-OOH Dissociation	0.18	0.24
H_2O Formation	0.11	0.09

Table 4. Reaction barriers (eV) for Pt^{59} and Pt_3Os in solvated phase.

Reaction Barriers	**Pt**	**Pt_3Os**
H_2 Dissociation	0.00	0.05
O_2 Dissociation	0.00	0.16
OH Formation	1.09	0.90
O Hydration	0.50	0.48
OOH Formation	0.19	0.00
OOH Dissociation	0.00	0.00
H-OOH Dissociation	0.04	0.41
H_2O Formation	0.17	0.35

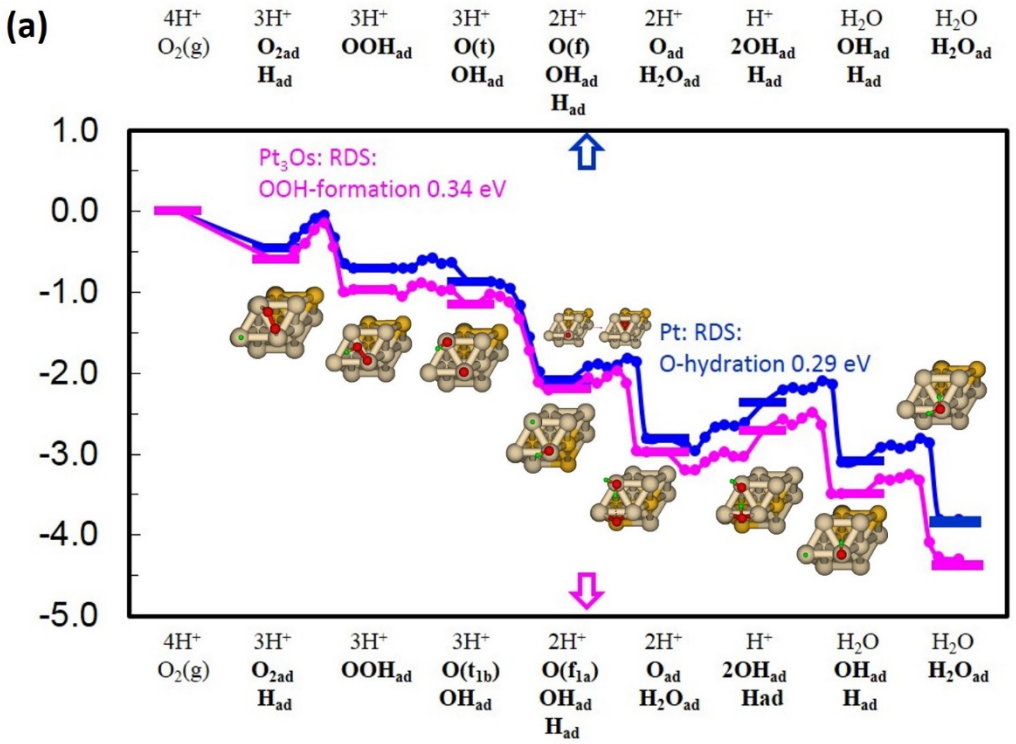
(a)
4H+ O2(g)
3H+ O2ad Had
3H+ OOHad
3H+ O(t) OHad
2H+ O(f) OHad Had
2H+ Oad H2Oad
H+ 2OHad Had
H2O OHad Had
H2O H2Oad
1.0
0.0
-1.0
-2.0
-3.0
-4.0
-5.0
Pt3Os: RDS:
OOH-formation 0.34 eV
Pt: RDS:
O-hydration 0.29 eV
4H+ O2(g)
3H+ O2ad Had
3H+ OOHad
3H+ O(t1b) OHad
2H+ O(f1a) OHad Had
2H+ Oad H2Oad
H+ 2OHad Had
H2O OHad Had
H2O H2Oad

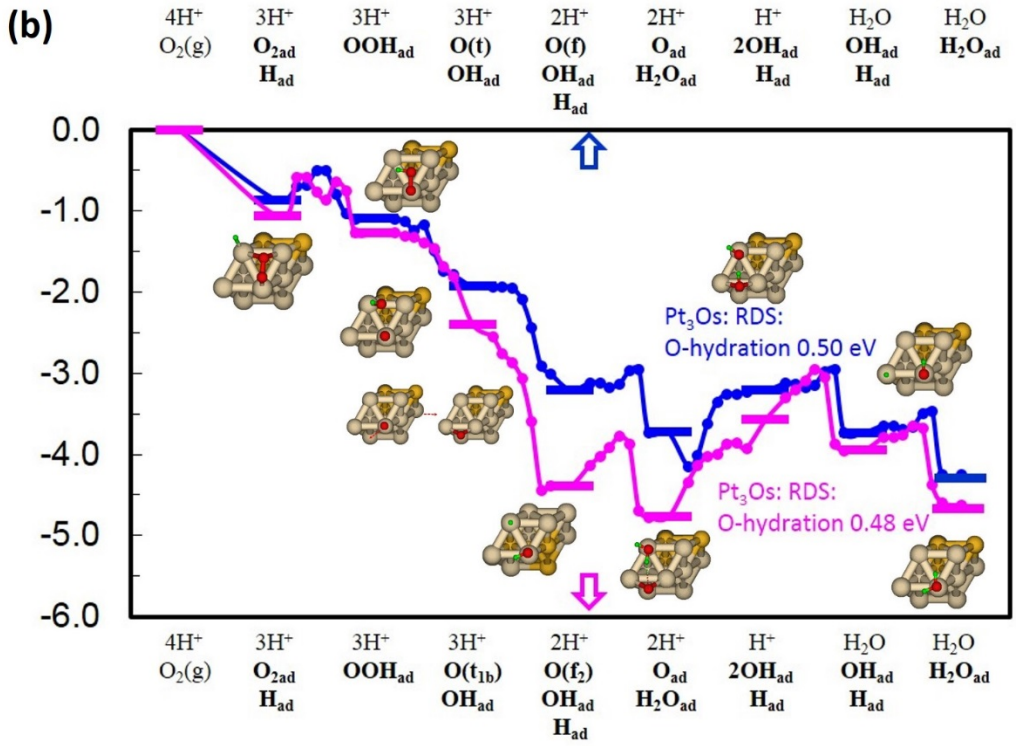
(b)
4H+ O2(g)
3H+ O2ad Had
3H+ OOHad
3H+ O(t) OHad
2H+ O(f) OHad Had
2H+ Oad H2Oad
H+ 2OHad Had
H2O OHad Had
H2O H2Oad
0.0
-1.0
-2.0
-3.0
-4.0
-5.0
-6.0
Pt3Os: RDS:
O-hydration 0.50 eV
Pt3Os: RDS:
O-hydration 0.48 eV
4H+ O2(g)
3H+ O2ad Had
3H+ OOHad
3H+ O(t1b) OHad
2H+ O(f2) OHad Had
2H+ Oad H2Oad
H+ 2OHad Had
H2O OHad Had
H2O H2Oad

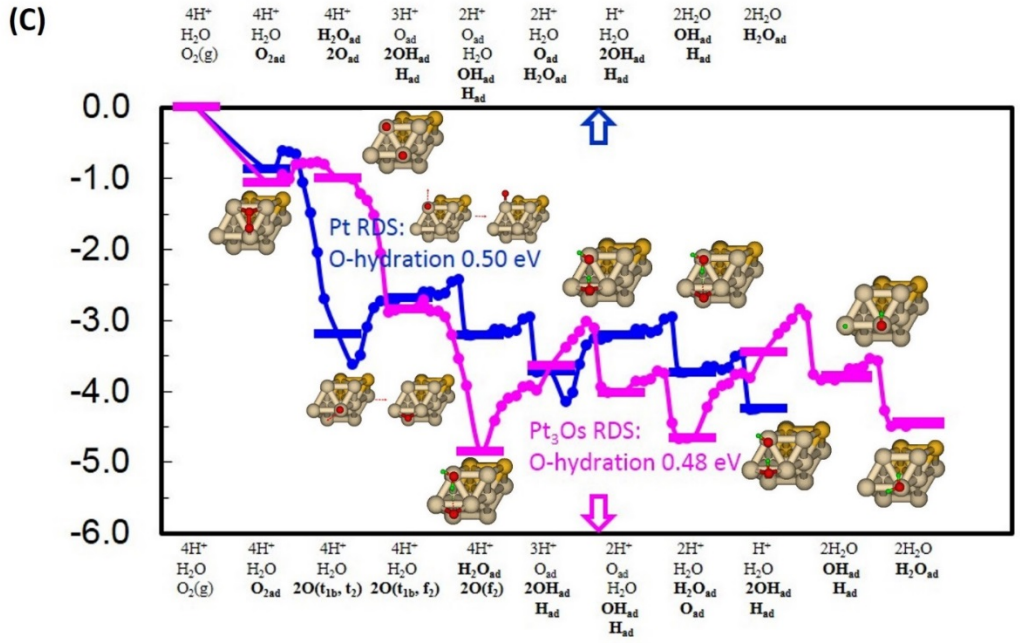

Figure 7. Potential energy surfaces, including reaction barriers for the OOH-form-hydr mechanism in gas phase (a), OOH-form-hydr mechanism in solution (b), and O_2-diss-hydr mechanism in solution (c) for Pt and Pt_3Os.

Figure 7a shows the potential energy surface of this mechanism for Pt and Pt_3Os. It starts from O_2 gas labeled as O_2(g), and represents the sequential steps of the ORR that follows the four-electron mechanism: $O_2 + 4H^+ + 4e^- \rightarrow 2H_2O$. For the purpose of conservation of atoms, we include $4H^+$ in the first step, although the proton successively comes to the cathode from the electrolyte. The reactants and products involved in each reaction step are marked by bold font. The rate-determining step (RDS) is O-hydration with a barrier of 0.29 eV for Pt and OOH formation with a barrier of 0.34 eV for Pt_3Os. Although the RDS barrier for Pt_3Os is higher than for Pt, the energy barrier for the O hydration reaction on the Pt_3Os(111) surface is lower (0.23 eV) than for Pt.

3.5 Reaction Barriers and ORR Mechanism for Pt_3Os in Solvated Phase

O-O bond activation. Since solvent strongly favors O_2 dissociation, this mechanism becomes preferable for the materials considered here. O_2 can easily dissociate to form O_{ad} at the fcc site with no barrier for Pt and with a barrier of 0.16 eV for Pt_3Os, where O_{ad} is at the top site (Figure 8). The solvent effect on the O_2 dissociation is stronger on Pt_3Os than on Pt (see Tables 3 and 4), which is related to the stronger solvent effect on the O_{ad} binding on Pt_3Os than on Pt. On Pt_3Os, O_2 first migrates from the f_{1a} site to the b_{2a} site, and then dissociates to two adsorbed oxygen at the t_{1b} and t_2 sites. The O atom adsorbed at the top site generates a stronger dipole than the O atom adsorbed at the fcc site, which results in the stronger solvent effect on Pt_3Os compared to pure Pt.

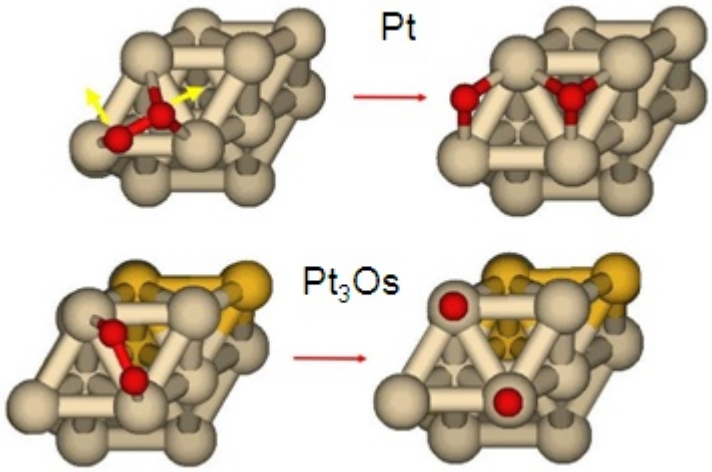

Figure 8. O_2 dissociation on Pt(111) and Pt_3Os(111) surfaces.

For comparison, OOH_{ad} formation and OOH_{ad} dissociation on the Pt_3Os surface is barrierless, which favors the ORR pathway to go via this step.

OH formation. Proceeding from the above conclusion, the second step should be O hydration, because the barrier for the direct OH_{ad} formation is 1.09 and 0.90 eV for Pt and Pt_3Os, respectively. The O hydration step with a barrier of 0.50 eV for Pt and 0.48 eV for Pt_3Os is significantly favorable.

OH consumption. The H_2O formation reaction on the Pt_3Os (111) surface occurs with a barrier of 0.35 eV, while pure Pt has a lower barrier of 0.17 eV.

Summarizing the above discussion, we come to the conclusion that the O_2-diss-hydr mechanism[108] is favorable for Pt, but for Pt_3Os, both the OOH-form-hydr mechanism and O_2-diss-hydr mechanism in solvated phase are feasible, although the OOH-form-hydr mechanism with the barrierless OOH_{ad} formation and OOH_{ad} dissociation steps looks more preferable than the O_2-diss-hydr mechanism:

O-O bond activation: $O_2 \rightarrow 2O$ (E_a = 0.00 eV for Pt, and 0.16 eV for Pt_3Os)

$O_2 + H \rightarrow OOH$ (E_a = 0.19 eV for Pt and 0.00 eV for Pt_3Os)

$OOH \rightarrow O + OH$ (E_a = 0.00 eV for Pt and 0.00 eV for Pt_3Os)

OH formation: $O + H_2O \rightarrow 2OH$ (E_a = 0.50 eV for P and 0.48 eV for Pt_3Os)

OH consumption: $OH + H \rightarrow H_2O$ (E_a = 0.17 eV for Pt and 0.35 eV for Pt_3Os)

Figures 7b and c show the potential energy surfaces of the OOH-form-hydr and O_2-diss-hydr mechanisms for Pt and Pt_3Os in solution. The RDS for both mechanisms is the O hydration step with a barrier of 0.50 and 0.48 eV for Pt and Pt_3Os, respectively. Spontaneous O_{ad} migration to the most stable fcc site after the OOH dissociation step or the O_2 dissociation step is included in the figure as well.

Based on this result, the ORR catalytic activity of the Pt_3Os alloy can be estimated and compared to that of pure Pt. We find that Pt_3Os should show about 2 times better catalytic activity than pure Pt ($e^{-0.48ev/kT}/e^{-0.50ev/kT} = 2.18$) at 80°C. Nilekar et al.[50] calculated the OH−OH repulsive energy and correlated it with the measured kinetic current density for $Pt_{0.8}M_{0.2}$/Pd(111), where M = Au, Pd, Rh, Re, and Os. Under 0.8 V, the current density for $Pt_{0.8}Os_{0.2}$/Pd (111) is about 3 times better than for Pt/Pd(111) (47 vs. 17 mA/cm^2). Pt alloys with Os and Re were found to be more reactive than the others due to their high OH−OH and OH−O repulsive energy. Another possible way to explain the better performance of Pt_3Os is either by the smaller size of the Os atom, which results in a compressed strain (strain effect) for the surface Pt atoms, or the electronic interaction (ligand effect) of the subsurface Os atoms with the surface Pt atoms. In general, the strain and ligand effects occur simultaneously and it is hard to separate them. Both effects are manifested in the interatomic matrix element describing bonding interaction between an atom and its nearest neighbors.[109] For the Pt_3Os catalyst, the electronic structure of the surface Pt is modified by the underlying Os atoms, and the Pt–Pt bond distance is compressed to 2.76 Å compared to 2.81 Å for the Pt bulk structure. Nørskov et al. developed the d-band model,[9,109,110] which was applied to connect the surface chemical properties of bimetallic alloy catalysts with their electronic structures. For compressive strain, the interatomic distances become smaller and the overlapping of metal d-states increases. The increased *d*-state overlapping results in the increased d-band width, which is highly correlated with the position of the *d*-band center due to the fact that the *d*-band filling changes negligibly upon the formation of the bimetallic surfaces. To maintain the filling, the broader d-band downshifts the d-band center, which results in weaker adsorbate bonding. On the Pt_3Os(111) surface, the downshift of the surface *d*-band center relative to pure Pt(111) is ~0.35 eV (Figure 9), whereas according to Stamenkovic et al.,[23] this downshift should be ~0.2 eV and the O/OH bindings should be by 0.1−0.2 eV weaker[23,26,28] to reach the maximum oxygen reduction

activity. Both above-mentioned effects reduce the O and OH binding energies (the O binding energy on the $Pt_3Os(111)$ surface is by 0.11 eV weaker than for Pt(111), 3.55 vs. 3.66 eV, and the OH binding energy for $Pt_3Os(111)$ is by 0.08 eV weaker than for Pt(111), 2.20 vs. 2.28 eV; see Table 1) in gas phase. However, in solution, which is more relevant to the PEMFC operating conditions, O binds stronger on Pt_3Os than on pure Pt (see Table 2), but the computed RDS barrier is lower for Pt_3Os, 0.48 vs. 0.50 eV for Pt. Therefore, knowing the binding energies of the intermediates is not always sufficient to reliably predict the ORR activity. Reaction barriers have to be considered as well to better understand the ORR kinetics. The result obtained in our study indicates that Pt-Os materials might be considered as potential ORR catalysts.

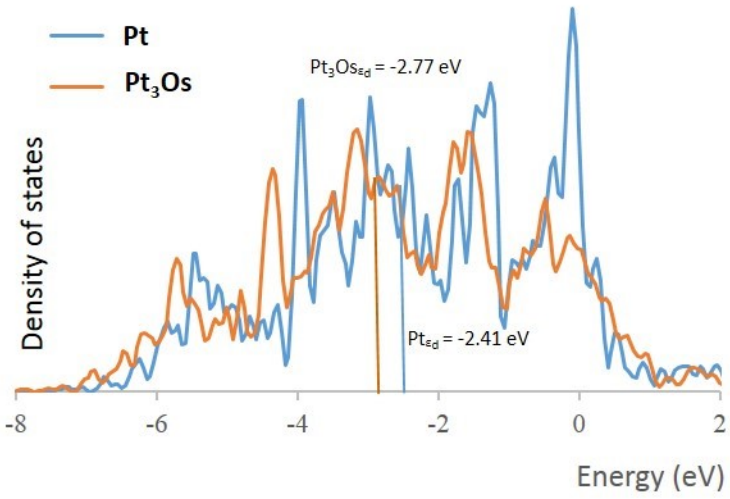

Figure 9. Densities of states and *d*-band centers for Pt(111) and $Pt_3Os(111)$ surface layers.

3.6 Experimental Verification

To verify our simulation results, we performed the dealloying method to synthesize Pt_3Os nanoparticles. Table 5 lists the structural data and composition for our synthesized Pt_2Os, DA-Pt_2Os, and commercial Pt nanoparticles. Based on SEM-EDS analysis, the atomic ratio for our DA-Pt_2Os electrocatalyst is ~ Pt : Os = 4 :1, slightly deviating but not far from our target Pt : Os =3 :1.

Table 5. Structural parameters and composition of Pt/C, Pt_2Os/C, and DA-Pt_2Os/C electrocatalysts.

Sample	Peak angle (2θ)	Lattice constant (Å)	Particle size[a] (nm)	Particle size[b] (nm)	Atomic ratio[c] Pt/Os	Atomic ratio[d] Pt/Os
Pt/C	39.62	3.94	2.09	2.3±0.4	-	-
Pt_2Os/C	41.01	3.81	3.65	3.1±0.7	68/32	67/33
DA-Pt_2Os/C	40.43	3.85	3.7	3.1±1	93/7	81/19

a. Mean particle size calculated from Debye-Scherrer equation on Pt (111) and Pt_2Os (220) planes.
b. Mean particle size observed from TEM images.
c. Atomic ratio determined by TXRF.
d. Atomic ratio determined by SEM-EDS.

The elemental profiles of Pt and Os in the Pt_2Os and DA-Pt_2Os nanoparticles were obtained by the STEM-EDS measurements with a probe size of about 1.5 Å. Figure 10 (a) exhibits a STEM image and the corresponding line-scan profile across a Pt_2Os nanoparticle in 4.5 nm size. The result suggested an alloy state for the as-synthesized Pt_2Os nanoparticles. Figure 10 (b) shows a STEM image and the line-scan profile of a DA-Pt_2Os nanoparticle of 7 nm in diameter. Apparently, the Os atoms residing on the surface regime were mostly removed and the DA-Pt_2Os (Pt_4Os) revealed a quasi-core-shell structure in which the core retained some Os atoms, whereas the shell was occupied by the Pt atoms exclusively.

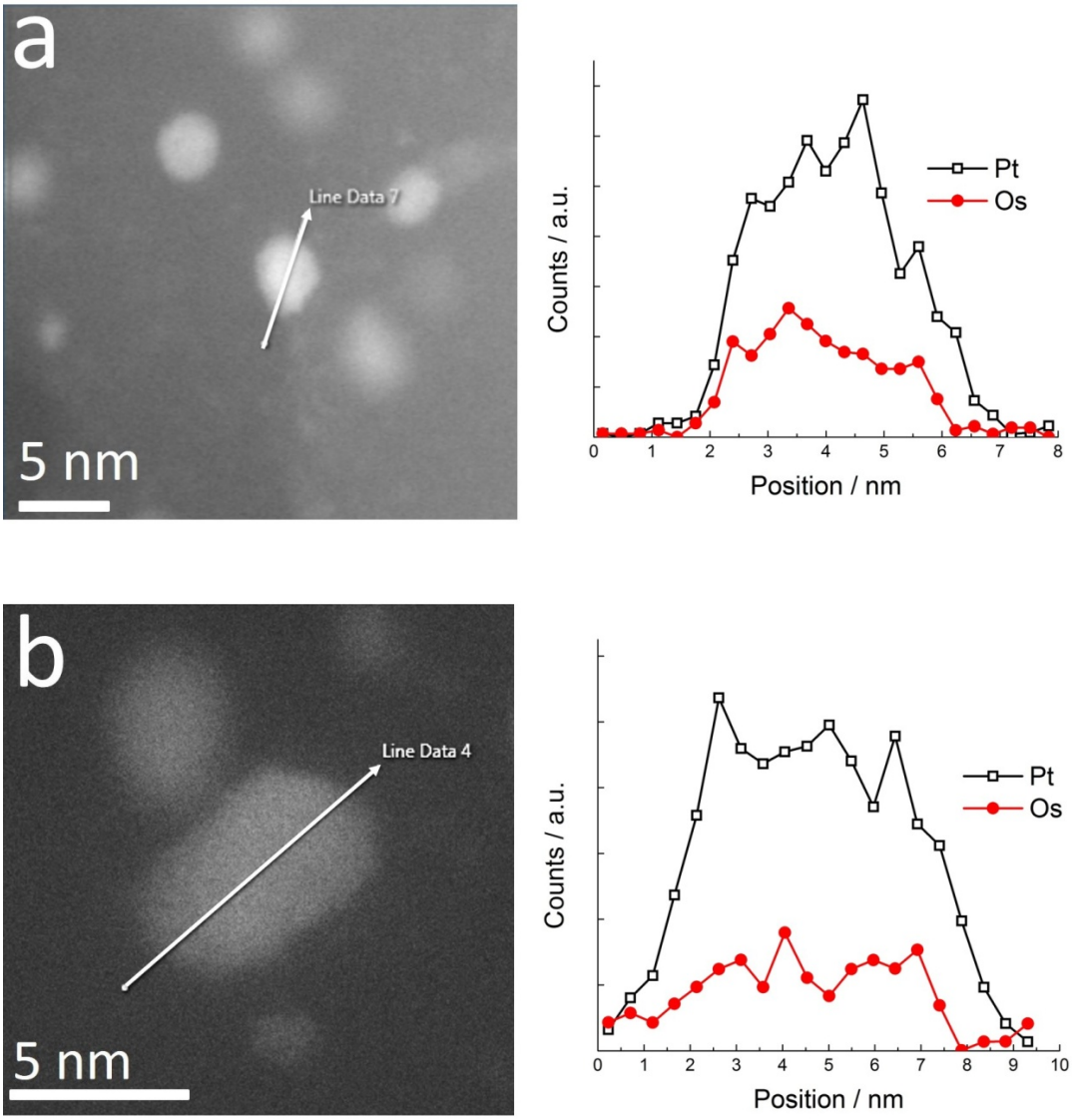

Figure 10. The STEM images and EDS line-scan of (a) Pt_2Os (b) DA-Pt_2Os nanoparticles.

Figure 11 demonstrates the ORR CV curves for Pt_2Os/C, DA-Pt_2Os/C, and Pt/C. In the literature, at potential below 0.6 V, the ORR response is under mass transport control limited by the diffusion of the dissovled oxygen in the electrolyte, whereas at potential between 0.8 and 1 V the ORR response is dominated by kinetics (the electrocatalytic activity of the electrocatalyst involved in the ORR process).[111] Hence, a simple method to quickly evaluate the ORR behavior of a potential

electrocatalyst is the reading of half-wave potential, which is defined as the potential at which the magnitude of the current is half of the limiting current. In general, the larger the half-wave potential, the greater the ORR activity. As shown, the half-wave potentials for the Pt/C, Pt_2Os/C, and DA-Pt_2Os/C were 891, 837, and 908 mV, respectively. Moreover, the DA-Pt_2Os/C exhibited the highest on-set potential of 1 V, and this provided more evidence of better electrocatalytic ability among these samples.

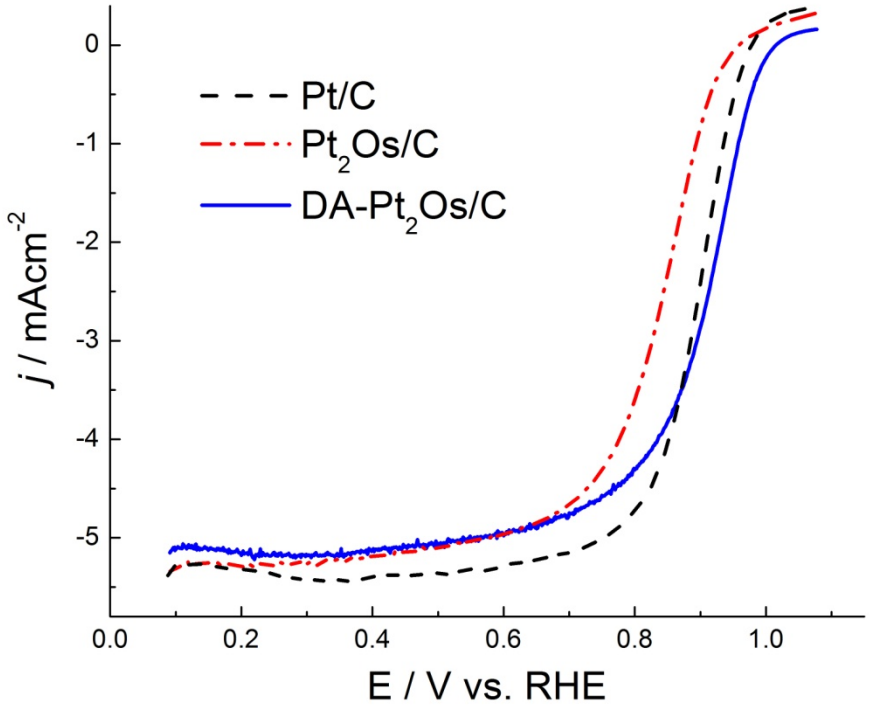

Figure 11. The ORR curves of Pt/C, Pt_2Os/C, and DA-Pt_2Os/C in apparent current density.

Figure 12 (a) demonstrates the ORR curves from the DA-Pt_2Os/C at various rotation speeds of RDE. Among these curves, the ORR responses at voltage below 0.6 V were stabilzed at the limiting

currents, whose values were proportional to the rotation speed as expected. To extract the kinetic information, we employed the Koutecky-Levich equation listed below,[112]

$$1/i = 1/i_{kinetic} + 1/i_{diffusion\ limit} = 1/i_{kinetic} + 1/0.62nFAD_{O2}^{2/3}\omega^{1/2}v^{-1/6}C_{O2} \qquad (1)$$

where i is the experimentally-measured current, $i_{diffusion\ limit}$ is the diffusion limiting current due to the limitation of mass transport of dissolved oxygen in the 0.1 M aqueous $HClO_4$ solution, $i_{kinetic}$ is the kinetic current associated with the ORR activity of DA-Pt_2Os/C, n is the number of electron transferred in the ORR process, F is the Faraday constant, A is the reaction area of the RDE (0.196 cm^2), D_{O2} is the diffusivity of dissolved oxygen in the 0.1 M aqueous $HClO_4$ solution (1.93×10^{-5} cm^2 s^{-1}),[113] ω is the rotation speed of the RDE, v is the kinematic viscosity of the 0.1 M aqueous $HClO_4$ solution (1.009×10^{-2} cm^2 s^{-1}),[112] and C_{O2} is the concentration of dissolved oxygen in the 0.1 M aqueous $HClO_4$ solution (1.26×10^{-3} mol L^{-1}).[113] Figure 12 (b) provides the Koutecky-Levich plots at different potentials. Obviously, these curves showed a consistent pattern and the average slope was 11.11 mA^{-1} $s^{-1/2}$. Thus, the resulting n value became 3.94. Therefore, we concluded that the DA-Pt_2Os/C nanoparticles adopted a four-electron route to catalyze the ORR process, similar to that of Pt.

The values of $i_{kinetic}$ obtained from the Koutecky-Levich equation were used to calculate the mass activity and specific activity shown in Figure 13. These Tafel plots were obtained using $i_{kinetic}$ values from 0.95 to 0.8 V divided by the effective mass of the Pt in the RDE (from ICP-MS) and

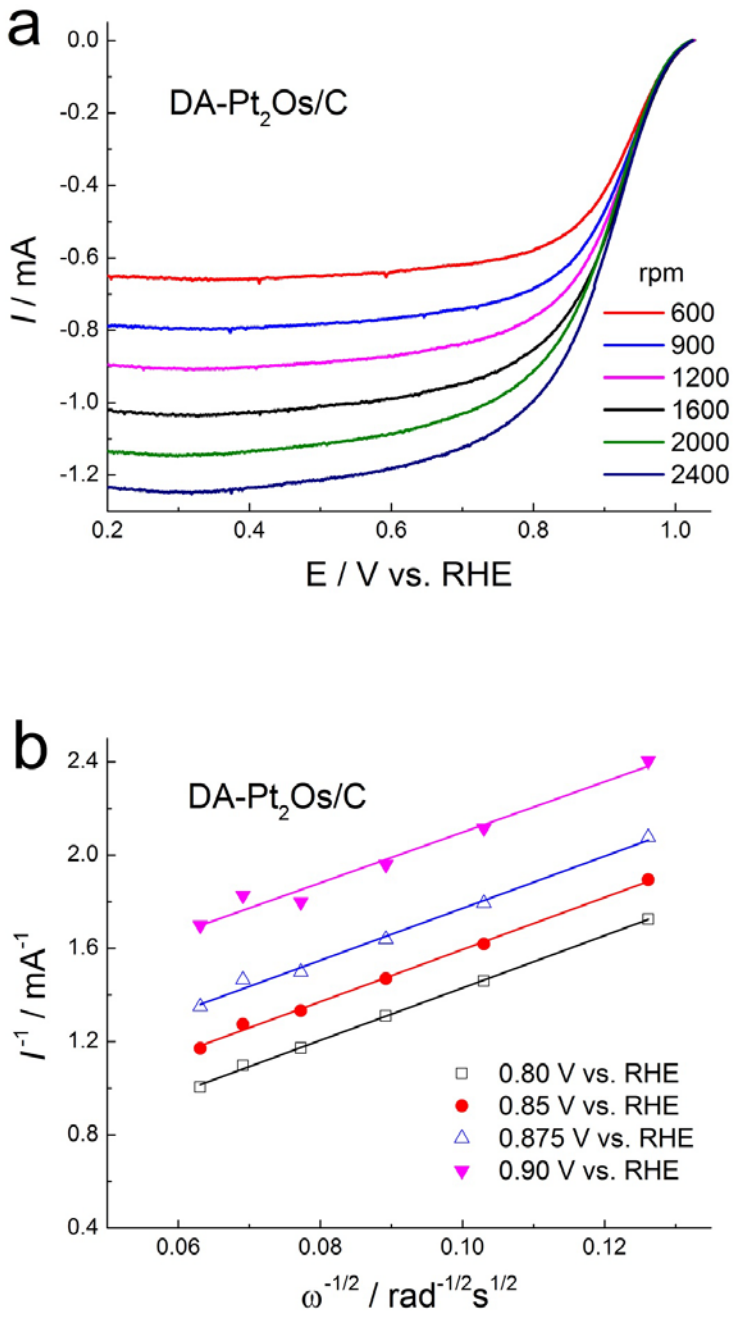

Figure 12. (a) The ORR curves of DA-Pt_2Os/C at various rotation speeds. The electrolyte was oxygen-saturated 0.1 M aqueous $HClO_4$ solution and the scan rate was 10 mV s^{-1}. (b) The Koutecky-Levich plot of DA－Pt_2Os/C at different voltages.

ECSA (cm_{Pt}^2) values. For the Pt/C, its mass activity and specific activity at 0.9 V were 0.14 mA μg_{Pt}^{-1} and 0.28 mA cm_{Pt}^{-2}, respectively. However, the Pt_2Os/C exhibited a lower mass activity (0.05 mA μg_{Pt}^{-1}) and a greater specific activity (0.52 mA cm_{Pt}^{-2}), as compared to those of Pt/C. The reduced mass activity is attributed to its relatively larger size as compared to that of Pt/C because the predominant share of the Pt atoms was residing at the core. However, the 250% increment in the specific activity suggested the complementary role of Os atoms to the Pt atoms for ORR activity. This is because the surface of the Pt_2Os nanoparticle was partially occupied by the Os atoms, and those Os atoms were oxyphilic and thus promote the ORR process via bifunctional model and electronic mechanism. In the bifunctional model, the Os atoms exhibit a strong affinity toward the adsorption of OH and as a result lead to a considerable reduction in the Pt-OH coverage.[72] In general, a larger percentage of OH coverage on the Pt sites is considered disadvantageous for the ORR action. According to Zhang et al., two OH species can adsorb onto a single Os atom and subsequently initiate a spontaneous breakup of the O-H bonding forming an oxygen atom and water.[72]

Once the dealloying process was completed, the DA-Pt_2Os demonstrated a significantly-enhanced mass activity (0.29 mA μg_{Pt}^{-1}) and specific activity (1.03 mA cm_{Pt}^{-2}). We realized that the removal of Os atoms engendered a Pt-enriched surface with a substantially-enlarged ECSA. At this stage, the contributory role played by the Os atoms can be explained mostly by the electronic effect because the electronic structure of the surface Pt atoms was expected to be altered by the Os atoms underneath, as our previous discussion in section 3.5 describes.

For durability tests, the DA-Pt_2Os and Pt/C samples were subjected to multiple CV scans in a potential window of 0.65 and 1.05 V at 50 mV s^{-1} in a 0.1 M aqueous $HClO_4$ solution following procedures used by Wang et al.[115] Figure 14 shows the ORR responses before and after the durability test for DA-Pt_2Os/C and Pt/C, (a) and (b), respectively. Apparenttly, for both samples

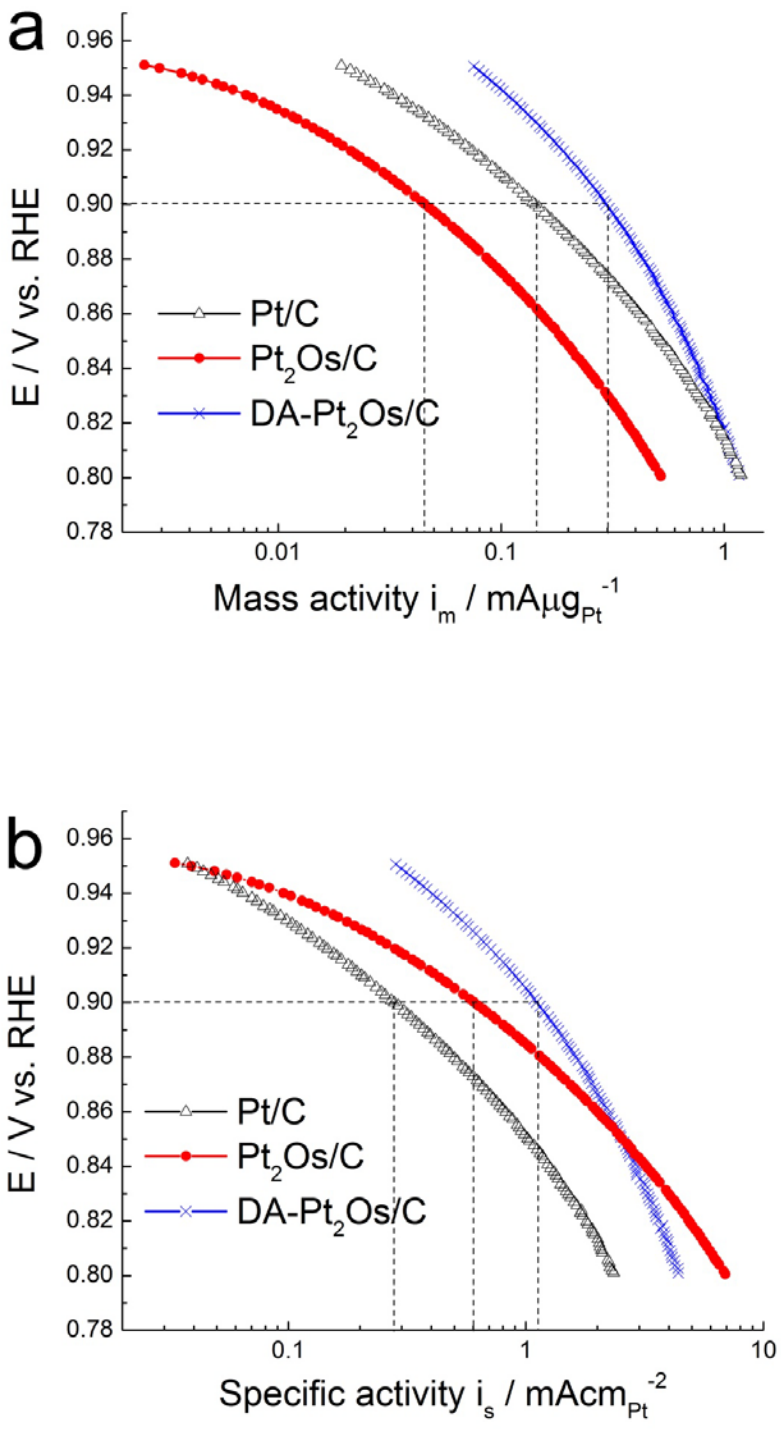

Figure 13. The Tafel plots of the ORR curves (Figure 11) in (a) mass activity and (b) specific activity.

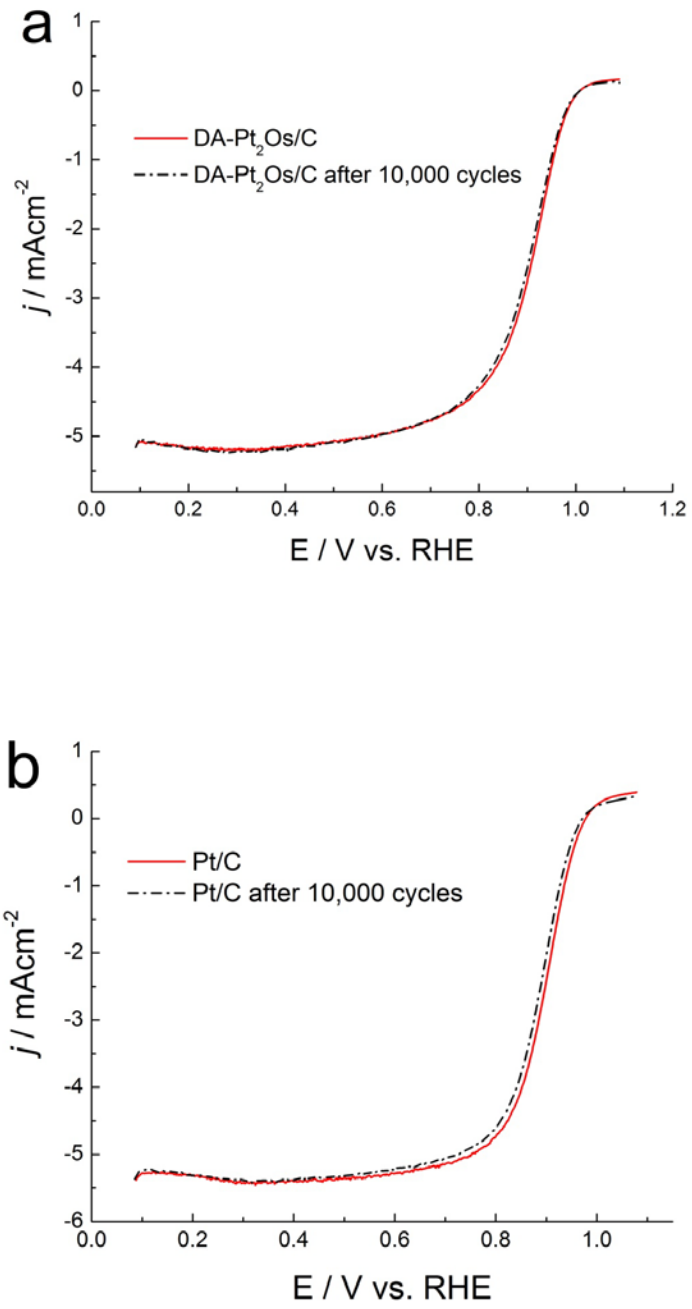

Figure 14. The ORR curves before and after the durability test for (a) DA-Pt_2Os/C and (b) Pt/C. The electrolyte was oxygen-saturated 0.1 M aqueous $HClO_4$ solution and the scan rate was 10 mV s^{-1}.

there appeared a very subdued degradation during the durability tests, and both the onset potentials and diffusion-limiting currents remained almost unchanged. The minor degradation is manifested in the slight negative shift of the half-wave potential at 5 and 9 mV for DA-Pt_2Os/C and Pt/C, respectively. These CV curves suggested that the stability of DA-Pt_2Os/C was comparable or even better than that of commercially available Pt nanoparticles. Since the Os atoms are easily oxidized in the electrolyte, a stable Pt-shell structure formed for DA-Pt_2Os/C catalyst.

The DFT study of the Pt segregation on the Pt_4Os slab is performed to support the experimental observation and the results were summarized in Figure 15. The five layer 2×2 cell slab contains 16 Pt atoms and 4 Os atoms, providing the 4:1 ratio. 4 Os atoms cannot be equally distributed in five layers, so one of the layers should be pure Pt. The *a* slab shows a uniform Os distribution in four lower layers with the pure Pt top layer. This structure was chosen because from our previous calculations[29] we know that the Pt_3Os alloy demonstrates strong surface segregation and the most stable Pt_3Os slab structure has 100% Pt at the top surface layer, 50% Pt in the second layer, and 75% Pt in the following layer.

The *b* structure has pure Pt at the top and in the second layer, but with 50% Os in the third layer, and 25% Os in the following layers.

The *c* structure also has two top layers of Pt but is Os enriched in the bottom layer rather than in the third layer.

Our calculation shows that the most stable structure is *b*, followed by *a* and *c* (see Figure 15). This is consistent with our previous segregation study of Pt-based binary alloys,[29] which found that the most stable structure of the segregated alloys has Pt-skin on the surface. The 6 layer 2×2 and 4 layer 3×3 cell models provide a similar result. Therefore, both experiment (STEM-EDS analysis) and

theory (computational modeling) demonstrate that the DA-Pt_2Os (Pt_4Os) prefers the Pt-skin surface structure. The Pt segregation is expected to influence the electronic structure of the alloy and affects its electrochemical activity as we mentioned before.

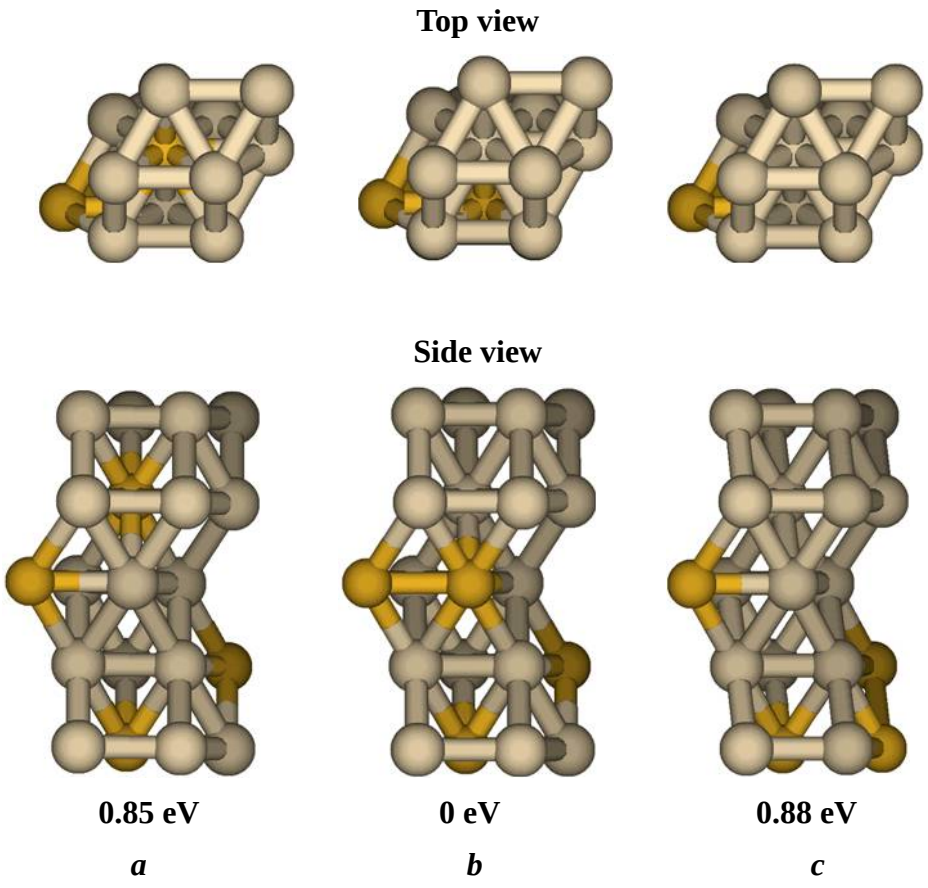

Figure 15. The surface segregation models for 5 layers of DA-Pt_2Os electrocatalysts. (a) the uniformly distributed structure, (b) the segregated structure with Os enriched in the third layer, and (c) the segregated structure with Os enriched in the bottom layer. The energies are relative to the energy of the most stable structure b, at -48849.55 eV.

3.7 Summary for Pt_3Os Catalyst

Surface segregation of a number of Pt_3M alloys was investigated. Only a few Pt binary alloys demonstrate favorable surface segregation energy in the presence of adsorbed O or OH. Out of them, only Pt_3Os and Pt_3Ir show surface segregation in the presence of both adsorbed species. This assumes that unlike other Pt-based binary alloys, Pt_3Os and Pt_3Ir might be stable under fuel cell operating conditions. We systematically studied the binding site preference of all reaction intermediates involved in ORR on Pt_3Os in gas phase and solution. The binding energies of adsorbates on the alloy surface show the strong sublayer dependence. Reaction barriers for the eight ORR fundamental steps were also calculated for Pt_3Os both in gas phase and solution, and compared to those for pure Pt. According to our result, Pt_3Os has a slightly lower energy barrier for the ORR RDS than pure Pt, which should result in better catalytic activity compared to pure Pt. This conclusion is in agreement with our earlier performed experimental study of Pt-Os catalysts, in which we found that the ORR mass and specific activities of dealloyed Pt_2Os materials are 2 and 3.5 times better than the corresponding activities of pure Pt. In addition, these materials show good electrochemical stability. Thus, Pt-Os alloys might be considered as promising ORR catalysts.

Chapter 4

Results and Discussion for Os/Pt Core-Shell Catalysts

4.1 Stability of the Os/Pt Core-Shell Structure

The crystal structure of Os is hcp, while that of Pt is fcc. The stacking sequences for the closest packed planes of hcp (0001) and fcc (111) are ABABAB and ABCABC, respectively. To determine structures with different numbers of Pt layers deposited on the Os core, we calculated all the stacking sequences and compared their energies (see Table 6). Each letter in the "Pt/Os surface structure" row represents a specific layer in the structure. The capital letters represent Os layers, while the lower cases denote Pt layers. For example, the label b/ABA means that the structure has a Pt monolayer with the b stacking on the three Os layer substrate with the ABA stacking sequence. The lowest energy stacking sequence result conforms to the similar DFT result for the Ru(hcp)/Pt(fcc) core-shell catalyst.[61,116] In addition, our recent study using HAADF STEM technique proves the energetically favorable cb/ABAB stacking sequence for Pt_{2ML}/Ru obtained from the DFT calculation.[116] We used the lowest energy stacking sequences as the stable structures for calculations of binding energies and reaction energy barriers on Pt/Os slabs.

Table 6. Relative energies (eV) for Pt/Os surface structures with different stacking sequences.

Pt/Os surface structure	Relative Energy
Pt_{1ML}/Os	
b/ABA	0.07
c/ABA	**0.00***
Pt_{2ML}/Os	
ab/ABA	0.53
cb/ABA	**0.00***
bc/ABA	0.40
ac/ABA	0.81
Pt_{3ML}/Os	
bab/ABA	0.82
cab/ABA	0.32
acb/ABA	**0.00***
bcb/ABA	0.52
abc/ABA	0.29
cbc/ABA	0.66
bac/ABA	0.64
cac/ABA	1.03

*Reference energy: c/ABA: -76283.72 eV; cb/ABA: -99327.96 eV; acb/ABA: -122371.54 eV. All energies are relative to the lowest one (bold numbers).

4.2 Binding Sites and Binding Energies

4.2.1 *Binding Site Notations*

Figure 16 shows the binging sites on Os and Pt/Os surfaces. There are four types of sites on the closed-packing plane:

- On top, bonded to one Os or Pt atom (μ1), denoted as t
- Bridging between two Os or Pt atom (μ2), denoted as b
- An fcc position between three Os or Pt atom (μ3), denoted as f
- An hcp position between three Os or Pt atom (μ3), denoted as h

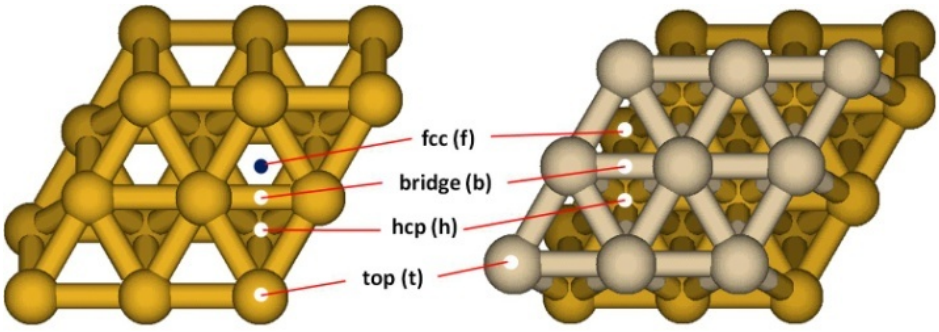

Figure 16. Binding sites on Os (left) and Pt/Os (right) slab surfaces.

In our notations, capital letters represent the binding species, such as H, O, O_2, etc. The lower case letters denote the binding sites. For OH and OOH, two and three lower case labels are applied to distinguish the different orientations of the species. Figure 17 illustrates some examples for the labels of OH and OOH species on the Pt/Os catalyst surface. OH/b-f means OH with O adsorbed

at the b bridge site and H at the f site. OOH/t-b-f denotes OOH with the first O at the top site, the second O at the b bridge site, and the H atom at the f site. OOH/t-f labels only the O positions: the first O at the top site and the second O at the f site. Similar notation rules are applied to other ORR intermediates. Figure 18 shows binding energies of the ORR intermediates at the most stable sites on the Os, Pt, and Pt/Os surfaces in vacuum and solvent. All binding energies for the ORR species at various surface sites are summarized in Tables 7 and 8. It should be noted that after geometry optimization, the OH/f and OH/h spontaneously move to the sites which can be considered as OH/b-f and OH/b-h with similar corresponding energy values.

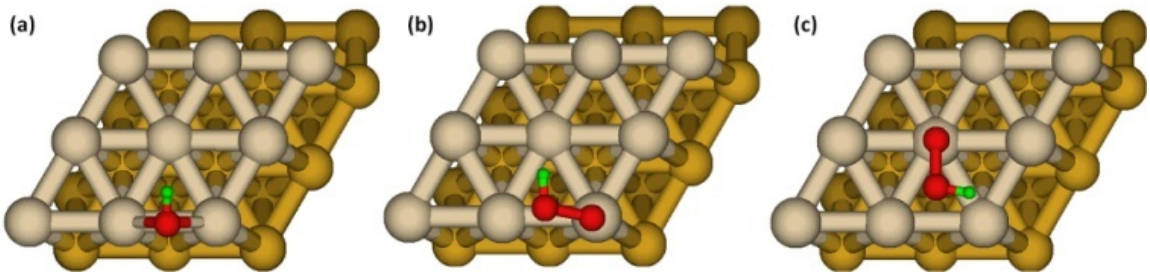

Figure 17. OH and OOH species on the Pt/Os catalyst surface: (a) OH/b-f (b) OOH/t-b-f and (c) OOH/t-f.

H binding. On the pure Os surface, both in gas phase and solvent, H prefers the f site, but the binding energy difference between various sites is not significant.

For Pt and Pt/Os surfaces, the t site is most preferable for the H binding. The binding energy values lie between -2.45 and -2.81 eV in gas phase and -2.61 and -2.90 eV in solvation phase. It is worthy to notice that the binding energy rises with an increasing number of deposited Pt layers and approaches the binding energy for the pure Pt surface. A similar trend is observed for most of the ORR species.

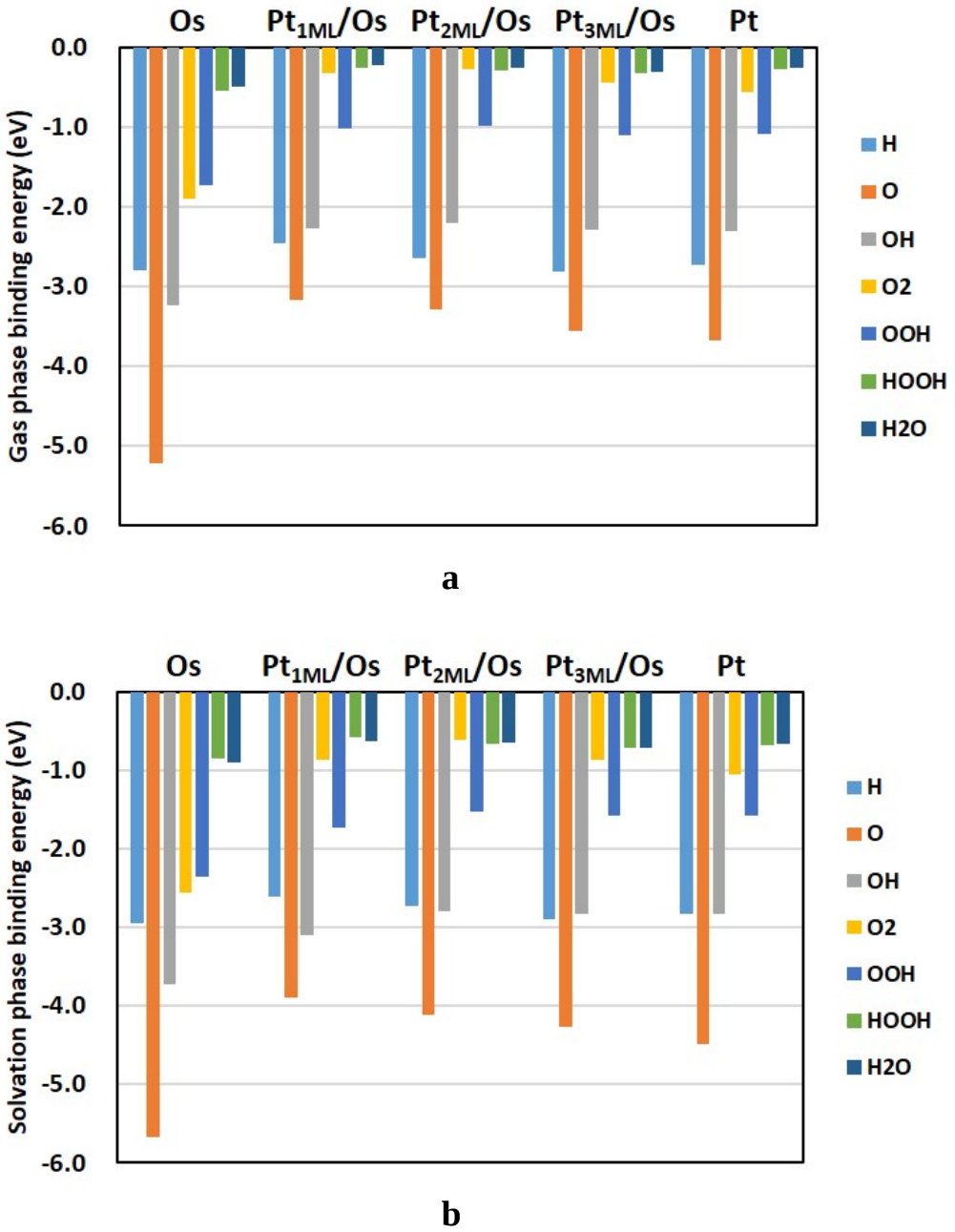

Figure 18. Binding energies of the ORR intermediates at the most stable sites on Os, Pt, and Pt/Os surfaces in gas phase (a) and solution (b).

Table 7. Binding energies[a] (eV) of ORR species at various binding sites on Os, Pt, and Pt/Os surfaces in gas phase.

Species	pure Os	pure Pt	Pt_{1ML}/Os	Pt_{2ML}/Os	Pt_{3ML}/Os
H/b	-2.72	-2.65	-2.34	-2.53	-2.69
H/f	**-2.80**	-2.66	-2.35	-2.53	-2.68
H/h	-2.71	-2.62	-2.34	-2.53	-2.66
H/t	-2.69	**-2.73**	**-2.45**	**-2.64**	**-2.81**
O/b	-4.57	-3.20	-2.90	-2.98	-3.16
O/f	-4.87	**-3.68**	**-3.16**	**-3.29**	**-3.55**
O/h	**-5.21**	-3.33	-2.97	-3.08	-3.27
O/t	-4.26	-2.62	-2.36	-2.29	-2.33
OH/b-f	**-3.24**	**-2.31**	-2.26	-2.17	-2.28
OH/b-h	-3.20	-2.30	-2.26	-2.17	-2.27
OH/f	Unstable[b]				
OH/h	Unstable[b]				
OH/t	-3.09	-2.28	**-2.27**	**-2.21**	**-2.29**
O_2/b	-1.80	**-0.56**	**-0.33**	**-0.28**	**-0.45**
O_2/f	-1.78	-0.49	-0.28	-0.19	-0.43
O_2/h	**-1.89**	-0.43	-0.30	-0.24	-0.44
OOH/t-b-f	unstable	-1.09	-1.02	-0.99	-1.11
OOH/t-b-h	unstable	**-1.09**	**-1.02**	**-0.99**	**-1.11**
OOH/t-f	**-1.73**	-1.01	-0.92	-0.91	-1.05
OOH/t-h	-1.68	-1.03	-0.91	-0.91	-1.05
HOOH/b	**-0.55**	**-0.27**	**-0.26**	**-0.29**	**-0.32**
HOH/t	**-0.50**	**-0.26**	**-0.23**	**-0.26**	**-0.30**

HOH-down/t	-0.05	-0.02	-0.05	-0.06	-0.09

[a] The estimated value for the basis set superposition error (BSSE) is ~0.05 eV.

[b] After geometry optimization, OH/f and OH/h moved to the bridge sites OH/b-f and OH/b-h.

Table 8. Binding energies[a] (eV) of ORR species at various binding sites on Os, Pt, and Pt/Os surfaces in solution.

Species	pure Os	pure Pt	Pt_{1ML}/Os	Pt_{2ML}/Os	Pt_{3ML}/Os
H/b	-2.90	-2.76	-2.46	-2.63	-2.81
H/f	**-2.94**	-2.79	-2.46	-2.62	-2.78
H/h	-2.84	-2.75	-2.44	-2.61	-2.75
H/t	-2.83	**-2.82**	**-2.61**	**-2.72**	**-2.90**
O/b	-5.08	-3.95	-3.59	-3.65	-3.87
O/f	-5.26	**-4.49**	**-3.90**	**-4.11**	**-4.27**
O/h	**-5.67**	-4.05	-3.67	-3.82	-4.01
O/t	-5.17	-3.47	-3.59	-3.22	-3.19
OH/b-f	-3.50	-2.72	-2.79	-2.51	-2.62
OH/b-h	-3.38	-2.71	-2.70	-2.61	-2.65
OH/f	Unstable[b]				
OH/h	Unstable[b]				
OH/t	**-3.72**	**-2.83**	**-3.10**	**-2.80**	**-2.83**
O_2/b	**-2.56**	**-1.05**	**-0.86**	**-0.61**	**-0.87**
O_2/f	-2.21	-0.94	-0.78	-0.59	-0.85
O_2/h	-2.40	-0.83	-0.79	-0.57	-0.72
OOH/t-b-f	unstable	-1.55	**-1.73**	-1.45	-1.56
OOH/t-b-h	unstable	**-1.58**	-1.67	**-1.52**	**-1.58**
OOH/t-f	-2.24	-1.53	-1.52	-1.46	-1.49
OOH/t-h	**-2.35**	-1.50	-1.66	-1.39	-1.52

HOOH/b	**-0.84**	**-0.68**	**-0.58**	**-0.66**	**-0.71**
HOH/t	**-0.90**	**-0.67**	**-0.63**	**-0.65**	**-0.71**
HOH-down/t	-0.51	-0.46	-0.60	-0.50	-0.49

[a] The estimated value for the BSSE is ~0.05 eV.

[b] After geometry optimization, OH/f and OH/h moved to the bridge sites OH/b-f and OH/b-h.

O binding. On the pure Os surface, O binds stronger than on the Pt or Pt/Os surfaces. The binding energy on the Os surface is -5.21 eV at the h site and ranges from -3.16 to -3.68 eV at the f site for Pt and Pt/Os.

In solvation phase, the most stable binding sites are the same as in gas phase. The differences between the O binding energy values on the Os and Pt, Pt/Os surfaces are smaller.

OH binding. In gas phase, the most stable OH binding site on the Os and Pt surfaces is the b site, whereas the t site is most stable for the Pt/Os surfaces. The binding energy on the Os surface in gas phase is -3.24 eV, which is lower than -2.31 and -2.21 to -2.29 eV for the Pt and Pt/Os surfaces, respectively. Interestingly, for all catalysts OH shows no significant binding site preference in gas phase, unlike the solvation phase where the t site is clearly preferable.

In solvation phase, the t site is the most stable for the all catalysts. The OH binding energy for the Pt_{1ML}/Os is -3.10 eV, higher than on the Os surface (-3.72 eV) but lower than on the Pt surface (-2.83 eV). The OH binding energy does not exhibit an obvious trend versus different numbers of deposited Pt layers, as the values vary from -2.80 to -3.10 eV.

O_2 binding. We use the center of the O-O bond to denote the binding sites of O_2. Thus, the O_2/b means that two O atoms are located approximately on the top of the surface Os or Pt atoms with the O-O bond center at the b site. The O_2/f and O_2/h binding sites are defined as one O atom located on

top of the Os or Pt atom, and the other at the b site with the O-O bond center at the f or h site, respectively. The O_2 binding on the Os surface is stronger than on the Pt and Pt/Os surfaces both in gas phase and solution. The bridge site is the most stable for the O_2 adsorption on all surfaces, except for the Os surface in gas phase, where O_2 binds most strongly at the h site.

We find that the O_2 binding energy differences for the b and f sites on Pt_{2ML}/Os and Pt_{3ML}/Os surfaces are as small as 0.02 eV in solvent, which means that during the ORR process, O_2 can probably be adsorbed at both sites. It was also found that the O_2 binding energy for the Pt_{2ML}/Os catalyst is higher than the O_2 binding energy for the Pt_{1ML}/Os and Pt_{3ML}/Os catalysts. The reason for this violation of the expected linear trend is not clear yet.

OOH binding. For notations of the OOH binding sites we used two or three letters. The first letter denotes a position of the first oxygen atom, the second letter denotes a position of the second oxygen atom, and the third letter denotes a position of the hydrogen atom. For example, OOH/t-b-f means that the first oxygen is located on the top of Pt or Os atom, the second oxygen atom is at the b site (actually, it is between the top and bridge sites), and the hydrogen is at the f site (see Figure 17b). For OOH/t-f or OOH/t-h, the symmetry makes the O-H bond toward right or left be the same, and therefore only two letters can be used to denote positions of the two oxygen atoms (see Figure 17c). For the OOH binding on the Os surface in gas and solvation phases, the OOH/t-b-f and OOH/t-b-h sites are both unstable and OOH spontaneously decomposes into O and OH at the top sites. We find that the OOH binding for the Pt_{2ML}/Os catalyst is weaker than that for the Pt_{1ML}/Os and Pt_{3ML}/Os catalysts, similar to the O_2 binding case.

HOOH and HOH binding. There is only one site for the HOOH binding: the two O atoms bind to two neighboring Pt atoms similar to the O_2/b case with the O-O bond parallel to the surface Pt-Pt bond. For the HOH binding, the O atom binds at the top site with the two O-H bonds parallel to the

surfaces. For the HOH-down binding, one H atom binds at the top site with the remaining O-H bond almost parallel to the surface. The HOOH and HOH binding energies both in gas and solvation phases fit the general trend described before, i.e. the binding energies rise with the increasing number of deposited Pt layers and approach the binding energies for the pure Pt surface. Furthermore, the corresponding binding energies on the Os and Pt_{3ML}/Os surfaces are lower than on the pure Pt surface.

Summarizing, we can say that the binding on the Os surface is stronger than on the Pt or Pt/Os surfaces in gas and solvated phases. The general trend both in gas phase and solution is that the binding becomes stronger when the number of deposited Pt layers increases.

4.3 Reaction Energy Barriers

Based on our previously obtained results,[59,91,108] the ORR could be divided into three fundamental stages:

I. $O_2 \rightarrow O$: dissociation of O_2 to become O, which could be either via direct O_2 dissociation: $O \rightarrow 2O$ or OOH dissociation: $OOH \rightarrow O+OH$ following OOH formation: $O_2+H \rightarrow OOH$

II. $O \rightarrow OH$: OH formation. This step could be OH formation, O hydration, or H-OOH dissociation: $O+H \rightarrow OH$, $O+H_2O \rightarrow 2OH$, $H+OOH \rightarrow 2OH$

III. $OH \rightarrow H_2O$: H_2O formation from OH generated in the second stage: $OH+H \rightarrow H_2O$

Here we consider the reactions which proceed via the Langmuir–Hinshelwood mechanism. According to our previous result, the estimated energy barrier for a hydronium ion adsorbed on the Pt surface is 0.25 eV,[108] which is consistent with other published results[117,118] and lower than the RDS barrier for pure Pt, 0.50 eV (0.37 eV, if the H-OOH-diss mechanism is realized for Pt). A co-adsorbed hydronium ion with anions has also been observed experimentally at potential higher than 0.6V (RHE).[119] Figure 19 shows the ORR pathway and potential energy surface for Os, Pt, and Os/Pt core-

shell catalysts in gas phase. The reaction energy barriers for each ORR step in gas phase are listed in Table 9.

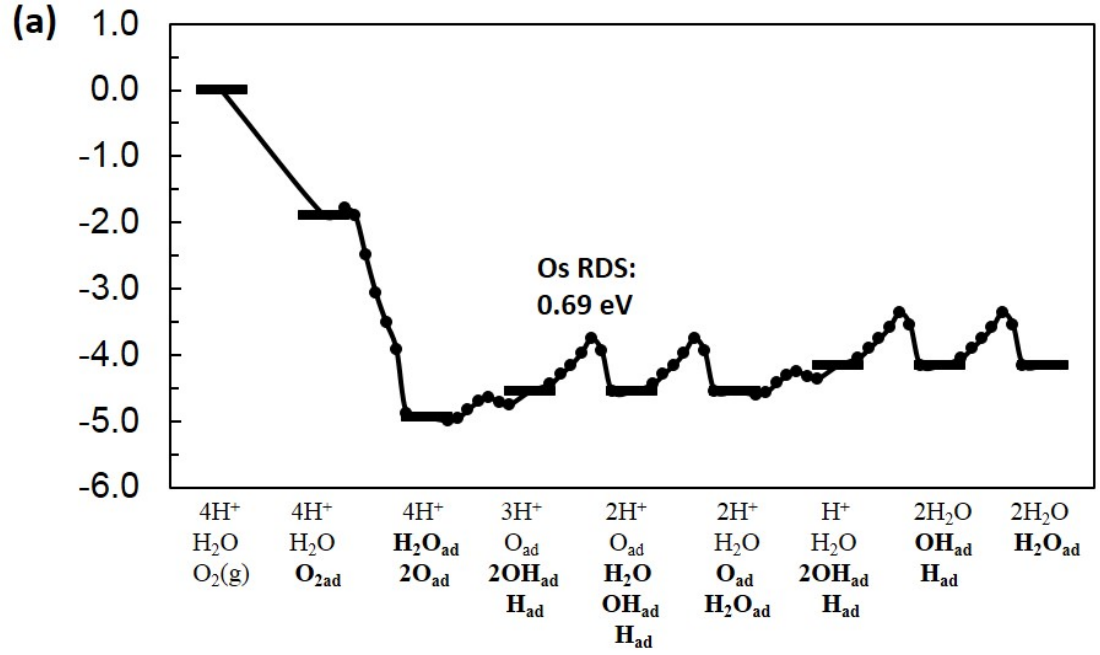

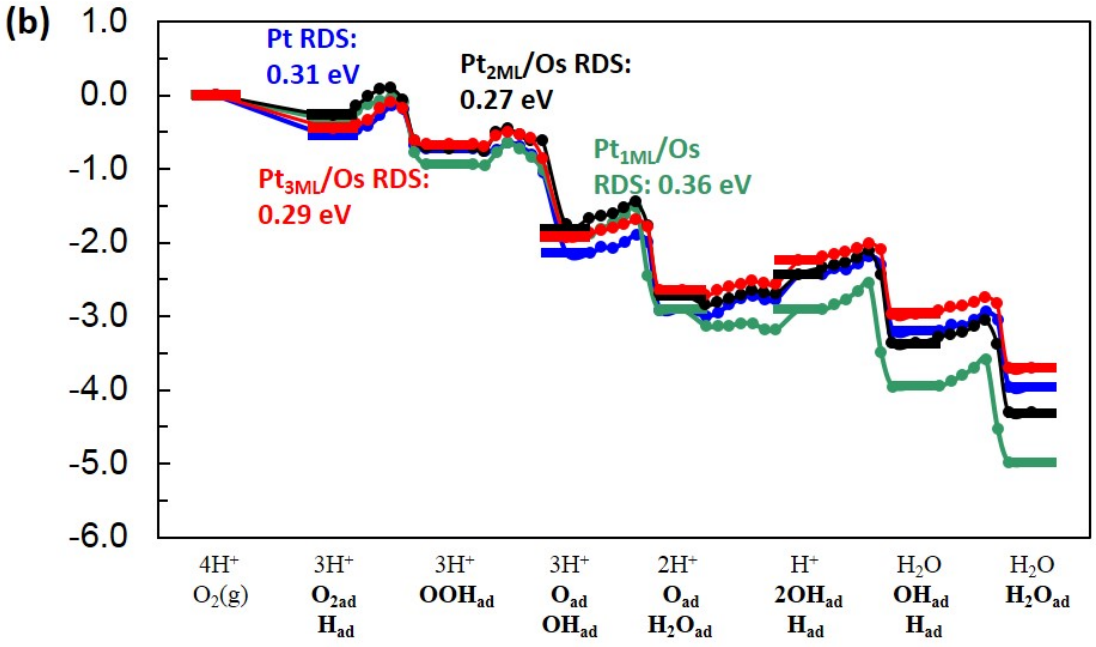

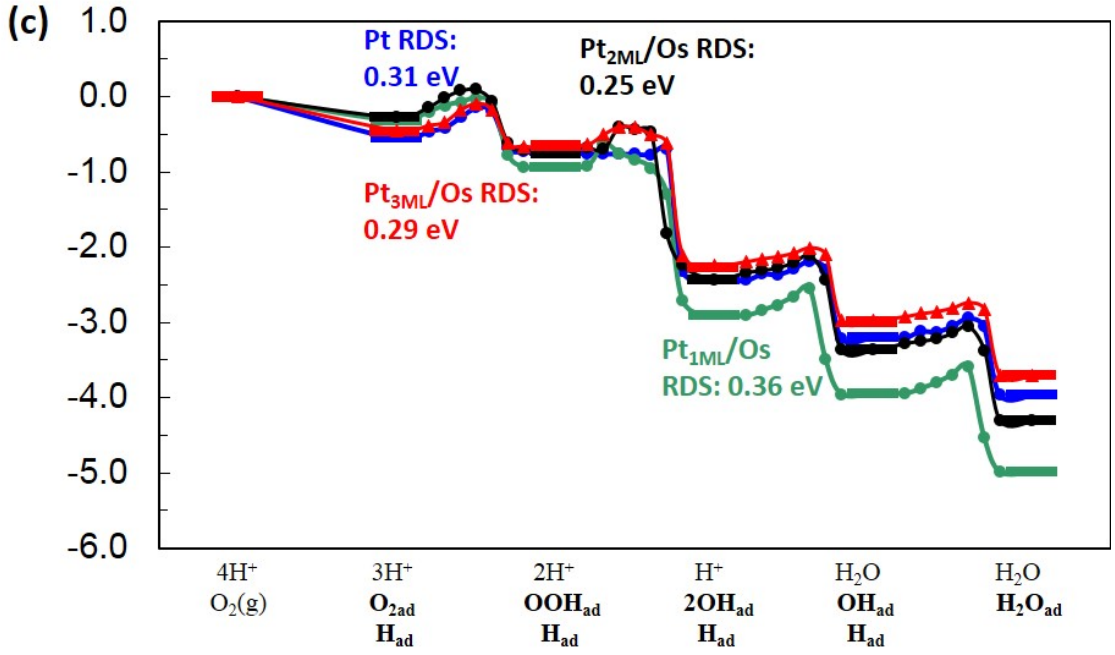

Figure 19. Potential energy surface including reaction barriers for the O_2-diss-hydr mechanism for Os (a), OOH-form-hydr mechanism (b), and H-OOH-diss mechanism (c) for Pt and Pt/Os catalysts in gas phase.

In stage I, the O_2 dissociation energy barrier is higher than the OOH formation/dissociation barriers for the Pt and Os/Pt core-shell catalysts. Thus, it is more difficult for the ORR to start from the direct O_2 dissociation, but for Os this step is favorable. This is due to the stronger O binding on the Os surface, which prompts direct O_2 dissociation.

In stage II, the direct OH formation step has a much higher barrier, which makes the oxygen hydration reaction and H-OOH dissociation more feasible, because the reaction proceeds along the lowest energy path.

Table 9. Reaction energy barriers (eV) for ORR steps on Os, Pt, and Pt/Os surfaces in gas phase.

Step	Os	Pt	Pt_{1ML}/Os	Pt_{2ML}/Os	Pt_{3ML}/Os
HH dissociation	0.16	0.00	0.24	0.20	0.13
O_2 dissociation	0.00	0.56	0.90	0.77	0.63
OH formation	1.38	0.74	0.50	0.55	0.68
H_2O formation	**0.69**	0.26	**0.36**	0.23	0.19
OOH formation	0.81	**0.31**	0.18	0.23	**0.29**
OOH dissociation	0.00	0.09	0.29	0.27	0.17
H-OOH dissociation	0.00	0.06	0.29	**0.25**	0.23
O hydration	0.35	0.27	0.04	0.20	0.19

In stage III, we find that the H_2O formation reaction energy barrier decreases, while the OOH formation energy barrier increases with the increasing number of deposited Pt layers. Thus, the RDS is a compromise between the OOH formation reaction (stage I) with the energy barrier from 0.18 to 0.31 eV and the H_2O formation reaction (stage III) with the energy barrier from 0.19 to 0.36 eV for the Pt and Os/Pt catalysts in gas phase. For pure Os, the O_2 dissociation is barrierless, but the H_2O formation has a barrier of 0.69 eV, much higher than the corresponding values for the Pt or Os/Pt catalysts. This is because of the much stronger OH binding, which makes difficult the H_2O formation reaction. Therefore, the RDS for pure Os is the H_2O formation reaction.

The ORR potential energy surface and reaction barriers in solution are shown in Figure 20 and listed in Table 10. Although the O_2 dissociation barriers are greatly reduced due to the solvent effect, the O_2 dissociation reaction and oxygen hydration reaction barriers show opposite trends versus the increasing number of deposited Pt layers. This occurs because the O binding energy in solvent rises

as the number of deposited Pt layer increases. The lower O binding energy benefits the O_2 dissociation reaction but hinders the O hydration reaction. Similar phenomena have been reported for pure metals in stage I and III.[107] The reaction energy barriers for the direct O_2 dissociation followed by the oxygen hydration reaction are higher than the barriers for the path starting from the OOH formation reaction and followed by the H-OOH dissociation reaction. Thus, the reaction path via the OOH formation is favorable for pure Pt and Os/Pt catalysts, which is in agreement with results obtained by other theoretical groups[13,117] that proposed a similar ORR mechanism for Pt. The RDS barrier is again a compromise between stage I and stage III.

Figure 21 shows the reaction energy barriers for the OOH formation reaction and H_2O formation reaction in solvated phase. The values are from Table 10. The OOH formation barrier increases with an increasing number of Pt deposited layers, while the H_2O formation barrier decreases. The two lines intersect at about 0.22 eV, which approximately corresponds to 2 ML deposited Pt. The RDS is a compromise between stage I and stage III. The best activity is observed for ~2 layers of Pt deposition.

For pure Os, the OOH formation barrier is much higher because of the stronger O_2 binding. Thus, the ORR proceeds through the direct O_2 dissociation and then the O hydration reaction. The RDS is 0.64 eV for Os, while for pure Pt, Pt_{1ML}/Os, Pt_{2ML}/Os, and Pt_{3ML}/Os the RDS is 0.37, 0.26, 0.23, and 0.35 eV, respectively. Therefore, we may expect that the ORR catalytic activity obeys the following trend, Pt_{2ML}/Os>Pt_{1ML}/Os>Pt_{3ML}/Os> Pt>Os, which allows us to consider the Os/Pt core-shell materials as potential candidates for the ORR catalysts.

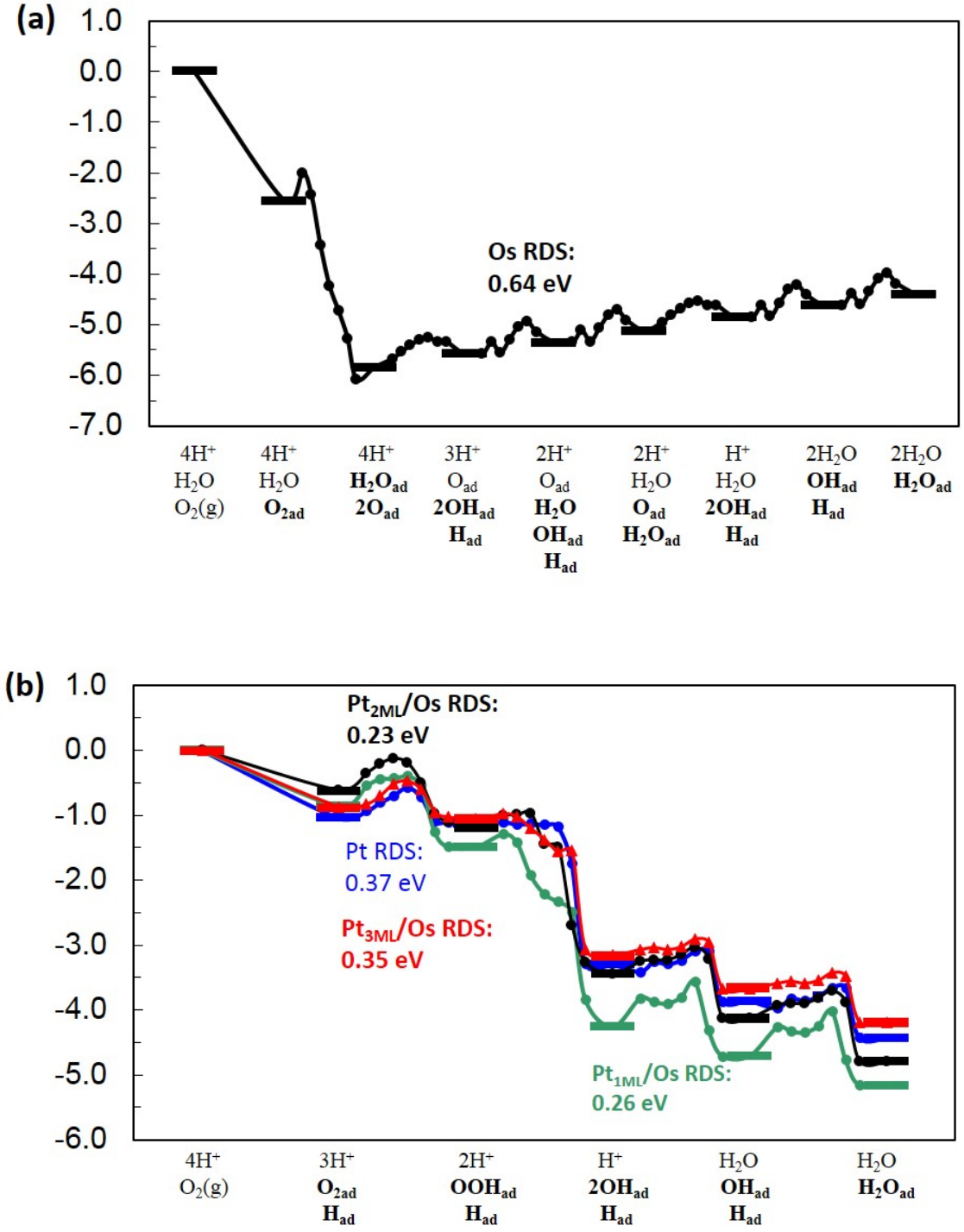

Figure 20. Potential energy surface including reaction barriers for the O_2-diss-hydr mechanism for Os (a) and H-OOH-diss mechanism (b) for Pt and Pt/Os catalysts in solution.

Table 10. Reaction energy barriers (eV) for ORR steps on Os, Pt, and Pt/Os surfaces in solution.

Step	Os	Pt	Pt_{1ML}/Os	Pt_{2ML}/Os	Pt_{3ML}/Os
HH dissociation	0.14	0.00	0.15	0.15	0.09
O_2 dissociation	0.00	0.00	0.37	0.21	0.00
OH formation	1.92	1.09	0.61	0.83	0.92
H_2O formation	**0.64**	0.32	**0.26**	0.22	0.16
OOH formation	0.87	**0.37**	0.15	**0.23**	**0.35**
OOH dissociation	0.00	0.00	0.00	0.00	0.00
H-OOH dissociation	0.00	0.00	0.00	0.04	0.00
O hydration	0.42	0.45	0.06	0.37	0.42

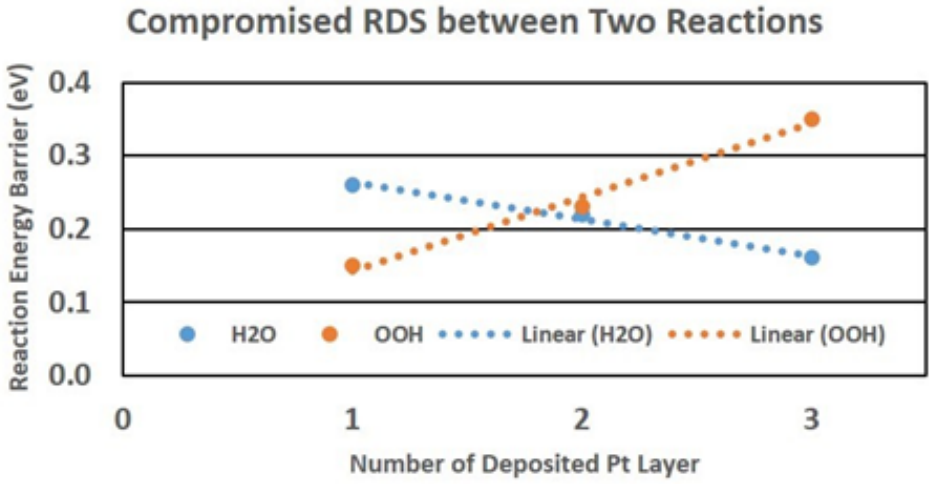

Figure 21. Reaction energy barriers for the OOH formation and H_2O formation reactions vs. a number of deposited Pt layers in solution.

Although we do not consider here the influence of the electrode potential on the ORR in detail, we have briefly analyzed the thermodynamic effect of the electrode potential by examining the Eley-Rideal mechanism. For this, we applied the approach developed by Norskøv et al.[120-122] In this approach, the reaction energy barriers are not considered properly, but assumed to be equal at least to the energy differences of the corresponding endothermic reactions, whereas the exothermic reactions are regarded as spontaneous and barrierless.

Since O_2 is not well described by DFT PBE,[121] we set the energy of the reaction $H_{2(g)}+1/2O_{2(g)}\rightarrow H_2O_{(g)}$ to the experimental value of the Gibbs free energy, –2.46 eV. Therefore, the O_2 energy could be determined by calculating the H_2 and H_2O energies as reference energies. The binding energies of the ORR species in solution (Table 8) were applied for each ORR step of the O_2-diss-hydr and H-OOH-diss mechanisms. Three potentials, 0.00, 0.80, and 1.23 V, were applied in our calculations. The ORR potential energy surfaces for the Eley-Rideal reactions are shown for the O_2-diss-hydr and H-OOH-diss mechanisms in Figures 22 and 23, respectively.

The ORR pathways obtained for the Os, Pt, and Pt/Os surfaces using the Eley-Rideal mechanism are consistent with those resulted from the Langmuir–Hinshelwood mechanism. On the Os surface, the O_2-diss-hydr mechanism is preferable, whereas on the Pt and Pt/Os surfaces, the H-OOH-diss mechanism dominates. At potential lower than 0.80 V, the ORR is almost barrierless for the Pt/Os catalysts, with a slightly higher barrier for pure Pt (0.17 eV at 0.80 V). At 1.23 V, the RDS for Pt_{1ML}/Os is the H_2O formation reaction with a barrier of 0.45 eV, while for Pt_{2ML}/Os, Pt_{3ML}/Os, and Pt, the RDS is the OOH formation reaction with a barrier of 0.23 eV, 0.42, and 0.60 eV, respectively. The RDS is again a compromise between the H_2O formation and OOH-formation reactions and Pt_{2ML}/Os is the best among the catalysts considered here.

Figure 22 (a) shows the O_2 reduction via the O_2 dissociation ($O_2\rightarrow 2O$) and O-hydration ($O+H_2O$

→2OH) on Os slab at the three different potentials. The energy difference between the first and last steps at 1.23 V is the H_2O binding energy, since we have set the energy of the reaction $H_{2(g)}+1/2O_{2(g)} \rightarrow H_2O_{(g)}$ to −2.46 eV. We find that the potential-independent O-hydration reaction (0.27 eV) determines the ORR rate at 0 V, while the H_2O formation reaction is the RDS at higher potentials (0.37 eV at 0.80 V and 0.80 eV at 1.23 V).

If we consider the O_2-diss-hydr mechanism on the Pt and Pt/Os surfaces, the O-hydration reaction is the RDS for almost all catalysts (0.65 eV for Pt, 0.31 eV for Pt_{2ML}/Os, and 0.48 eV for Pt_{3ML}/Os), except for Pt_{1ML}/Os, where the O-hydration reaction is practically barrierless and the more sluggish H_2O formation reaction retards the ORR (Figure 22 b-e and Table 10). The high barrier for the O-hydration reaction makes the ORR run via the OOH formation, H-OOH dissociation, and H_2O formation steps (Figure 23). For Os, the potential-dependent OOH formation reaction has a higher barrier than the H_2O formation reaction. Thus, the O_2-diss-hydr mechanism is more relevant for the ORR on the Os surface.

On the pure Pt surface, the OOH formation reaction, which is the RDS, has a lower barrier than the O-hydration reaction and, therefore, the H-OOH-diss mechanism is preferable on the Pt surface.

On the Pt/Os surfaces, the ORR are almost barrierless at 0 V and 0.80 V. More important is the barrier at a higher potential, because the activation region of the ORR polarization curves begins from ~ 1.00 V vs. RHE (see the ORR curves in section 4.5 Experimental Results). At 1.23 V, a compromise between the H_2O and OOH formation reactions determines the ORR rate (similar to Figure 21). The barrier for the H_2O formation reaction decreases with the increasing number of the Pt layers deposited, at 0.45, 0.12 and 0.09 eV for Pt_{1ML}/Os, Pt_{2ML}/Os, and Pt_{3ML}/Os, respectively. On the other hand, the barrier for the OOH formation reaction generally increases with the increasing number of the deposited Pt layers, at 0.26, 0.23 and 0.42 eV for Pt_{1ML}/Os, Pt_{2ML}/Os, and Pt_{3ML}/Os, respectively. The

best catalyst is, therefore, Pt_{2ML}/Os. This conclusion is consistent with our result for the Langmuir–Hinshelwood mechanism.

Summarizing, we can say that the result obtained for the Eley-Rideal mechanism generally agrees with that obtained for the Langmuir–Hinshelwood mechanism and does not affect our conclusions.

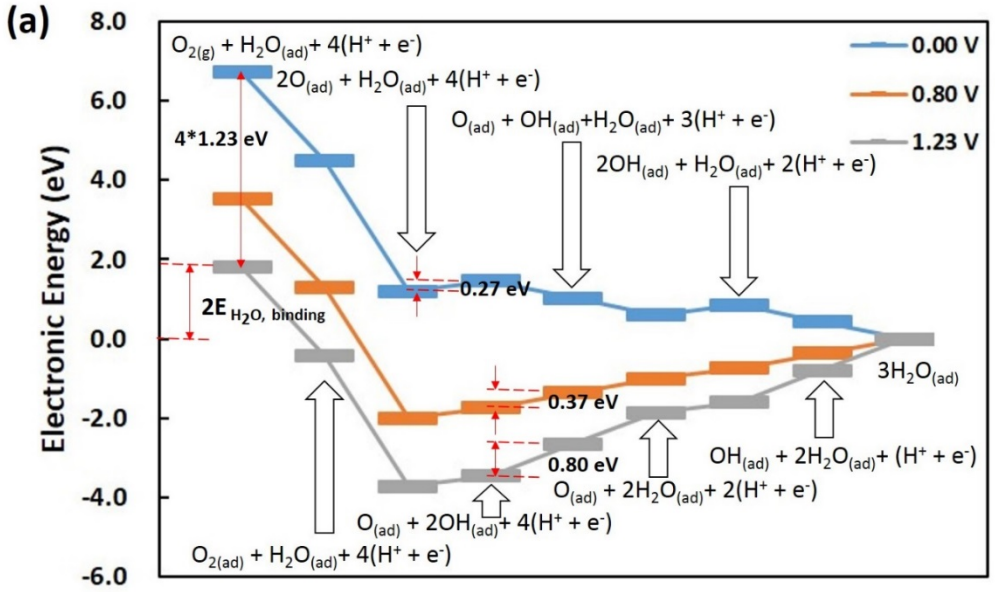

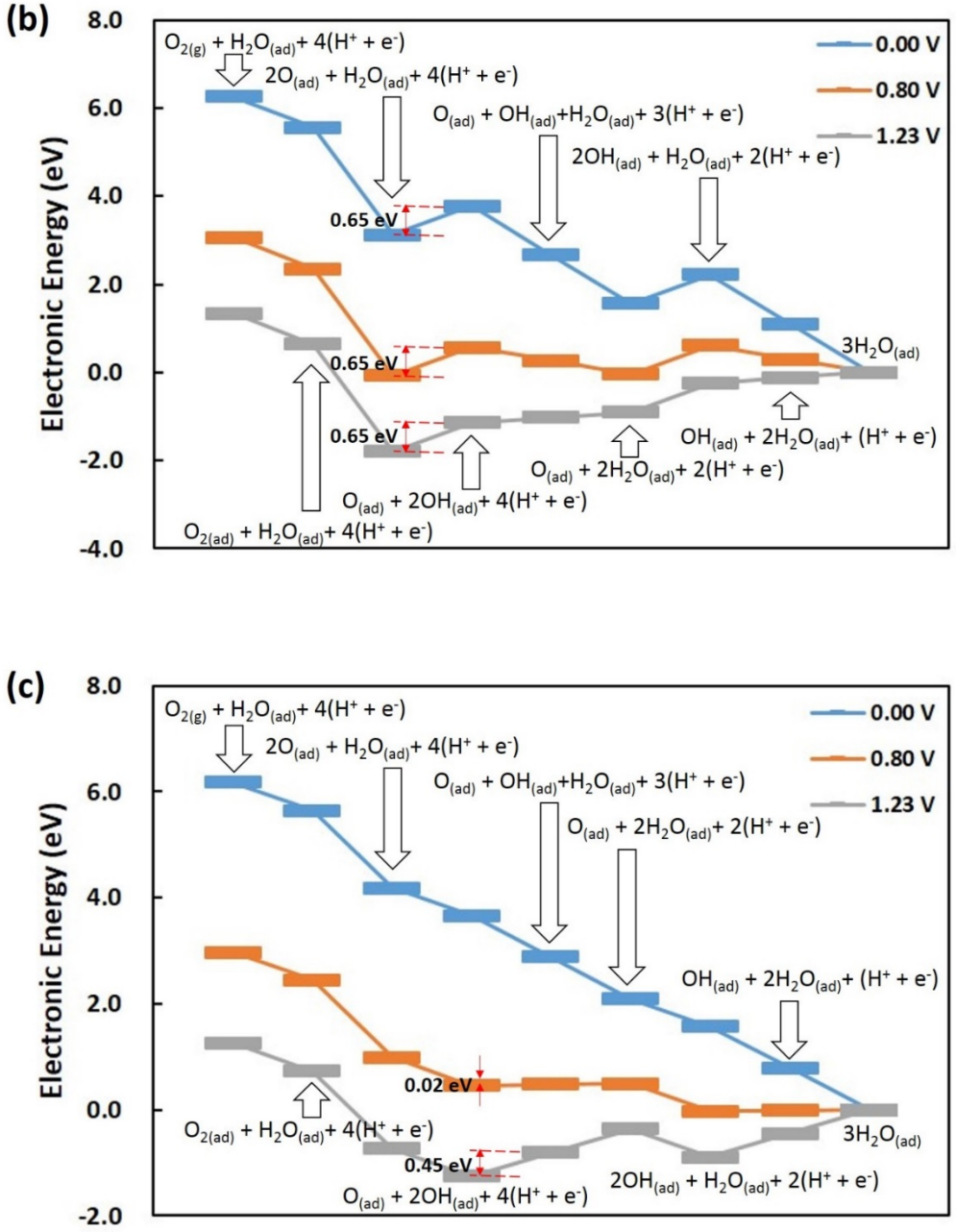
(b)
Electronic Energy (eV)
8.0
6.0
4.0
2.0
0.0
-2.0
-4.0
0.00 V
0.80 V
1.23 V
O2(g) + H2O(ad)+ 4(H+ + e-)
2O(ad) + H2O(ad)+ 4(H+ + e-)
O(ad) + OH(ad)+H2O(ad)+ 3(H+ + e-)
2OH(ad) + H2O(ad)+ 2(H+ + e-)
0.65 eV
0.65 eV
0.65 eV
3H2O(ad)
OH(ad) + 2H2O(ad)+ (H+ + e-)
O(ad) + 2H2O(ad)+ 2(H+ + e-)
O(ad) + 2OH(ad)+ 4(H+ + e-)
O2(ad) + H2O(ad)+ 4(H+ + e-)
(c)
Electronic Energy (eV)
8.0
6.0
4.0
2.0
0.0
-2.0
0.00 V
0.80 V
1.23 V
O2(g) + H2O(ad)+ 4(H+ + e-)
2O(ad) + H2O(ad)+ 4(H+ + e-)
O(ad) + OH(ad)+H2O(ad)+ 3(H+ + e-)
O(ad) + 2H2O(ad)+ 2(H+ + e-)
OH(ad) + 2H2O(ad)+ (H+ + e-)
0.02 eV
O2(ad) + H2O(ad)+ 4(H+ + e-)
3H2O(ad)
0.45 eV
2OH(ad) + H2O(ad)+ 2(H+ + e-)
O(ad) + 2OH(ad)+ 4(H+ + e-)

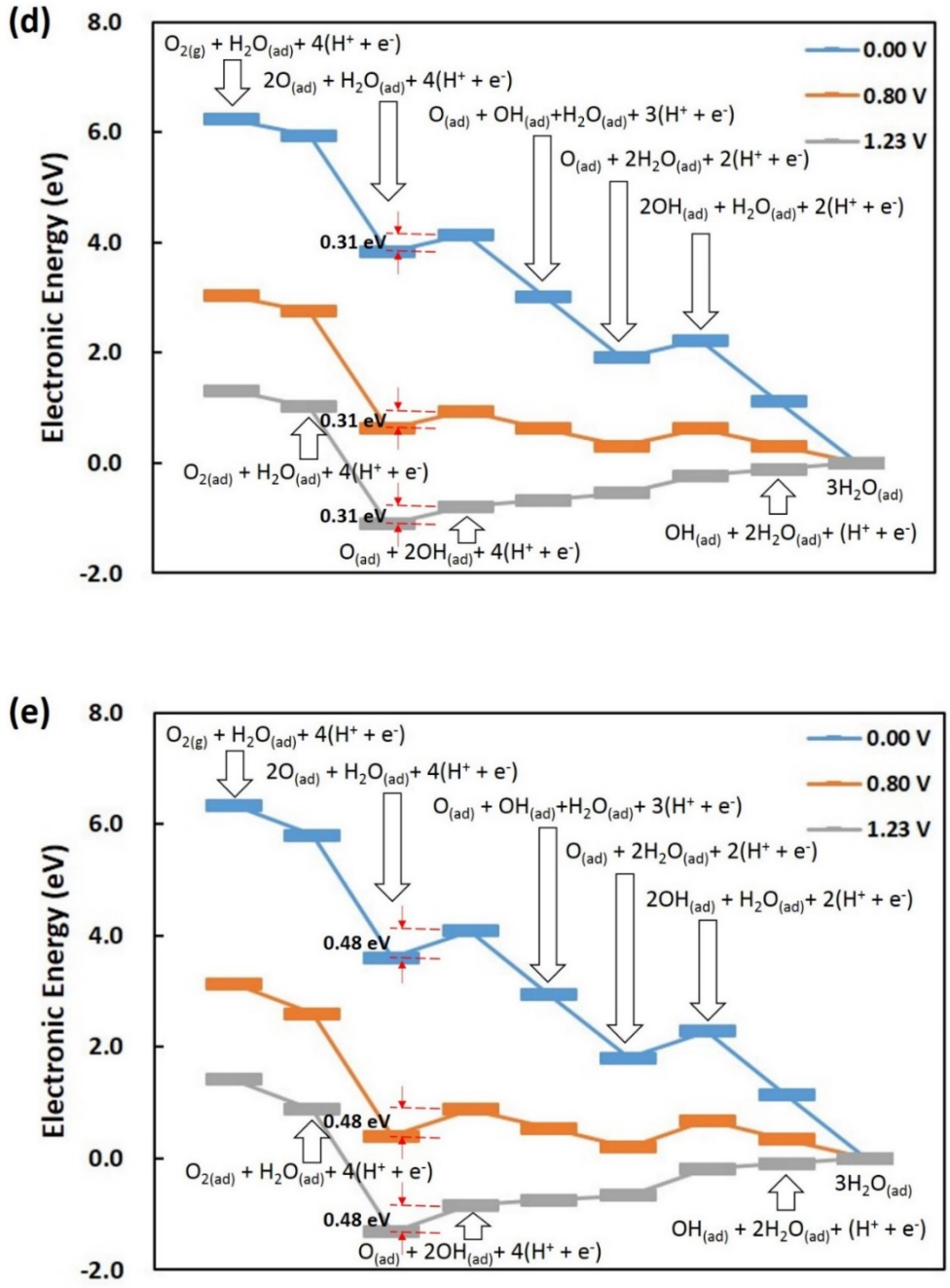

Figure 22. Potential energy surfaces for the O_2-diss-hydr mechanism for Os (a), Pt (b), Pt_{1ML}/Os (c), Pt_{2ML}/Os (d), and Pt_{3ML}/Os (e) in solution.

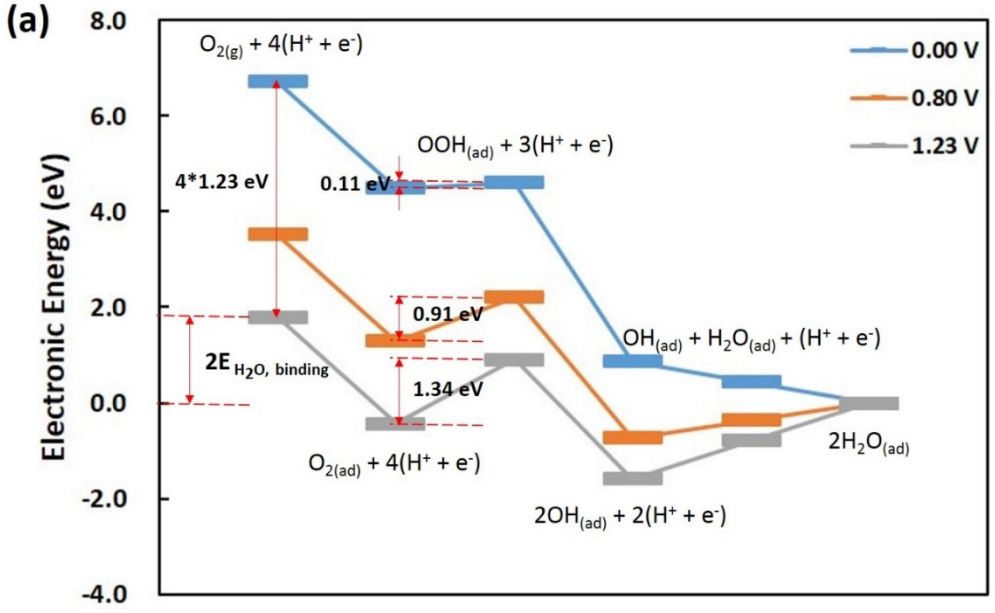
(a)
Electronic Energy (eV)
8.0
6.0
4.0
2.0
0.0
-2.0
-4.0
$O_{2(g)}$ + 4(H^+ + e^-)
$OOH_{(ad)}$ + 3(H^+ + e^-)
$OH_{(ad)}$ + $H_2O_{(ad)}$ + (H^+ + e^-)
$2H_2O_{(ad)}$
$O_{2(ad)}$ + 4(H^+ + e^-)
$2OH_{(ad)}$ + 2(H^+ + e^-)
4*1.23 eV
0.11 eV
0.91 eV
1.34 eV
$2E_{H_2O,\ binding}$
0.00 V
0.80 V
1.23 V

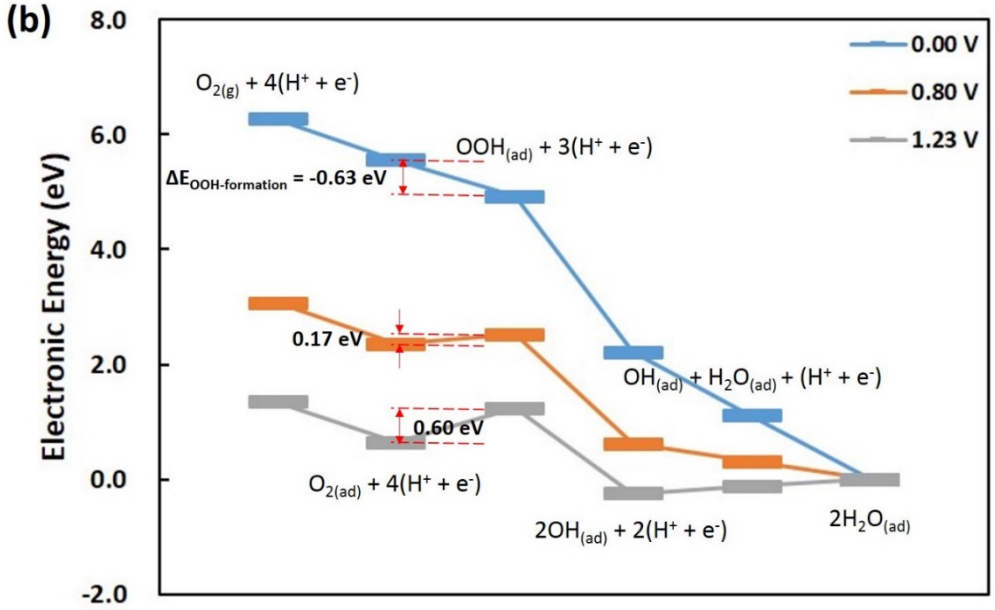
(b)
Electronic Energy (eV)
8.0
6.0
4.0
2.0
0.0
-2.0
$O_{2(g)}$ + 4(H^+ + e^-)
$OOH_{(ad)}$ + 3(H^+ + e^-)
$OH_{(ad)}$ + $H_2O_{(ad)}$ + (H^+ + e^-)
$2H_2O_{(ad)}$
$O_{2(ad)}$ + 4(H^+ + e^-)
$2OH_{(ad)}$ + 2(H^+ + e^-)
$\Delta E_{OOH\text{-}formation}$ = -0.63 eV
0.17 eV
0.60 eV
0.00 V
0.80 V
1.23 V

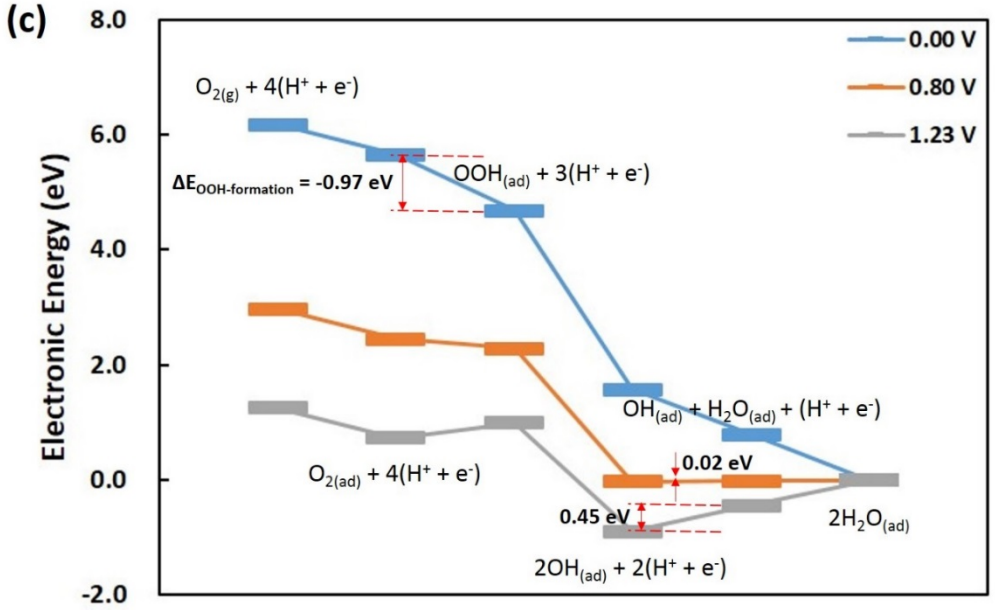
(c)
8.0
6.0
4.0
2.0
0.0
-2.0
Electronic Energy (eV)
0.00 V
0.80 V
1.23 V
O2(g) + 4(H+ + e-)
ΔEOOH-formation = -0.97 eV
OOH(ad) + 3(H+ + e-)
OH(ad) + H2O(ad) + (H+ + e-)
0.02 eV
O2(ad) + 4(H+ + e-)
0.45 eV
2H2O(ad)
2OH(ad) + 2(H+ + e-)

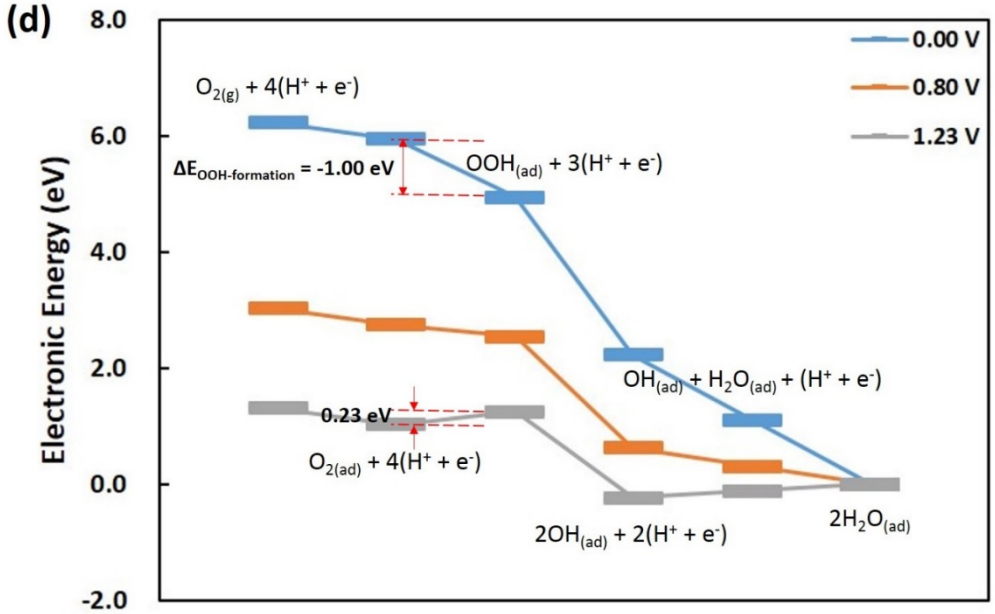
(d)
8.0
6.0
4.0
2.0
0.0
-2.0
Electronic Energy (eV)
0.00 V
0.80 V
1.23 V
O2(g) + 4(H+ + e-)
ΔEOOH-formation = -1.00 eV
OOH(ad) + 3(H+ + e-)
OH(ad) + H2O(ad) + (H+ + e-)
0.23 eV
O2(ad) + 4(H+ + e-)
2H2O(ad)
2OH(ad) + 2(H+ + e-)

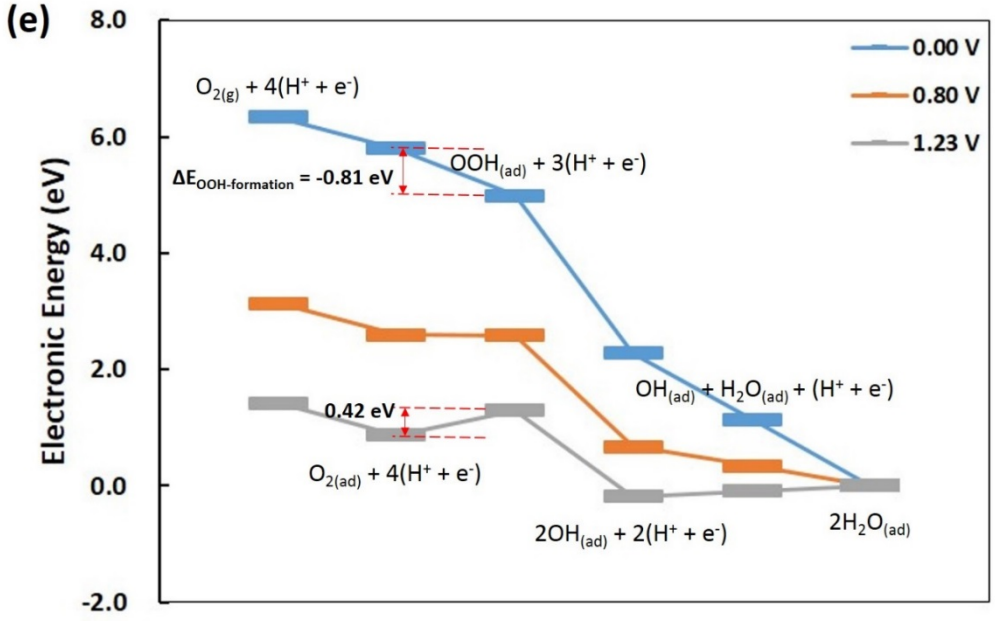

Figure 23. Potential energy surfaces for the H-OOH-diss mechanism for Os (a), Pt (b), Pt_{1ML}/Os (c), Pt_{2ML}/Os (d), and Pt_{3ML}/Os (e) in solution.

4.4 Strain and Ligand Effects

There are many publications both experimental and theoretical (see, for instance, refs 109,123,124) that discuss the strain and ligand effects for the heteroepitaxial metal layers (bimetallic overlayers). The strain effect arises due to the bond length difference between the deposited layers and the substrate, whereas the ligand effect describes the effect owing to the heterometallic bonding between the surface atoms and the substrate atoms which changes the electronic structure.

To study the strain effect, we compress the Pt bond lengths to the Os bond length value and compare the binding energies of different ORR species and reaction barriers for Pt and Pt_{3ML}/Os. Figures 24 compares the binding energies of the ORR species on the pure Pt, compressive Pt, Pt_{1ML}/Os, and Pt_{3ML}/Os surfaces in gas phase and solution (the corresponding values are listed in Tables 11 and 12, respectively). In both phases, all binding energies for Pt_{3ML}/Os are similar to those for compressive Pt, which includes the strain effect but excludes the ligand effect. On the other hand, the binding energy differences between compressive Pt and Pt_{1ML}/Os are larger. This phenomenon is more obvious in solvation phase than in gas phase.

Since the ligand effect descends versus the increasing number of deposited Pt layers, the ligand effect is more significant in Pt_{1ML}/Os than in Pt_{3ML}/Os. This result supports the viewpoint that the ligand effect of the Os substrate plays an important role. A similar conclusion could be made from the reaction energy barriers (Figure 25, Tables 13 and 14). The barrier differences between pure Pt, Pt_{3ML}/Os, and compressive Pt are lower than the differences between Pt_{1ML}/Os and compressive Pt. This implies that the ligand effect of the Os substrate rather than the strain effect is responsible for the improved ORR catalytic activity. The RDS barrier becomes higher and approaches the value

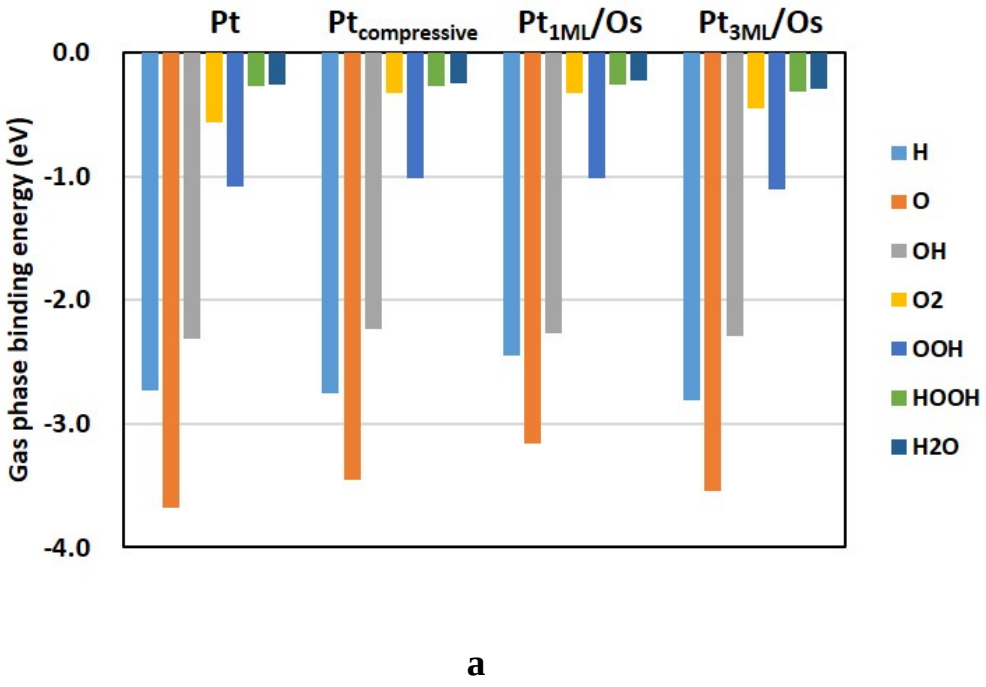

a

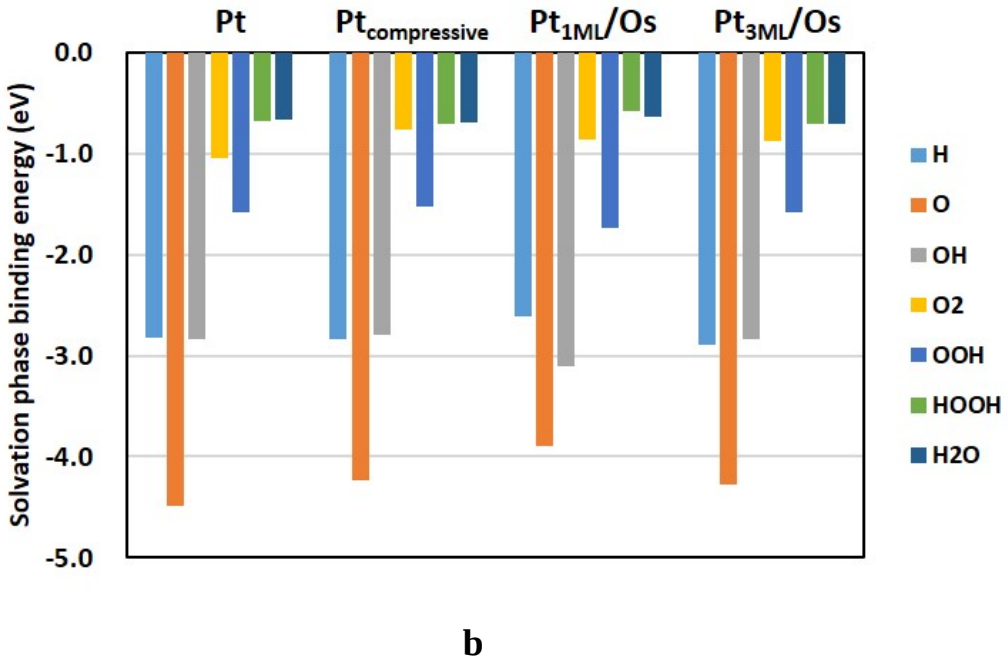

b

Figure 24. Binding energies of ORR species for Pt, compressive Pt, and Pt/Os surfaces in gas phase (a) and solution (b).

Table 11. Binding energies[a] (eV) of ORR species on Pt, compressive Pt, and Pt/Os surfaces in gas phase.

Species	Pt	compressive Pt	Pt_{1ML}/Os	Pt_{3ML}/Os
H	-2.73	-2.76	-2.45	-2.81
O	-3.68	-3.45	-3.16	-3.55
OH	-2.31	-2.23	-2.27	-2.29
O_2	-0.56	-0.33	-0.33	-0.45
OOH	-1.09	-1.02	-1.02	-1.11
HOOH	-0.27	-0.27	-0.26	-0.32
HOH	-0.26	-0.25	-0.23	-0.30

[a] The estimated value for the BSSE is ~0.05 eV.

Table 12. Binding energies[a] (eV) of ORR species on Pt, compressive Pt, and Pt/Os surfaces in solution.

Species	Pt	compressive Pt	Pt_{1ML}/Os	Pt_{3ML}/Os
H	-2.82	-2.84	-2.61	-2.90
O	-4.49	-4.23	-3.90	-4.27
OH	-2.83	-2.79	-3.10	-2.83
O_2	-1.05	-0.77	-0.86	-0.87
OOH	-1.58	-1.53	-1.73	-1.58
HOOH	-0.68	-0.70	-0.58	-0.71
HOH	-0.67	-0.69	-0.63	-0.71

[a] The estimated value for the BSSE is ~0.05 eV.

for pure Pt with the increasing number of deposited Pt layers (see Table 10). Earlier, it was explained by weakening of the ligand effect, when the number of deposited Pt layers increases.[124]

The ligand effect can be seen in Figure 24, Tables 11 and 12. We find that Pt_{3ML}/Os, which experiences a weaker ligand effect than Pt_{1ML}/Os, has similar binding energy values with compressive Pt. In general, the ligand effect, as well as the strain effect, weakens the ORR species binding on the Os/Pt core-shell structure compared to pure Pt. However, too weak binding of certain ORR intermediates may result in a higher barrier for the critical reaction. That is why Pt_{2ML}/Os, which has the binding energy closer to the optimal value than Pt_{1ML}/Os, shows better ORR activity than Pt_{1ML}/Os (see Figure 21, which shows a compromise between the OOH formation and H_2O formation steps).

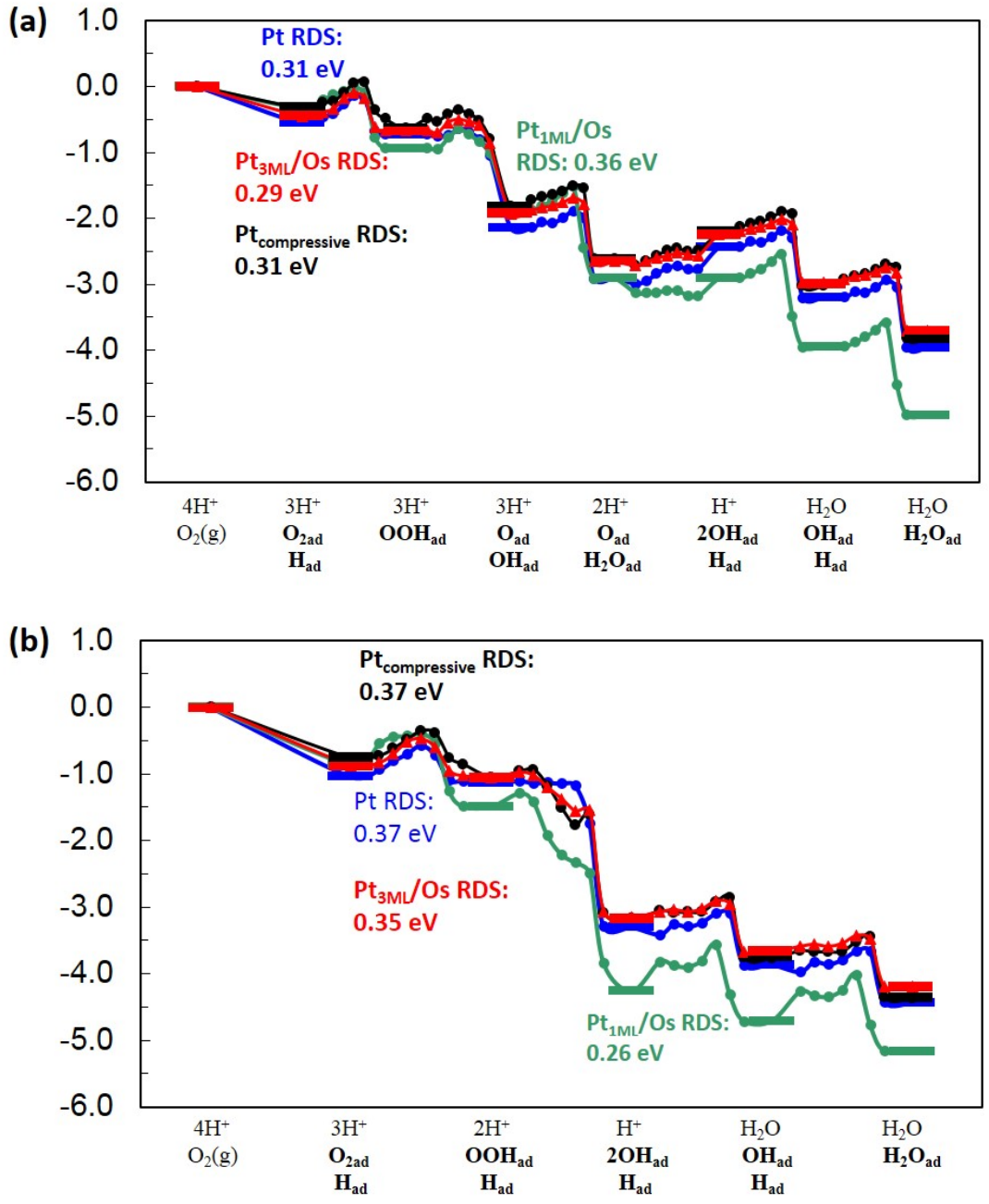

Figure 25. Potential energy surface including reaction barriers of H-OOH-diss-hydr mechanism for Pt, compressive Pt, and Pt/Os catalysts in gas phase (a) and solution (b).

Table 13. Reaction energy barriers (eV) for ORR steps on Pt, compressive Pt, and Pt/Os surfaces in gas phase.

Step	Pt	Compressive Pt	Pt_{1ML}/Os	Pt_{3ML}/Os
HH dissociation	0.00	0.00	0.24	0.13
O_2 dissociation	0.56	0.63	0.90	0.63
OH formation	0.74	0.69	0.56	0.68
H_2O formation	0.26	0.22	**0.36**	0.19
OOH formation	**0.31**	**0.31**	0.18	**0.29**
OOH dissociation	0.09	0.14	0.29	0.17
H-OOH dissociation	0.06	0.24	0.29	0.23
O hydration	0.27	0.27	0.04	0.19

Table 14. Reaction energy barriers (eV) for ORR steps on Pt, compressive Pt, and Pt/Os surfaces in solution.

Step	Pt	Compressive Pt	Pt_{1ML}/Os	Pt_{3ML}/Os
HH dissociation	0.00	0.00	0.15	0.09
O_2 dissociation	0.00	0.00	0.37	0.00
OH formation	1.09	0.92	0.61	0.92
H_2O formation	0.32	0.21	**0.26**	0.16
OOH formation	**0.37**	**0.37**	0.15	**0.35**
OOH dissociation	0.00	0.00	0.00	0.00
H-OOH dissociation	0.00	0.03	0.00	0.00
O hydration	0.45	0.47	0.06	0.42

4.5 Experimental Results

A HAADF STEM image for the Pt_{2ML}/Os/C particle is shown in Figure 26 (a). Although the HAADF technique could supply clear contrast for interface/locations because of various element distributions,[55] some HAADF STEM images do not show clear core-shell structure contrast, like in our case where the atomic number variation (Z contrast) is not significant, as was discussed earlier.[55,125,126] Figure 26 (b) shows the element profile analysis for a Pt_{2ML}/Os/C nanoparticle from the STEM-EDS measurement with a probe size of about 1.5 Å. As shown, Pt_{2ML}/Os/C revealed a core-shell structure in which the core consisted of Os atoms whereas the shell was predominately occupied by the Pt atoms.

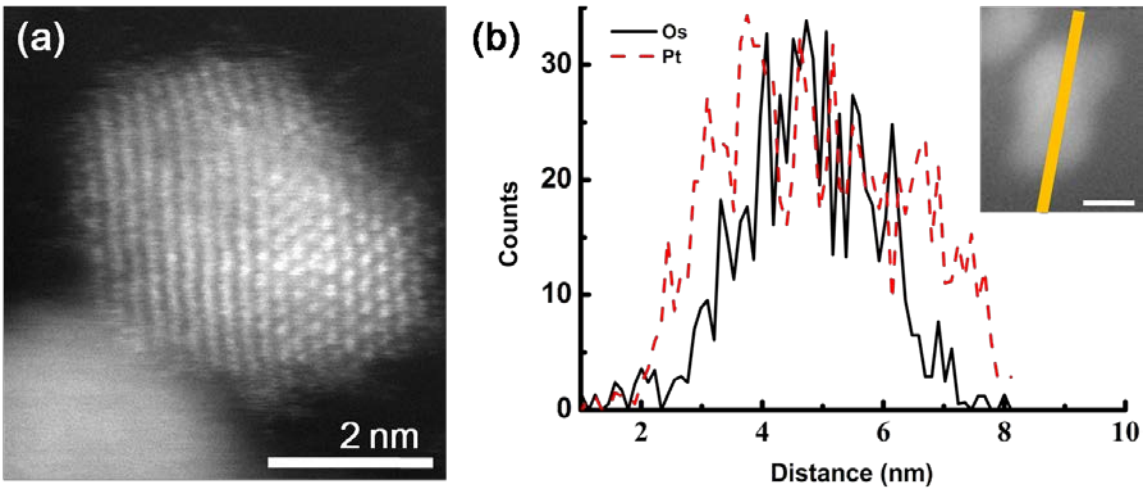

Figure 26. The HAADF STEM image (a) and EDS line-scan of a Pt_{2ML}/Os/C nanoparticle (b).

Figure 27 shows the CV curves of Os/C, Pt_{1ML}/Os/C, Pt_{2ML}/Os/C, and Pt/C for ECSA determination by hydrogen adsorption. The ECSA values for Pt/C, Pt_{1ML}/Os/C, and Pt_{2ML}/Os/C

were 2.39, 1.18, and 1.88 cm_{Pt}^2, respectively. The Pt/Os/C catalysts and pure Pt have different adsorption behavior, because the modified structure weakens the interaction between adsorbates and catalyst surfaces,[127] which can also be seen in Tables 7 and 8. By increasing the thickness of the Pt overlayer, the current densities at the double layer region (0.3 ~ 0.6 V vs. RHE) are decreased (see Figure 28). The increased current densities at the double layer region of Pt_{1ML}/Os/C is possibly due to the oxidation of incompletely covered Os, similar to the Ru/Pt catalyst.[61] Therefore we reasonably concluded that the Pt in Pt_{1ML}/Os/C did not cover the entire Os surface, but in the case of Pt_{2ML}/Os/C, the surface was more completely covered by the Pt atoms. This is anticipated because even in a straightforward displacement reaction process, the stoichiometric ratio of Cu:Pt was 1:1, and previous literature reported that the galvanic displacement did not form a continuous layer but a fine structure with some nano-voids or 2ML high deposit at some spots[76] or the deposit formed by interconnected Pt islands with some holes.[78,128] A similar 3D island structure was also observed by using the extended X-ray adsorption fine structure (EXAFS) analysis applied for Pt/Rh(0001)[63] and Au/Pd[129] samples, which were prepared via the Cu UPD displacement process. The island structure formation might be due to the incomplete Cu UPD shell structure before galvanic displacement.[130] Furthermore, some references reported the Cl^- as a strong complexing ligand, promoting the stability of Cu(I) over Cu(II),[131,132] which makes the stoichiometric ratio greater than one. Therefore, the Os bare surface of the Pt_{1ML}/Os/C catalyst is not fully covered by Pt deposit, but the Pt_{2ML}/Os/C has much better Pt coverage. The incomplete coverage decreases the stability of the Pt/Os/C catalysts. However, in Chapter 3, we reported that the stability of dealloyed Pt-Os nanoparticles after 10000 CV cycles was better than that of pure Pt. This implies that with complete Pt coverage, which could be reached by using another technique, Pt/Os core-shell catalysts may have a good enough stability.

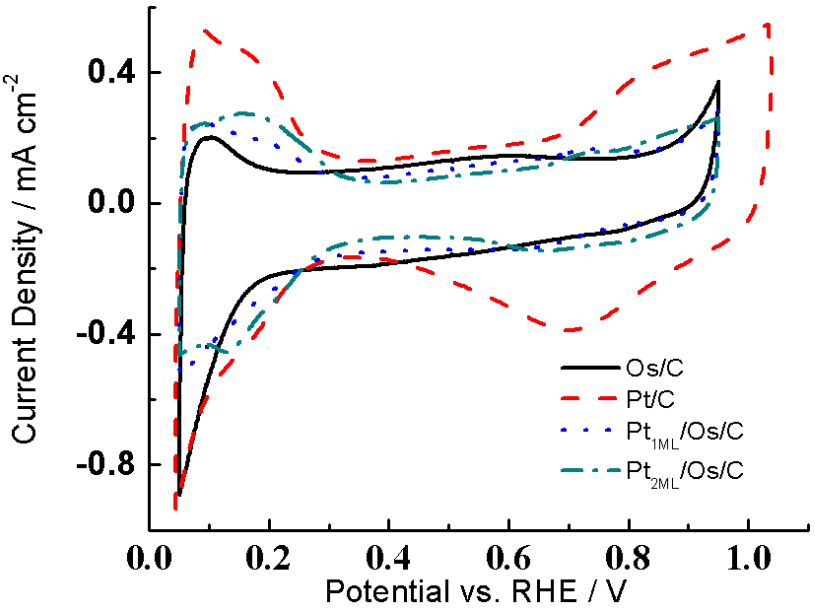

Figure 27. The CV curves for ECSA determination for Os/C, Pt/C, Pt_{1ML}/Os/C, and Pt_{2ML}/Os/C, respectively. The electrolyte was deaerated 0.1 M aqueous $HClO_4$.

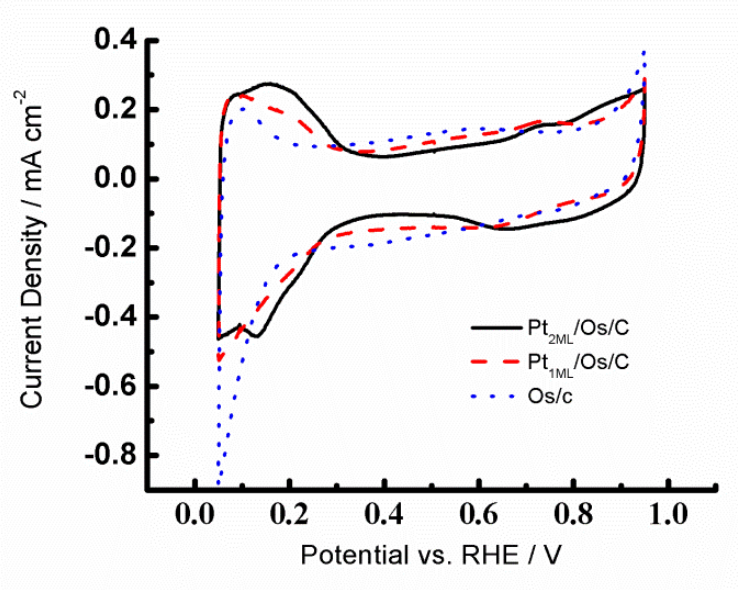

Figure 28. The CV curves for ECSA determination for Os/C, Pt_{1ML}/Os/C, and Pt_{2ML}/Os/C, respectively. The electrolyte was deaerated 0.1 M aqueous $HClO_4$.

Figure 29 demonstrates the ORR CV curves in apparent current density for Pt_{1ML}/Os/C, Pt_{2ML}/Os/C, and Pt/C. At potential below 0.6 V, the ORR response is under mass transport control limited by the diffusion of the dissolved oxygen in the electrolyte, whereas at potential between 0.8 and 1 V, the ORR response is dominated by kinetics (the electrocatalytic activity of the electrocatalyst involved in the ORR process).[111] Therefore, a simple method to quickly evaluate the ORR behavior of a potential electrocatalyst is the reading of half-wave potential, which is defined as the potential at which the magnitude of the current is half of the limiting current. In general, the larger the half-wave potential, the greater the ORR activity. As shown, the half-wave potentials for the Pt/C, Pt_{1ML}/Os/C, and Pt_{2ML}/Os/C were 876, 795, and 918 mV, respectively. It should be noted that the diffusion-limiting current for these samples at a rotation speed of 1600 rpm was close to 6 mA cm^{-2}, which is consistent with the value earlier reported.[133] This consistence indicated that our ORR experiments were carried out properly.

To extract the kinetic information, we employed the Kouteck-Levich equation (see section 3.6) again. The respective kinetic parameters are listed in Table 15. As it was mentioned above, the Os core of Pt_{1ML}/Os/C is not fully covered by Pt atoms. According to our solvation calculation (Table 10), the ORR at the Os surface is very sluggish because of the high H_2O formation reaction energy barrier due to the strong OH binding. This causes the catalytic performance of Pt_{1ML}/Os/C, which is not completely covered by Pt, to be even worse than that of the commercial Pt catalyst. The Pt_{2ML}/Os/C sample, which is more completely covered by Pt atoms and shows a core-shell structure, exhibits excellent catalytic activity. It is in agreement with the low reaction energy barriers for the Pt_{1ML}/Os and Pt_{2ML}/Os catalysts (Table 10) from our computational evaluations.

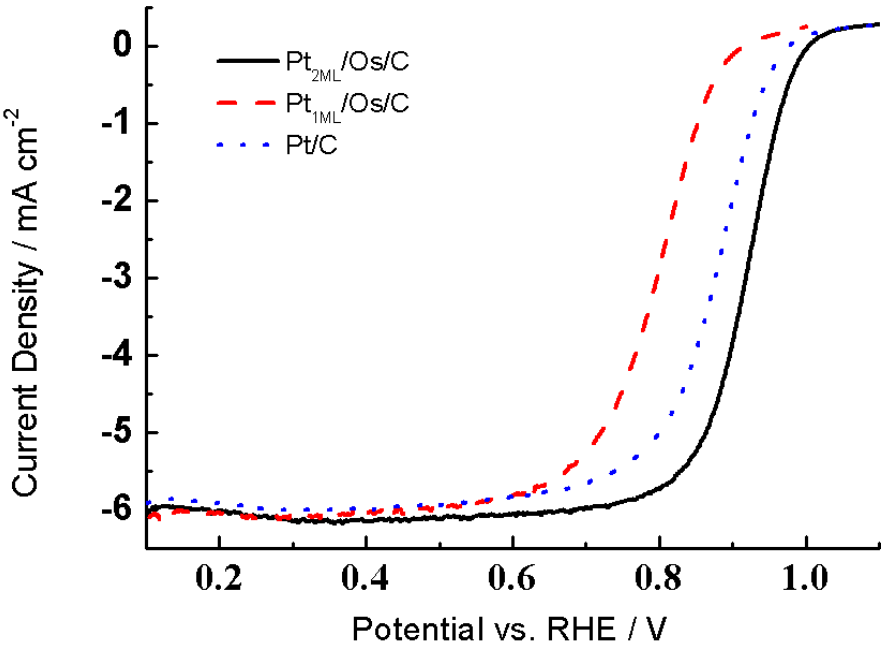

Figure 29. The ORR curves of Pt/C, Pt_{1ML}/Os/C, and Pt_{2ML}/Os/C in apparent current density. The electrolyte is oxygen-saturated 0.1 M aqueous $HClO_4$ solution and the scan rate is 20 mV/s.

Table 15. The comparison of kinetic data for ORR Os/Pt core-shell catalysts.

Catalyst	Pt loading (μg)	Imass (mA μg_{Pt}^{-1})	I_{mass} (mA μg_{Pt+Os}^{-1})	$i_{specific}$ (mA cm_{Pt}^{-2})	Half wave potential (V vs RHE)
Pt/C	3	-0.20	-0.20	-0.26	0.876
Pt_{1ML}/Os/C	1.42	0	0	0	0.795
Pt_{2ML}/Os/C	2.82	-0.70	-0.45	-1.33	0.918

Figure 30 shows correlation between the experimental half wave potential and theoretically calculated OH binding energy. Previous experimental studies[28] indicate good agreement with a theoretical study in which the maximum activity corresponds to the surface that could bind OH by ~0.1 eV weaker than Pt.[134,135] Our results indicate that the highest activity occurs at Pt_{2ML}/Os/C, where the corresponding OH binding is slightly (by ~0.03 eV) weaker than for Pt. This is a relatively rough approximation, but still a good way to find correlation between the theoretical prediction and experimental result. In Figure 31, we use the calculated RDS for comparison with the experimental half wave potential. To fix the UPD coverage issue (Pt atoms partially cover the Os core), we used the average value of the RDS barriers for pure Os and Pt_{1ML}/Os (Table 10) as the RDS barrier for Pt_{1ML}/Os/C and the average value of the RDS barriers for Pt_{1ML}/Os and Pt_{2ML}/Os as the RDS barrier for Pt_{2ML}/Os/C. The higher barrier corresponds to the smaller half wave potential, and the correspondence looks good enough, although it is based on a rough approximation and assumption. Indeed, Pt_{2ML}/Os/C shows 3.5 times better mass activity, when considering only Pt loading, and 5 times better specific activity for ORR compared to those of Pt/C (Table 15 and Figure 32). Considering a total precious metal loading (Pt+Os), Pt_{2ML}/Os/C shows over 2 times better activity (Figure 32).

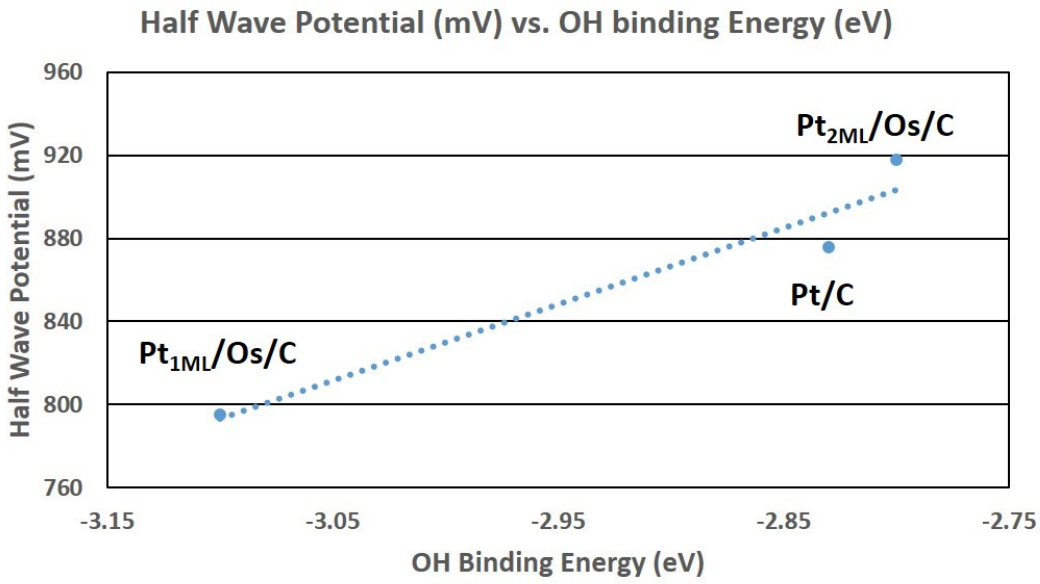

Figure 30. Experimental half wave potential vs. the theoretically predicted OH binding energy in solution.

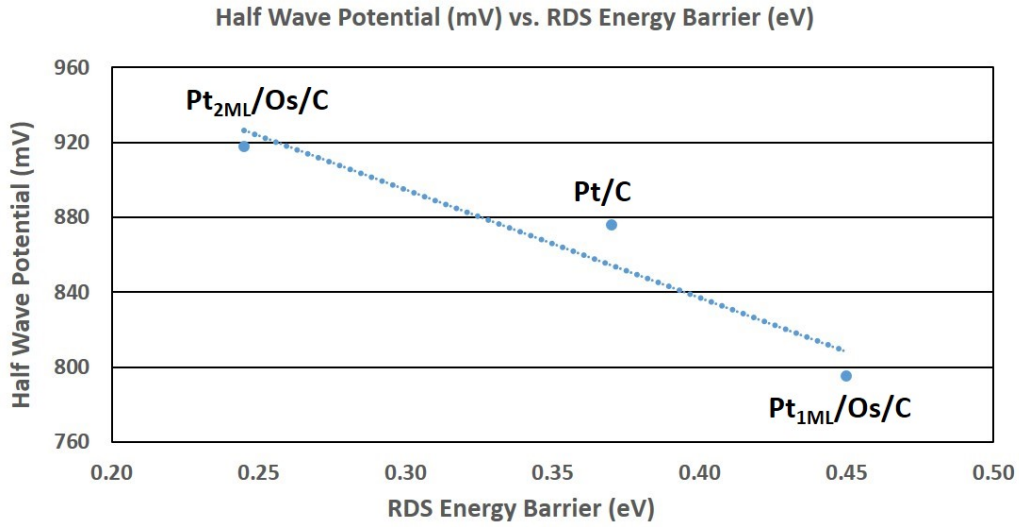

Figure 31. Experimental half wave potential versus the theoretical RDS reaction barrier in solution.

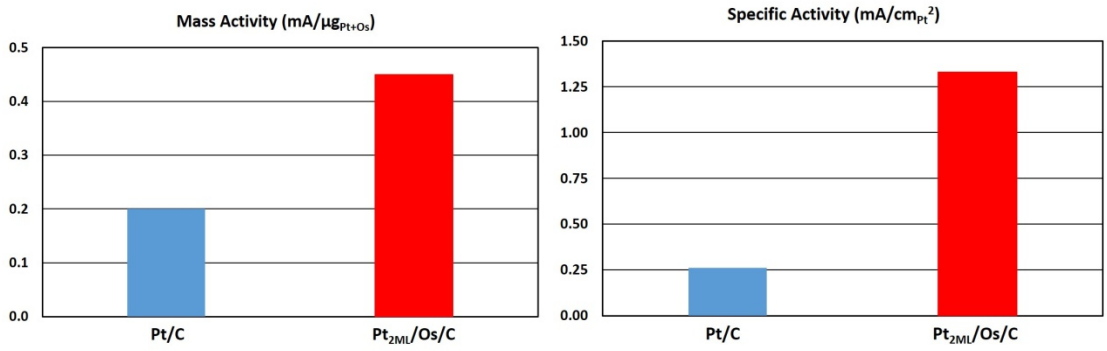

Figure S8. The total precious mass (left) and specific (right) activity of Pt/C and Pt_{2ML}/Os/C at 0.9 V (vs. NHE).

4.6 Summary for Os/Pt Core-Shell Catalysts

We applied both QM calculations and electrochemical measurements to evaluate the catalytic activity of the Pt/Os/C catalysts. Using QM calculations, we identified the most stable structures for various layer Pt deposits on the Os substrate and these structures were applied to calculate binding energies and reaction energy barriers for the ORR species. In general, the binding energy increases with the number of Pt deposit layers and approaches the values on the pure Pt surface both in gas phase and solution. This result confirms that the ligand effect gradually decreases as the number of Pt deposit layers increases. The calculated RDS barriers predict the ORR catalytic activity as following: Pt_{2ML}/Os>Pt_{1ML}/Os>Pt_{3ML}/Os>Pt>Os. To further understand the origin of the higher catalytic activity of the Pt/Os surfaces, a non-physical compressive Pt system was built to compare its reaction energy barriers and binding energies to Pt, Pt_{1ML}/Os and Pt_{3ML}/Os. The results implied that due to changes in the electronic structure of the Pt/Os catalysts, the ligand effect might be more important for the improved ORR activity than the purely compressive strain effect.

Pt/Os/C catalysts were fabricated by the chemical synthesis and UPD method. TEM technologies were applied for materials characterization. The CV curve for Os, Pt_{1ML}/Os/C, and Pt showed that in Pt_{1ML}/Os /C, the Os substrate is only partially covered by Pt atoms. The more complete Pt coverage is formed after the second UPD process. The SEM-EDS analysis proved the existence of the core-shell structure for our Pt_{2ML}/Os/C catalyst. The ORR CV curves demonstrate that the Pt_{2ML}/Os/C structure shows 3.5 to 5 times better catalytic activity than Pt/C, which allows the Os/Pt core-shell structured materials to be considered as a potential ORR catalyst. The experimentally observed ORR catalytic activity follows the sequence: Pt_{2ML}/Os/C > Pt/C > Pt_{1ML}/Os/C, which agrees with our theoretical prediction, based on the ORR energy barrier calculations.

Chapter 5

Conclusions

The fuel cell technology has a potential to solve many energy related problems due to its high efficiency and low pollution merits. However, the sluggish ORR at cathode limits its performance. Therefore, various catalysts, including Pt based metal catalysts and NPM catalysts, were developed to improve the ORR activity. Even though the high cost of the Pt based metal catalysts is a big problem for wide commercialization of these catalysts, the unsatisfactory stability issues of NPM catalysts limits the application of NPM catalysts to replace Pt based catalysts. To date, developing a low cost, high efficiency, and great stability catalyst is still the most important target in the fuel cell area.

Among the Pt based catalysts, Pt_3M alloys demonstrates superior activity when compared to pure Pt because of the formation of Pt-skin structure. Unfortunately, these reported Pt_3M alloys showed fast performance degradation due to the dissolution of their NPM elements during fuel cell operation. The dissolution is a consequence of the NPM element migration to the catalyst surface and subsequent reactions with acidic electrolyte during the ORR operation. Therefore, Pt_3M alloys that show a good surface segregation with ORR species adsorbed on their surfaces are potential candidates for the ORR catalyst. To find these potential candidates, we performed the surface segregation study of 28 Pt_3M alloys and found that only Pt_3Os and Pt_3Ir may show a good surface segregation under the fuel cell operation environment. However, Pt-Ir could not formed a homogeneous alloy at lower temperature. Thus, we focused on the Pt_3Os alloy considering it as a possible candidate for the ORR catalyst.

Our studies of the ORR species binding energies and reaction energy barriers predicted that Pt_3Os has slightly higher activity than pure Pt. The improved activity could be ascribed to the synergetic effects of compressive strain and the electronic structure modification by the underlying Os atoms. The d-band center shift explained the reduced O/OH binding energy and the better activity of Pt_3Os catalyst. Our barrier calculation showed the RDS for Pt_3Os and Pt is O hydration step (($O_{ad} + H_2O_{ad} \rightarrow OH_{ad} + OH_{ad}$) for both cases. The barrier for Pt of 0.50 eV is decreased to 0.48 eV for Pt_3Os, which would improve the activity by 218%. To validate our theoretical prediction, we prepared the DA-Pt_2Os catalysts by the dealloying method. The electrochemical analysis showed that the DA-Pt_2Os has ~2 times better activity than pure Pt and possesses 272% better stability, which confirmed our theoretical predictions.

To further improve the Pt-Os catalyst activity, we modified the surface structure of this type of catalysts. We used UPD method to fabricate Os/Pt core-shell catalysts. The surface structure energy calculation determined the stacking series of our Os/Pt slab. The ORR species binding energy calculation, as well as ORR barrier analysis, were performed to evaluate the catalyst activity. Our theoretical study showed that the ORR activity is a compromise between the OOH formation step (0.23 eV for Pt_{2ML}/Os and 0.37 eV for Pt) and H_2O formation step (0.22 eV for Pt_{2ML}/Os and 0.32 eV for Pt). With too weak O/OH binding energy, the OOH formation step dominates ORR, while for too strong O/OH binding energy the high H_2O formation barrier limits catalyst activity. The results predicted that the Pt_{2ML}/Os catalyst, which has the optimum O/OH binding energy because of suitable ligand effect resulting from the Os core, have better activity than Pt, Pt_{1ML}/Os, Pt_{3ML}/Os, or Pt_3Os. We concluded that our results based on the Langmuir–Hinshelwood mechanism are consistent with the results obtained by other groups for the Eley-Rideal mechanism. Experimental material characterizations for our catalyst proved its core-shell structure feature. The electrochemical analysis showed that the activity of Pt_{2ML}/Os/C in 0.1M $HClO_4$ solution at $25^{O}C$ has 3.5 to 5 times

better activity than commercial Pt catalyst, which validated our theoretical prediction, while Pt_{1ML}/Os/C has worse activity than Pt because its Os core was incompletely covered by Pt. The correlation between experimental half potential and theoretical OH binding energy/RDS energy barrier showed good correspondence, although it was based on rough approximation and assumption.

In this thesis, we successfully predict the Pt-Os catalyst activity and validated by experimental results. Our Pt-Os catalyst case demonstrates the possibility of using the basic QM method and simple Langmuir–Hinshelwood mechanism to evaluate the catalyst performance without losing the accuracy.

BIBLIOGRAPHY

[1] Borup, R.; Meyers, J.; Pivovar, B.; Kim, Y. S.; Mukundan, R.; Garland, N.; Myers, D.; Wilson, M.; Garzon, F.; Wood, D.; Zelenay, P.; More, K.; Stroh, K.; Zawodzinski, T.; Boncella, J.; McGrath, J. E.; Inaba, M.; Miyatake, K.; Hori, M.; Ota, K.; Ogumi, Z.; Miyata, S.; Nishikata, A.; Siroma, Z.; Uchimoto, Y.; Yasuda, K.; Kimijima, K. I.; Iwashita, N. *Chem. Rev.* **2007**, *107*, 3904-3951.

[2] Wang, Y.; Chen, K. S.; Mishler, J.; Cho, S. C.; Adroher, X. C. *Appl. Energy* **2011**, *88*, 981-1007.

[3] Yasuda, K.; Taniguchi, A.; Akita, T.; Ioroi, T.; Siroma, Z. *Phys. Chem. Chem. Phys.* **2006**, *8*, 746-752.

[4] Eroglu, M.; Dursun, E.; Sevencan, S.; Song, J.; Yazici, S.; Kilic, O. *Int. J. Hydrogen Energy* **2011**, *36*, 7985-7992.

[5] Steele, B. C. H.; Heinzel, A. *Nature* **2001**, *414*, 345-352.

[6] Kordesch, K.; Simader, G. *Fuel Cells and Their Applications*; Wiley-VCH: New York, 1996.

[7] Appleby, A. J.; Foulkes, F. R. *Fuel Cell Handbook*; Van Nostrand Reinhold: New York, 1989.

[8] O'Hayre, R. P.; Cha, S. W.; Colella, W.; Prinz, F. B. *Fuel Cell Fundamentals*; 2nd ed.; John Wiley & Sons: New York, 2006.

[9] Hammer, B.; Nørskov, J. K. *Adv. Catal.* **2000**, *45*, 71-129.

[10] Xin, H.; Holewinski, A.; Schweitzer, N.; Nikolla, E.; Linic, S. *Top. Catal.* **2012**, *55*, 376-390.

[11] Xin, H.; Holewinski, A.; Linic, S. *ACS Catal.* **2011**, *2*, 12-16.

[12] Holewinski, A.; Linic, S. *J. Electrochem. Soc.* **2012**, *159*, H864-H870.

[13] Wei, G. F.; Fang, Y. H.; Liu, Z. P. *J. Phys. Chem. C* **2012**, *116*, 12696-12705.

[14] Fang, Y. H.; Liu, Z. P. *J. Phys. Chem. C* **2011**, *115*, 17508-17515.

[15] Wei, G. F.; Liu, Z. P. *Phys. Chem. Chem. Phys.* **2013**, *15*, 18555-18561.

[16] Jacob, T.; Goddard, W. A. *ChemPhysChem* **2006**, *7*, 992-1005.

[17] Keith, J. A.; Jerkiewicz, G.; Jacob, T. *ChemPhysChem* **2010**, *11*, 2779-2794.

[18] Wang, B. *J. Power Sources* **2005**, *152*, 1-15.

[19] Bashyam, R.; Zelenay, P. *Nature* **2006**, *443*, 63-66.

[20] Othman, R.; Dicks, A. L.; Zhu, Z. *Int. J. Hydrogen Energy* **2012**, *37*, 357-372.

[21] Debe, M. K. *Nature* **2012**, *486*, 43-51.

[22] Hwang, S. J.; Kim, S. K.; Lee, J. G.; Lee, S. C.; Jang, J. H.; Kim, P.; Lim, T. H.; Sung, Y. E.; Yoo, S. J. *J. Am. Chem. Soc.* **2012**, *134*, 19508-19511.

[23] Stamenkovic, V.; Mun, B. S.; Mayrhofer, K. J. J.; Ross, P. N.; Markovic, N. M.; Rossmeisl, J.; Greeley, J.; Nørskov, J. K. *Angew. Chem.* **2006**, *118*, 2963-2967.

[24] Stamenkovic, V. R.; Mun, B. S.; Arenz, M.; Mayrhofer, K. J.; Lucas, C. A.; Wang, G.; Ross, P. N.; Markovic, N. M. *Nat. Mater.* **2007**, *6*, 241-247.

[25] Stamenkovic, V. R.; Fowler, B.; Mun, B. S.; Wang, G.; Ross, P. N.; Lucas, C. A.; Markovic, N. M. *Science* **2007**, *315*, 493-497.

[26] Greeley, J.; Stephens, I. E. L.; Bondarenko, A. S.; Johansson, T. P.; Hansen, H. A.; Jaramillo, T. F.; Rossmeisl, J.; Chorkendorff, I.; Nørskov, J. K. *Nat. Chem.* **2009**, *1*, 552-556.

[27] Strasser, P.; Koh, S.; Anniyev, T.; Greeley, J.; More, K.; Yu, C. F.; Liu, Z. C.; Kaya, S.; Nordlund, D.; Ogasawara, H.; Toney, M. F.; Nilsson, A. *Nat. Chem.* **2010**, *2*, 454-460.

[28] Stephens, I. E. L.; Bondarenko, A. S.; Perez-Alonso, F. J.; Calle-Vallejo, F.; Bech, L.; Johansson, T. P.; Jepsen, A. K.; Frydendal, R.; Knudsen, B. P.; Rossmeisl, J.; Chorkendorff, I. *J. Am. Chem. Soc.* **2011**, *133*, 5485-5491.

[29] Yu, T. H.; Sha, Y.; Merinov, B. V.; Goddard, W. A. *J. Phys. Chem. C* **2010**, *114*, 11527-11533.

[30] Colón-Mercado, H. R.; Popov, B. N. *J. Power Sources* **2006**, *155*, 253-263.

[31] Colón-Mercado, H. R.; Kim, H.; Popov, B. N. *Electrochem. Commun.* **2004**, *6*, 795-799.

[32] Maillard, F.; Dubau, L.; Durst, J.; Chatenet, M.; André, J.; Rossinot, E. *Electrochem. Commun.* **2010**, *12*, 1161-1164.

[33] Chen, S.; Ferreira, P. J.; Sheng, W. C.; Yabuuchi, N.; Allard, L. F.; Shao-Horn, Y. *J. Am. Chem. Soc.* **2008**, *130*, 13818-13819.

[34] Watanabe, M.; Tsurumi, K.; Mizukami, T.; Nakamura, T.; Stonehart, P. J. *Electrochem. Soc.* **1994**, *141*, 2659-2668.

[35] Antolini, E.; Salgado, J. R. C.; Gonzalez, E. R. *J. Power Sources* **2006**, *160*, 957-968.

[36] Wakabayashi, N.; Takeichi, M.; Uchida, H.; Watanabe, M. *J. Phys. Chem. B* **2005**, *109*, 5836-5841.

[37] Ma, Y. G.; Balbuena, P. B. *Surf. Sci.* **2008**, *602*, 107-113.

[38] Chen, W.; Schneider, W. F.; Wolverton, C. *J. Phys. Chem. C* **2014**, *118*, 8342-8349.

[39] Wei, G. F.; Liu, Z. P. *Energy Environ. Sci.* **2011**, *4*, 1268-1272.

[40] Mayrhofer, K. J.; Arenz, M. *Nat. Chem.* **2009**, *1*, 518-519.

[41] Dai, Y.; Ou, L.; Liang, W.; Yang, F.; Liu, Y.; Chen, S. *J Phys. Chem. C* **2011**, *115*, 2162-2168.

[42] Brushett, F. R.; Duong, H. T.; Ng, J. W.; Behrens, R. L.; Wieckowski, A.; Kenis, P. J. A. *J. Electrochem. Soc.* **2010**, *157*, B837-B845.

[43] Nishimura, T.; Morikawa, T.; Yokoi, M.; Iwakura, C.; Inoue, H. *Electrochim. Acta* **2008**, *54*, 499-505.

[44] Johansson, T. P.; Ulrikkeholm, E. T.; Hernandez-Fernandez, P.; Malacrida, P.; Hansen, H. A.; Bandarenka, A. S.; Nørskov, J. K.; Rossmeisl, J.; Stephens, I. E. L.; Chorkendorff, I. *Top. Catal.* **2014**, *57*, 245-254.

[45] Fernandes, A. C.; Paganin, V. A.; Ticianelli, E. A. *J. Electroanal. Chem.* **2010**, *648*, 156-162.

[46] Chen, S.; Gasteiger, H. A.; Hayakawa, K.; Tada, T.; Shao-Horn, Y. *J. Electrochem. Soc.* **2010**, *157*, A82-A97.

[47] Ma, Y.; Balbuena, P. B. *Surf. Sci.* **2009**, *603*, 349-353.

[48] Wu, G.; More, K. L.; Johnston, C. M.; Zelenay, P. *Science* **2011**, *332*, 443-447.

[49] Yang, H. *Angew. Chem., Int. Ed.* **2011**, *50*, 2674-2676.

[50] Nilekar, A. U.; Xu, Y.; Zhang, J.; Vukmirovic, M. B.; Sasaki, K.; Adzic, R. R.; Mavrikakis, M. *Top. Catal.* **2007**, *46*, 276-284.

[51] Adzic, R. R.; Zhang, J.; Sasaki, K.; Vukmirovic, M. B.; Shao, M.; Wang, J. X.; Nilekar, A. U.; Mavrikakis, M.; Valerio, J. A.; Uribe, F. *Top. Catal.* **2007**, *46*, 249-262.

[52] Zhou, W. P.; Yang, X. F.; Vukmirovic, M. B.; Koel, B. E.; Jiao, J.; Peng, G. W.; Mavrikakis, M.; Adzic, R. R. *J. Am. Chem. Soc.* **2009**, *131*, 12755-12762.

[53] Wang, J. X.; Inada, H.; Wu, L. J.; Zhu, Y. M.; Choi, Y. M.; Liu, P.; Zhou, W. P.; Adzic, R. R. *J. Am. Chem. Soc.* **2009**, *131*, 17298-17302.

[54] Gong, K. P.; Su, D.; Adzic, R. R. *J. Am. Chem. Soc.* **2010**, *132*, 14364-14366.

[55] Sasaki, K.; Wang, J. X.; Naohara, H.; Marinkovic, N.; More, K.; Inada, H.; Adzic, R. R. *Electrochim. Acta* **2010**, *55*, 2645-2652.

[56] Knupp, S. L.; Vukmirovic, M. B.; Haldar, P.; Herron, J. A.; Mavrikakis, M.; Adzic, R. R. *Electrocatal.* **2010**, *1*, 213-223.

[57] Sasaki, K.; Naohara, H.; Cai, Y.; Choi, Y. M.; Liu, P.; Vukmirovic, M. B.; Wang, J. X.; Adzic, R. R. *Angew. Chem., Int. Ed. Engl.* **2010**, *49*, 8602-8607.

[58] Bing, Y.; Liu, H.; Zhang, L.; Ghosh, D.; Zhang, J. *Chem. Soc. Rev.* **2010**, *39*, 2184-2202.

[59] Sha, Y.; Yu, T. H.; Merinov, B. V.; Shirvanian, P.; Goddard, W. A., III *J. Phys. Chem. C* **2012**, *116*, 21334-21342.

[60] Adzic, R. R. *Electrocatal.* **2012**, *3*, 163-169.

[61] Yang, L.; Vukmirovic, M. B.; Su, D.; Sasaki, K.; Herron, J. A.; Mavrikakis, M.; Liao, S.; Adzic, R. R. *J. Phys. Chem. C* **2013**, *117*, 1748-1753.

[62] Brimaud, S.; Engstfeld, A.; Alves, O.; Hoster, H.; Behm, R. *Top. Catal.* **2014**, *57*, 222-235.

[63] Friebel, D.; Viswanathan, V.; Miller, D. J.; Anniyev, T.; Ogasawara, H.; Larsen, A. H.; O'Grady, C. P.; Nørskov, J. K.; Nilsson, A. *J. Am. Chem. Soc.* **2012**, *134*, 9664-9671.

[64] Jackson, A.; Viswanathan, V.; Forman, A. J.; Larsen, A. H.; Nørskov, J. K.; Jaramillo, T. F. *ChemElectroChem.* **2014**, *1*, 67-71.

[65] Ley, K. L.; Liu, R. X.; Pu, C.; Fan, Q. B.; Leyarovska, N.; Segre, C.; Smotkin, E. S. *J. Electrochem. Soc.* **1997**, *144*, 1543-1548.

[66] Kua, J.; Goddard, W. A., III *J. Am. Chem. Soc.* **1999**, *121*, 10928-10941.

[67] Gurau, B.; Viswanathan, R.; Liu, R. X.; Lafrenz, T. J.; Ley, K. L.; Smotkin, E. S.; Reddington, E.; Sapienza, A.; Chan, B. C.; Mallouk, T. E.; Sarangapani, S. *J. Phys. Chem. B* **1998**, *102*, 9997-10003.

[68] Crown, A.; Moraes, I. R.; Wieckowski, A. *J. Electroanal. Chem.* **2001**, *500*, 333-343.

[69] Huang, J. J.; Yang, H.; Huang, Q. H.; Tang, Y. W.; Lu, T. H.; Akins, D. L. *J. Electrochem. Soc.* **2004**, *151*, A1810-A1815.

[70] Santos, V. P.; Del Colle, V.; Bezerra, R. M.; Tremiliosi-Filho, G. *Electrochim. Acta* **2004**, *49*, 1221-1231.

[71] Liu, W.; Huang, J. *J. Power Sources* **2009**, *189*, 1012-1015.

[72] Zhang, J. L.; Vukmirovic, M. B.; Sasaki, K.; Nilekar, A. U.; Mavrikakis, M.; Adzic, R. R. *J. Am. Chem. Soc.* **2005**, *127*, 12480-12481.

[73] Ma, Y.; Balbuena, P. B. *J. Electrochem. Soc.* **2010**, *157*, B959-B963.

[74] Ramírez-Caballero, G. E.; Ma, Y.; Callejas-Tovar, R.; Balbuena, P. B. *Phys. Chem. Chem. Phys.* **2010**, *12*, 2209-2218.

[75] Wang, J. X.; Inada, H.; Wu, L. J.; Zhu, Y. M.; Choi, Y. M.; Liu, P.; Zhou, W. P.; Adzic, R. R. J. Am. Chem. Soc. **2009**, *131*, 17298-17302.

[76] Brankovic, S. R.; Wang, J. X.; Adzic, R. R. *Surf. Sci.* **2001**, *474*, L173-L179.

[77] Herrero, E.; Buller, L. J.; Abruna, H. D. *Chem. Rev.* **2001**, *101*, 1897-1930.

[78] Zhang, J.; Mo, Y.; Vukmirovic, M. B.; Klie, R.; Sasaki, K.; Adzic, R. R. *J. Phys. Chem. B* **2004**, *108*, 10955-10964.

[79] Zhang, J.; Lima, F. H. B.; Shao, M. H.; Sasaki, K.; Wang, J. X.; Hanson, J.; Adzic, R. R. *J. Phys. Chem. B* **2005**, *109*, 22701-22704.

[80] Zhang, J.; Vukmirovic, M. B.; Xu, Y.; Mavrikakis, M.; Adzic, R. R. *Angew. Chem., Int. Ed. Engl.* **2005**, *44*, 2132-2135.

[81] Zhang, J.; Sasaki, K.; Sutter, E.; Adzic, R. R. *Science* **2007**, *315*, 220-222.

[82] Schultz, P. SeqQuest, Electronic Structure Code; Sandia National Laboratory, Albuquerque, NM, http://dft.sandia.gov/Quest/.

[83] Perdew, J. P.; Burke, K.; Ernzerhof, M. *Phys. Rev. Lett.* **1996**, *77*, 3865-3868.

[84] Perdew, J. P.; Zunger, A. *Phys. Rev. B* **1981**, *23*, 5048-5079.

[85] Ceperley, D. M.; Alder, B. J. *Phys. Rev. Lett.* **1980**, *45*, 566-569.

[86] Goddard, W. A., III *Phys. Rev.* **1968**, *174*, 659-662.

[87] Hamann, D. R. *Phys. Rev. B* **1989**, *40*, 2980-2987.

[88] Melius, C. F.; Goddard, W. A., III *Phys. Rev. A* **1974**, *10*, 1528-1540.

[89] Melius, C. F.; Olafson, B. D.; Goddard, W. A., III *Chem. Phys. Lett.* **1974**, *28*, 457-462.

[90] Redondo, A.; Goddard, W. A., III; McGill, T. C. *Phys. Rev. B* **1977**, *15*, 5038-5048.

[91] Sha, Y.; Yu, T. H.; Liu, Y.; Merinov, B. V.; Goddard, W. A., III *J. Phys. Chem. Lett.* **2010**, *1*, 856-861.

[92] Baker, N. A.; Sept, D.; Joseph, S.; Holst, M. J.; McCammon, J. A. *Proc. Natl. Acad. Sci. U.S.A.* **2001**, *98*, 10037-10041.

[93] Holst, M.; Saied, F. *J. Comput. Chem.* **1993**, *14*, 105-113.

[94] Holst, M. J.; Saied, F. *J. Comput. Chem.* **1995**, *16*, 337-364.

[95] Mills, G.; Jonsson, H.; Schenter, G. K. *Surf. Sci.* **1995**, *324*, 305-337.

[96] Mills, G.; Jonsson, H. *Phys. Rev. Lett.* **1994**, *72*, 1124-1127.

[97] Bonnet, N.; Otani, M.; Sugino, O. *J. Phys. Chem. C* **2014**, *118*, 13638-13643.

[98] Jinnouchi, R.; Kodama, K.; Hatanaka, T.; Morimoto, Y. *Phys. Chem. Chem. Phys.* **2011**, *13*, 21070-21083.

[99] Keith, J. A.; Anton, J.; Kaghazchi, P.; Jacob T. Modeling Catalytic Reactions on Surfaces with Density Functional Theory In Deutschmann, O. *Modeling and Simulation of Heterogeneous Catalytic Reactions: From the Molecular Process to the Technical System*; John Wiley & Sons, 2013.

[100] K. Kinoshita, P. Stonehart, in: J.O.M. Bockris, B.E. Conway (Eds.), *Modern Aspects of Electrochemistry*, Springer US, 1977.

[101] F. Gloaguen, J.M. Le´Ger, C. Lamy, *J. Appl. Electrochem.* **1997**, *27*, 1052-1060.

[102] Abrams, B. L.; Vesborg, P. C. K.; Bonde, J. L.; Jaramillo, T. F.; Chorkendorff, I. *J. Electrochem. Soc.* **2009**, *156*, B273-B282.

[103] Voronova, L. I.; Polyakova, V. P.; Savitskii, E. M. *Russ. Metall.* **1984**, *5*, 201-203.

[104] Raub, E.; Plate, W. *Zeit Metallkunde* **1956**, *47*, 688-693.

[105] Moore, J. T.; Chu, D.; Jiang, R. Z.; Deluga, G. A.; Lukehart, C. M. *Chem. Mater.* **2003**, *15*, 1119-1124.

[106] Hu, S.; Xiong, L. P.; Ren, X. B.; Wang, C. B.; Luo, Y. M. *Int. J. Hydrogen Energy* **2009**, *34*, 8723-8732.

[107] Yu, T. H.; Hofmann, T.; Sha, Y.; Merinov, B. V.; Myers, D. J.; Heske, C.; Goddard, W. A., III *J. Phys. Chem. C* **2013**, *117*, 26598-26607.

[108] Sha, Y.; Yu, T. H.; Merinov, B. V.; Shirvanian, P.; Goddard, W. A., III *J. Phys. Chem. Lett.* **2011**, *2*, 572-576.

[109] Kitchin, J. R.; Nørskov, J. K.; Barteau, M. A.; Chen, J. G. *Phys. Rev. Lett.* **2004**, *93*, 156801.

[110] Kitchin, J. R.; Nørskov, J. K.; Barteau, M. A.; Chen, J. G. *J. Chem. Phys.* **2004**, *120*, 10240-10246.

[111] Paulus, U. A.; Schmidt, T. J.; Gasteiger, H. A.; Behm, R. J. *J. Electroanal. Chem.* **2001**, 495, 134-145.

[112] Bard, A. J.; Faulkner, L. R. *Electrochemical Methods: Fundamentals and Applications*, John Wiley & Sons, 2001.

[113] Chen S.; Sheng, W.; Yabuuchi, N.; Ferreira, P. J.; Allard, L. F.; Shao-Horn, Y. *J. Phys. Chem. C* **2009**, 113, 1109–1125.

[114] Markovic, N. M.; Gasteiger, H. A.; Ross, P. N. *J. Phys. Chem. C* **1995**, 99, 3411–3415.

[115] Wang, J. X.; Ma, C.; Choi, Y. M.; Su, D.; Zhu, Y. ; Liu, P.; Si, R.; Vukmirovic, M. B.; Zhang, Y.; Adzic, R. R. *J. Am. Chem. Soc.* **2011**, 133, 13551-13557.

[116] Hsieh, Y. C.; Zhang, Y.; Su, D.; Volkov, V.; Si, R.; Wu, L. J.; Zhu, Y. M.; An, W.; Liu, P.; He, P.; Ye, S. Y.; Adzic, R. R.; Wang, J. X. *Nat. Commun.* **2013**, *4*, 2466.

[117] Tripković, V.; Skúlason, E.; Siahrostami, S.; Nørskov, J. K.; Rossmeisl, J. *Electrochim. Acta* **2010**, *55*, 7975-7981.

[118] Anderson, A. B.; Sidik, R. A.; Narayanasamy, J.; Shiller, P. *J. Phys. Chem. B* **2003**, *107*, 4618-4623.

[119] Hirota, K.; Song, M. B.; Ito, M. *Chem. Phys. Lett.* **1996**, *250*, 335-341.

[120] Nørskov, J. K.; Rossmeisl, J.; Logadottir, A.; Lindqvist, L.; Kitchin, J. R.; Bligaard, T.; Jonsson, H. *J. Phys. Chem. B* **2004**, *108*, 17886-17892

[121] Karlberg, G.; Rossmeisl, J.; Nørskov, J. K. *Phys. Chem. Chem. Phys.* **2007**, *9*, 5158-5161.

[122] Viswanathan, V.; Hansen, H. A.; Rossmeisl, J.; Nørskov, J. K. *ACS Catal.* **2012**, *2*, 1654-1660.

[123] Mavrikakis, M.; Hammer, B.; Nørskov, J. K. *Phys. Rev. Lett.* **1998**, *81*, 2819-2822.

[124] Schlapka, A.; Lischka, M.; Groß, A.; Käsberger, U.; Jakob, P. *Phys. Rev. Lett.* **2003**, *91*, 016101.

[125] Garcia-Gutierrez, D.; Gutierrez-Wing, C.; Miki-Yoshida, M.; Jose-Yacaman, M. *Appl. Phys. A-Mater.* **2004**, *79*, 481-487.

[126] Liu, C. P.; Twesten, R. D.; Gibson, J. M. *Ultramicroscopy* **2001**, *87*, 79-88.

[127] van der Vliet, D. F.; Wang, C.; Li, D.; Paulikas, A. P.; Greeley, J.; Rankin, R. B.; Strmcnik, D.; Tripkovic, D.; Markovic, N. M.; Stamenkovic, V. R. *Angew. Chem., Int. Ed.* **2012**, *51*, 3139-3142.

[128] Vukmirovic, M. B.; Bliznakov, S. T.; Sasaki, K.; Wang, J. X.; Adzic, R. R. *ECS Interface* **2011**, *20*, 33-40.

[129] Price, S. W.; Rhodes, J. M.; Calvillo, L.; Russell, A. E. *J. Phys. Chem. C* **2013**, *117*, 24858-24865.

[130] Price, S. W.; Speed, J. D.; Kannan, P.; Russell, A. E. *J. Am. Chem. Soc.* **2011**, *133*, 19448-19458.

[131] Gokcen, D.; Bae, S. E.; Brankovic, S. R. *J. Electrochem. Soc.* **2010**, *157*, D582-587.

[132] Lee, H. P.; Nobe, K. *J. Electrochem. Soc.* **1986**, *133*, 2035-2043.

[133] Paulus, U. A.; Wokaun, A.; Scherer, G. G.; Schmidt, T. J.; Stamenkovic, V.; Radmilovic, V.; Markovic, N. M.; Ross, P. N. *J. Phys. Chem. B* **2002**, *106*, 4181-4191.

[134] Rossmeisl, J.; Nørskov, J. K.; Taylor, C. D.; Janik, M. J.; Neurock, M. *J. Phys. Chem. B* **2006**, *110*, 21833-21839.

[135] Rossmeisl, J.; Karlberg, G. S.; Jaramillo, T.; Nørskov, J. K. *Faraday Discuss.* **2009**, *140*, 337-346.

Section Ⅱ

First-principles Modeling of Ni_4M (M= Co, Fe, Mn, Mo) Alloys as Solid Oxide Fuel Cell Anode Catalyst

Chapter 6

Introduction

The solid oxide fuel cells (SOFCs) are considered as a potential technology for power generation systems due to a number of advantages which this technology can offer.[1-3] For example, it generates electricity from oxidation of fuels via electrochemical reactions instead of mechanical conversion, provides lower noise[1] and higher efficiency which is not limited by the Carnot cycle.[1,3-5] Furthermore, since the SOFCs operate at high temperatures (typically above 800^{o}C), close to the temperature of the steam reforming process, the SOFC systems can use the waste heat for internal steam reforming.[3,6,7] In addition, SOFCs have wide fuel adaptability,[1,7] i.e. they may operate with various fuels, such as hydrogen,[2,4,8-10] carbon monoxide,[11] ammonia,[12] hydrocarbons,[3,5,8,13,14] and their combinations.[11,13,15]

In this type of fuel cells, oxygen-ion-conducting yttria-stabilized zirconia (YSZ) ceramics are widely used as electrolyte with perovskite-type oxides cathode and Ni/YSZ cermets anode.[3,16,17] SOFCs operate at ~800^{o}C because the YSZ electrolyte reaches the desirable conductivity only at this high temperature. Such an operating condition creates certain advantages and disadvantages. One of the most important advantages is that SOFCs use non-precious metal catalysts which make them more economically competitive than, for example, proton exchange membrane fuel cells (PEMFCs). Another significant advantage of SOFCs is their potential fuel flexibility, as we mentioned before. However, the high operating temperature causes certain problems, such as the long start-up time,[4] crack formation resulting from the stress because of different thermal expansion coefficients of cell components,[10,18-20] inter-diffusion at the electrolyte/electrode interfaces,[10,19-21] and the anode particle coarsening.[20] In the past years, many efforts were focused on reducing the operating temperature to develop intermediate or low-temperature SOFCs by using other high conductivity electrolytes, such

as samarium or gadolinium-doped ceria (SDC, GDC),[7,10,18,19,21] lanthanum gallate ($LaGaO_3$) based materials,[4,17,18,20] and scandium stabilized zirconia (ScSZ).[22,23]

Although SOFCs could perform internal steam reforming, utilizing hydrocarbon as fuels causes carbon deposition,[3,6,8,13,14,24] sulfur poisoning,[24-27] etc. on the conventional Ni-anode catalyst surfaces. The carbon growth mechanism includes the decomposition of hydrocarbons on Ni surface, dissolution of carbon into the bulk metals, and precipitation as carbon filament.[6,13,16] While moderate carbon may help the electronic connection between separate Ni particles,[28] it is generally believed that further growth of carbon filaments lifts the metal particles[3,29] and causes the fracture of materials resulting from the stress induced by carbon filaments.[3,6,8,16] For sulfur poisoning, either the elementary sulfur deposition or nickel sulfide formation resulting from the interaction between hydrogen sulfide (H_2S) in the hydrocarbon fuels and Ni induced the degradation of the anode performance.[24-27]

To mitigate the carbon deposition without sacrificing the anode activity, certain Ni alloys were used to replace pure Ni. For instances, Kim et al. reported that the carbon deposition could be greatly suppressed by using Ni-Cu cermet anode.[28] Fu et al. examined the microstructure, performance, and stability of $Ni_{0.75}Fe_{0.25}$-GDC anode for intermediate-temperature SOFC.[21] da Paz Fiuza et al. evaluated the conversion rate of ethanol steam reforming for various Ni-Fe alloy anode compositions and concluded that the catalyst performance was not significantly changed with the Fe substitution for Ni, but the carbon deposition could greatly be suppressed if most Ni were replaced by Fe.[7] The coking suppression was also observed for the Fe-Ni/ScSZ system by Huang et al.[22] However, the results published by Zhu et al. indicate that catalyst performance of a methane-fueled SOFC strongly depends on the Fe composition below 750°C and Ni_4Fe-ZrO_2 show the catalytic ability similar to Ni with somewhat lower carbon deposition.[30] The observed activity dependence does not look surprising because the earlier study performed by Horita et al.[31] for the methane steam oxidation and reforming

on Ni/YSZ and Fe/YSZ anodes revealed that the steam reforming activity on Ni/YSZ was much higher than that on Fe/YSZ. The work completed by Kan et al.[19] reported as well that the addition of Fe improved the stability of the Ni-Fe/GDC anode stability. In addition, the investigation of Ni-Fe + SDC composite anode for a hydrogen-fueled SOFC by Lu et al.[20] also pointed out the improved electrochemical properties of the Ni_4Fe composite anode.

Along with the experimental studies, computational modeling [mostly density-functional theory (DFT) studies] of chemical reactions in SOFCs was performed as well. For example, Rossmeisl and Bessler calculated the hydrogen atom, oxygen atom, and hydroxyl radical binding energies on surfaces of various metals and computed the reaction energy changes for three fundamental steps of the SOFC operation.[32] They found that that the activity of the metal catalysts versus O/OH binding energy obeys a volcano shape dependence with the apex at the optimum O binding energy, which is a compromise between the O adsorption and OH formation reactions. An et al.[33] carried out a similar DFT study of the binding energies of O, S, C, and H on various bimetallic Ni alloys surfaces and concluded that Cu-Ni, Fe-Ni, and Co-Ni have a better activity for the anode oxidation reaction. In addition, Mo-Ni has better C and S deposition resistance and still keep a good catalytic activity at the same time.[33] Nikolla et al.[34] employed DFT calculations to examine the activation energy barriers for C and O atom diffusion pathways, subsequent C atom attachment to a graphite sheet, and the C-O bond formation on both Ni(111) and Sn/Ni(111) surfaces. They predicted that the growth of carbon deposition is more difficult on the Sn/Ni(111) surface than on the Ni(111) surface and validated this prediction by experimental evidences. Ammal et al.[35] combined DFT and microkinetics modeling to study the hydrogen oxidation reaction at the Ni/YSZ interface and concluded that the rate-determining step is the bulk oxygen diffusion in YSZ at low temperatures and H transfer from Ni to YSZ to form water at high temperatures.

In summary we can say that according to the results published,[7,19-21,30] certain binary metal alloys, such as Ni-Fe catalysts with 10~25% Fe atomic compositions, show improved catalytic activity and/or better coking resistance and, therefore, it would be useful to better understand the mechanisms underlying these chemical processes.

In this work, we report results of our computational modeling of Ni_4M (M = Fe, Co, Mn, and Mo) binary alloys using DFT calculations to evaluate the activity and coking resistance of these catalysts. We calculated the segregation energy for different atomic configurations of the $Ni_4Fe(111)$ structure, and used the lowest energy configuration as the slab for binding energy and methane conversion reaction barriers calculations for the above-mentioned alloys.

Chapter 7

Theoretical Methods

For our QM two-dimensional slab periodic calculations, we use the SeqQuest code[36] with the Perdew, Burke, and Ernzerhof (PBE)[37] flavor of DFT with generalized gradient approximation (GGA)[38,39] and an optimized double zeta plus polarization Gaussian-type basis set for periodic calculations. Angular-momentum-projected norm-conserving pseudopotentials[40-44] are used to substitute for the core electrons in Seqquest code package. All calculations were performed with spin optimization. Since both Ni and Fe are ferromagnetic materials, the spin of Ni_4Fe is an important factor that affects its energetic. The SeqQuest program package allows the spin to be optimized simultaneously with the geometric parameters. To be confident that the program properly describes the spins, we performed manual calculations of the spins, optimizing only the geometry for each fixed spin. The energy difference between the optimized structures with the automatically (the obtained spin is 22.3) and manually calculated (the optimal spin is 23) spins is only 0.06 eV, the comparing results are summarized in Figure 1. This result confirmed the reliability of the automatic spin optimization procedure in the SeqQuest package that was widely used in our further calculations.

To describe the surface segregation and binding energies of intermediates involved in hydrocarbon fuel conversion on the $Ni_4Fe(111)$ surface, we assumed the closest fcc packed structure and used the 2 × 2 hexagonal periodic unit cell in the a and b directions based on the bulk lattice constant of Ni_3Fe, where Ni atoms are at the face centered sites and Fe at the corner sites. The calculated Ni_3Fe lattice constant is 3.56 Å, which is slightly greater than the Ni fcc structure lattice constant 3.53 Å. For calculating energetics, we considered a five-layer slab with 4 atoms per layer, in

which the top four layers are allowed to relax, but the bottom layer was fixed with the atoms in their bulk structure positions (Figure 2). There are 16 Ni and 4 Fe, totally 20 atoms per unit cell. The stacking of atoms follows the fcc(111) stacking rule, that is the abcabc… stacking series, shown as Figure 2.

The reaction energy barriers for each ORR step were calculated using the Nudged Elastic Band (NEB) method[45,46] implemented into the SeqQuest code, and the energy difference between the initial step and the highest NEB image (transition state) was considered as an energy barrier. The initial and final states were determined from the binding energies of the ORR species.

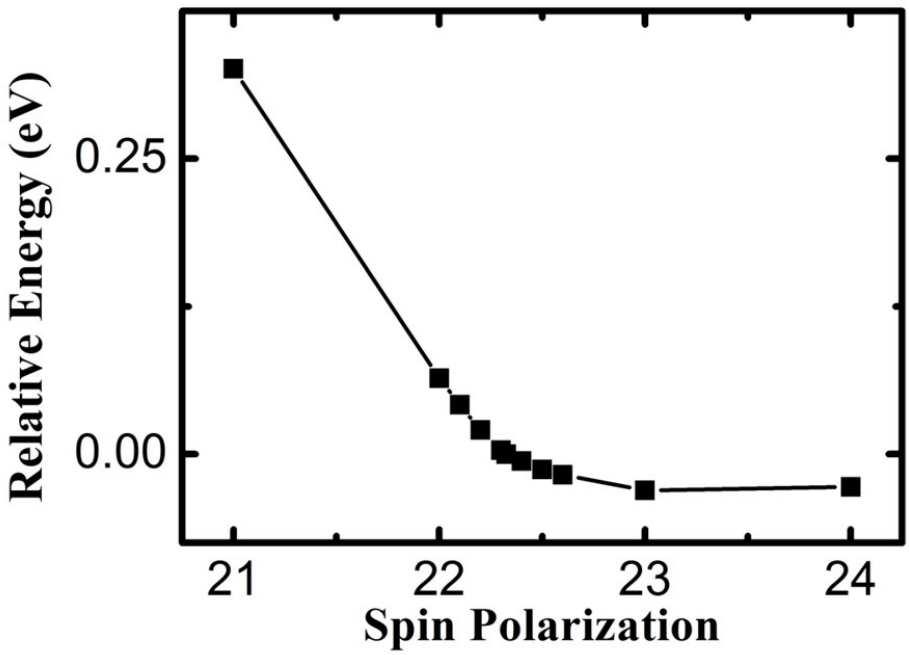

Figure 1. The energy versus spin polarization relationship of Ni_4Fe.

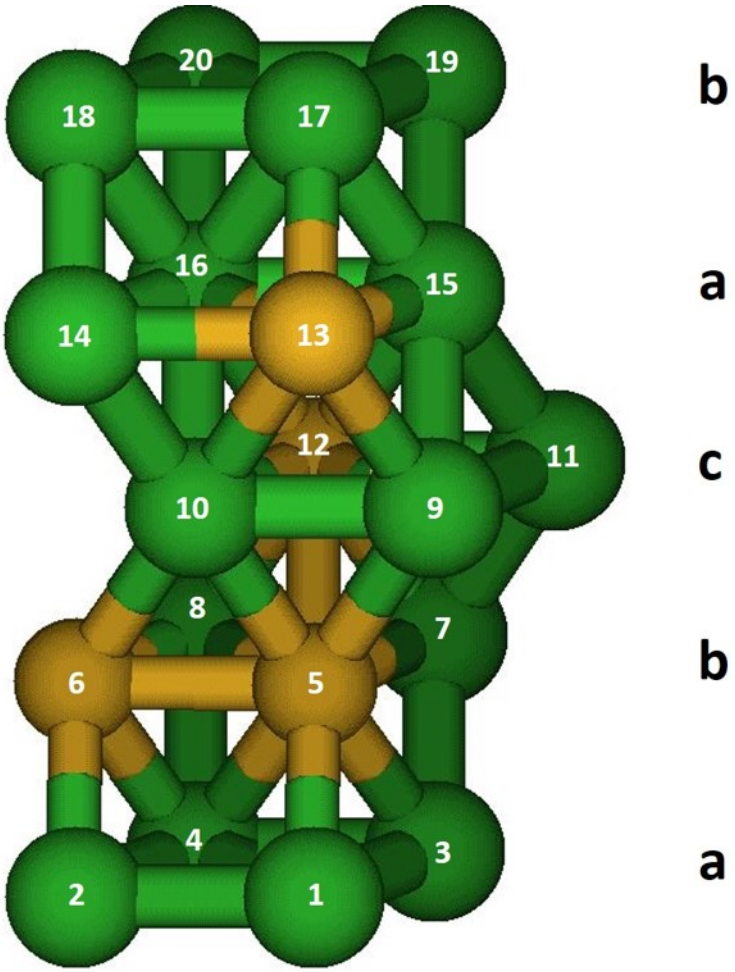

Figure 2. The atomic positions for the 5 layer slab with abcab stacking sequence.

Chapter 8

Results and Discussion

8.1 Surface Segregation in Ni_4Fe Alloy

To study the segregation effect for the Ni_4Fe alloy, we have examined different slab structures, which can be built by placing the Fe atoms in different positions. For example, the lowest energy structure is the structure which distributes the Fe atoms in 5, 6, 12, and 13 atomic positions, as shown in Figure 2. The results of our DFT calculations on the segregation effect for the Ni_4Fe alloys are listed in Table 1. Since mirror symmetry relationship exists between the structures, some structures are ignored in our calculation. For example, 5-6-12-13 and 8-10-15-16 are mirror symmetrical to each other via XY plane, so does 5-7-12-13 and 8-10-14-16. Though with symmetrical relationship, the fixed atom number 1 to 4 make the structures with two Fe atoms in the 2nd layer (atom number 5~8) have ~0.2 eV lower energy than the structure with two Fe atoms in the 4th layer (atom number 13-16). Therefore, our slab calculations ignored some mirror symmetrical configurations without losing the generality.

The calculated spin obtained for Ni_4Fe, using automatic spin optimization procedure, is ~0.6 per a Ni atom and ~3.0 per a Fe atom. To summarize, we find that Ni atoms show segregation preference for the surface layer and the most favorable Ni4Fe structure has the (02110) Fe atom distribution (5-6-12-13). The 5-6-12-13 is also the structure that separate the Fe atoms farthest with surface segregation at the top and bottom layer. This 5-6-12-13 structure was used for our further QM binding energy and reaction barriers calculations.

Table 1. Ni_4Fe surface segregation energies (eV).

Number of Fe atoms in each layer*	Position of Fe atoms	Relative energy (eV)**
40000	1-2-3-4	2.66
00400	9-10-11-12	1.36
20002	1-2-19-20	1.64
	2-3-17-20	1.74
02020	6-7-14-15	0.62
01111	2-7-10-15	0.57
	2-7-9-13	0.76
	2-8-10-16	0.78
11101	2-7-9-18	0.90
11011	1-8-13-20	1.24
01210	6-10-11-14	0.58
	7-9-12-14	0.57
	7-9-11-14	0.29
10201	2-9-11-19	1.17
01120	6-12-13-14	0.19
	8-10-14-16	0.52
	8-10-15-16	0.20
02110	5-7-12-13	0.28
	5-6-12-13	0.00

*The number from left to right indicates the number of Fe atoms from the bottom layer (1st layer) to the top layer (5th layer)

**All energies are relative to 5-6-12-13 configuration (-65780.53 eV)

8.2 Binding Energy of CH_x Species

8.2.1 *Binding Site Notation*

Generally, a closest packed (111) surface of fcc structured metals has four types of sites:

1. On-top, bonded to one Ni (μ_1), denoted as t,
2. Bridging, between two Ni (μ_2), denoted as b,
3. Bridging, between three Ni (μ_3-fcc) but in the fcc position (not above atoms of the top or 4th layer), denoted as f.
4. Bridging, between three Ni (μ_3-hcp) but in the hcp position (above atoms of the 4th layer), denoted as h.

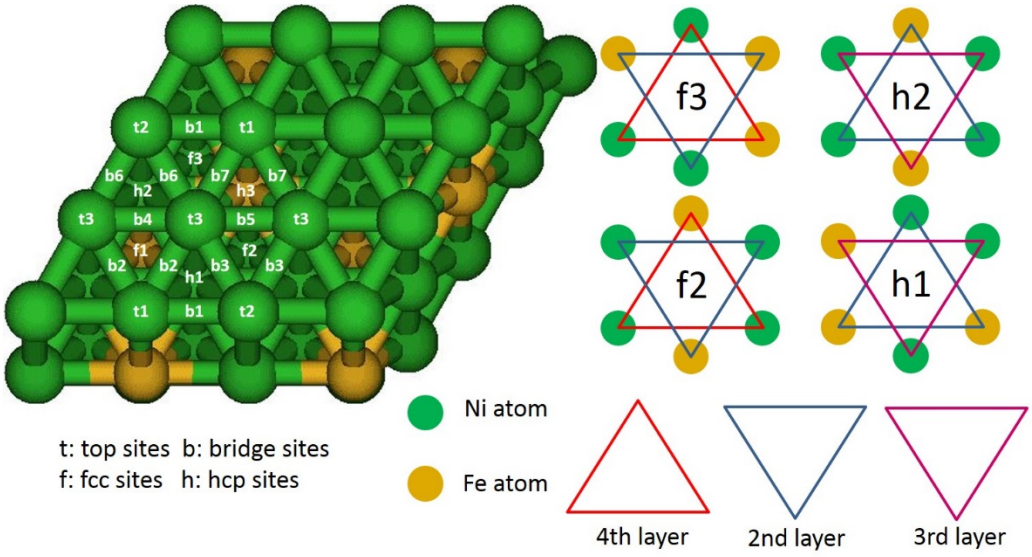

Figure 3. Notations of binding sites (left) and schematic representation possible binding sites (right) for the Ni_4Fe alloy.

However for the Ni_4Fe surface, we need to take into account that the 3rd and 4th layer is 25% Fe and 75% Ni, while the 2nd layer 50% Fe and 50 % Ni. We find that the binding energies to the top pure Ni layer depend strongly on the nature of the 2nd, 3rd, and 4th layer Fe atoms (see Figure 3 for details).

Considering only the 4th and 5th layers, we have three types of top sites: t_1 and t_3 with two Ni and one Fe neighbor in the 4th layer, while t_2 with three Ni neighbor atoms. As it can be seen from Figure 2, t_1 and t_3 sites are different because the Fe atoms in the 2nd layer are located vertically below t_1 and t_2 sites, on the other hand, the atoms directly below t_3 site at 2nd layer are Ni atoms.

Considering only top two layers, there are seven bridge sites, depending on the number of Fe atoms underneath: b_1, b_2, b_3, b_4, b_6 and b_5, b_7 with 0 and 1 Fe atoms in the 4th layer, respectively. If we take into account the 3rd layer as well, then two subtypes for b_2, b_4 and b_1, b_3, b_6 depending on the number of Fe atoms underneath in the 3rd layer, can be distinguished. If we also consider the 2nd layer, the underneath of the b_2 site connects one Ni and one Fe atoms, while the underneath of b_4 site connects two Ni atoms in the 2nd layer. Similarly, the underneath of b_1 connects two Fe atoms, while the underneath of b_3 and b_6 has one Fe and one Ni atom but in different positions. The underneath of b_5 has two Ni atoms, whereas the underneath of b_7 has one Fe and one Ni atom in the 2nd layer.

Considering the top two layers, three fcc sites can be distinguished: f_1 and f_2, f_3 with zero and one Fe atom in the sublayer (4th layer) triangle. If we take into account the 3rd layer as well, then f_1 is on top of the 3rd layer Fe, while f_2 and f_3 are on top of the 3rd layer Ni. With the 2nd layer, f_2 has one Fe atom in the 4th layer triangle, but f_3 has two Fe atoms.

Similarly considering the top two layers, three hcp sites, h_1, h_2 and h_3, can be distinguished. Here h_1, h_2 are on top of the sublayer Ni, while h_3 is on top of the sublayer Fe. Adding the 2nd layer allows

the h_1 and h_2 sites to be distinguished. h_1 has two Fe atoms in the 2nd layer, while h_2 has only one Fe atom in the projected triangle of the 2nd layer atoms (Figure 3).

8.2.2 *Binding Energies of Methane Reforming Intermediates*

First, we studied the methane reforming intermediates, CH_3, CH_2, CH, C, and H binding on various sites shown in Figure 3. Tables 2-6 list binding energies for CH_3, CH_2, CH, C and H species and their comparison with similar binding energies for pure Ni(111).[47] For CH_3 binding (see Table 3), the most and 2nd stable site is f_2 and h_i site with 41.4 and 40.5 Kcal/mol binding energy, respectively. CH_3 binding energies on other fcc and hcp sites are between 37 to 40 Kcal/mol, which are greater than the top site or bridge site binding energies (~35 to 37 Kcal.mol). Therefore, the fcc and hcp sites are energetically more preferable than top and bride sites, very similar to the pure Ni case. However, the addition of Fe atoms make the binding energy of Ni_4Fe slightly lower than binding energy of Ni, which possibly due to the ligand effect of Fe atoms or the strain effect resulting from lattice constant change. Since similar discussion for ligand effect and strain effect for Pt alloys has been discussed in our previous studies,[48,49] and we concluded that the ligand effect is more significant than strain effect in modifying the binding energy/activity.

For CH_2, the most stable binding sites are f_3 and h_1 site, while the fcc/hcp site with Fe atom directly underneath (h_3/f_1) is the least preferable fcc/hcp site. The top and bridge sites are relatively difficult for CH_2 binding, CH_2 is even unstable to bind at some of these sites and migrate to the neighboring fcc/hcp sites (see Table 3).

The most stable CH binding site is pretty similar to CH_2 binding. But CH binding at the most stable site, h_1, is 0.3 Kcal/mole greater than f_3, consistent with pure Ni case, in which hcp site is also slightly more stable than the fcc site. The CH binding energies are ~10 Kcal/mol smaller than binding

on pure Ni surface, while the differences for CH_3 and CH_2 binding between Ni_4Fe and Ni surfaces are only 2~4 Kcal/mol.

For C binding on Ni_4Fe surface, binding at top sites and bridge sites are unfavorable and C will migrate to surrounding fcc/hcp sites after geometry optimization. h_1 and h_2 sites are the most two preferred binding sites, consistent with our previous Ni result in which hcp site is the most favorable C binding site. But again, C binding on Ni_4Fe surface is ~10 Kcal/mol lower than on the pure Ni surface. The lower C binding energy indicates that C removal is easier and the coke formation is less, which conform to previous experimental literature.[7,19,30] For H binding, the most preferable binding sites are f_2 and h_1, with 60.4 and 60.2 Kcal/mol binding energy, respectively. The only bridge site that H adsorbed is b_3 site, which located between f_2 and h_1 site. Top sites are more disliked for H adsorption, and H binding energy at t_2 site is greater than t_3 site. If we combine H binding results of bridge and top sites, we could find that the sites which neighbors to Fe atoms is not ideal for H adsorption. For H binding on pure Ni, the fcc site is also slightly favorable than hcp site, and both fcc and hcp sites are more stable than bridge and top sites. This result is consistent with our Ni_4Fe results.

Based on the results obtained, we can assume that the most stable sites for all species are either fcc or hcp for both Ni_4Fe and pure Ni. The species at the top and bridge sites are bound more weakly to the Ni_4Fe surface than at the fcc and hcp sites.

Summarizing the data for the binding energy of the species involved in the methane conversion reaction, we find that the Ni_4Fe surface bind CH_3, CH_2, and H by 1~5 kcal/mol more weakly than pure Ni, whereas the binding energy of CH and C is ~10 kcal/mol weaker for Ni_4Fe compared to pure Ni. The weaker binding energy of C means easier removal of carbon deposits from the surface, providing better coking resistance. However, to make a reliable conclusion about the catalytic activity

of the Ni-based binary alloys compared to that of pure Ni, we need information about the reaction energy barriers for the methane conversion on the metal alloy surfaces.

Table 2. CH_3 binding energies.

	Ni_4Fe					**Ni**				
	Sites	E_{bond} (Kcal/mol)	Opt. spin	Ni ave. spin	Fe ave. spin	sites	E_{bond} (Kcal/mol)	Calc. spin	Opt. spin	Ni ave. spin
CH_3	t_1	35.2	22.25	0.63	3.07	T	37.2	12	11.80	0.78
	t_2	36.2	22.35	0.63	3.09					
	t_3	35.6	22.25	0.63	3.07					
	b_1	37.7	22.31	0.63	3.09	B	39.3	12	11.69	0.78
	b_2	unstable[a]								
	b_3	36.0	22.36	0.63	3.08					
	b_4	34.5	22.34	0.63	3.06					
	b_5	35.9	22.26	0.63	3.07					
	b_6	37.3	22.31	0.63	3.08					
	b_7	34.5	22.26	0.63	3.08					
	f_1	37.3	22.29	0.63	3.06	F	42.7	12	11.54	0.79
	f_2	**41.4**	**22.25**	**0.62**	**3.08**					
	f_3	40.4	22.24	0.62	3.09					
	h_1	**40.5**	**22.32**	**0.63**	**3.08**	H	42.3	12	11.60	0.80
	h_2	40.0	22.34	0.63	3.08					
	h_3	37.9	22.17	0.62	3.07					

[a] CH_3 moves to the h_1 site after geometry optimization.

Table 3. CH_2 binding energies.

	Ni_4Fe					**Ni**				
	Sites	E_{bond} (Kcal/mol)	Opt. spin	Ni ave. spin	Fe ave. spin	sites	E_{bond} (Kcal/mol)	Calc. spin	Opt. spin	Ni ave. spin
CH_2	t_1	62.6	22.62	0.64	3.07	T	66.0	12	11.62	0.77
	t_2	64.5	22.72	0.64	3.08					
	t_3	unstable[a]								
	b_1	unstable[b]				B	83.9	12	11.04	0.76
	b_2	unstable[c]								
	b_3	82.8	21.90	0.60	3.08					
	b_4	unstable[d]								
	b_5	unstable[a]								
	b_6	82.5	21.91	0.60	3.08					
	b_7	79.5	21.90	0.60	3.07					
	f_1	78.3	22.09	0.61	3.09	F	89.3	11	10.88	0.71
	f_2	84.1	22.00	0.61	3.08					
	f_3	**85.7**	**21.99**	**0.60**	**3.09**					
	h_1	**84.3**	**21.91**	**0.60**	**3.08**	H	88.6	11	10.77	0.71
	h_2	81.2	21.94	0.60	3.08					
	h_3	79.1	21.88	0.60	3.09					

[a] CH_2 moves to f_2 site after geometry optimization.

[b] CH_2 moves to f_3 site after geometry optimization.

[c] CH_2 moves to h_1 site after geometry optimization.

[d] CH_2 moves to h_2 site after geometry optimization.

Table 4. CH binding energies.

	Ni_4Fe					**Ni**				
	Sites	E_{bond} (Kcal/mol)	Opt. spin	Ni ave. spin	Fe ave. spin	sites	E_{bond} (Kcal/mol)	Calc. spin	Opt. spin	Ni ave. spin
CH	t_1	unstable[a]				T	99.5	11	10.92	0.72
	t_2	unstable[b]								
	t_3	unstable[c]								
	b_1	unstable[c]				B	139.4	10	10.42	0.65
	b_2	unstable[c]								
	b_3	unstable[c]								
	b_4	unstable[d]								
	b_5	unstable[e]								
	b_6	unstable[d]								
	b_7	unstable[a]								
	f_1	129.9	21.79	0.58	3.11	F	148.0	10	10.24	0.63
	f_2	138.9	21.34	0.57	3.09					
	f_3	**139.0**	**21.43**	**0.57**	**3.09**					
	h_1	**139.3**	**21.22**	**0.56**	**3.09**	H	148.9	10	10.06	0.65
	h_2	138.8	21.25	0.56	3.08					
	h_3	133.6	21.16	0.55	3.10					

[a]CH moves to the h_3 site after geometry optimization.

[b]CH moves to the f_3 site after geometry optimization.

[c]CH moves to the h_1 site after geometry optimization.

[d]CH moves to the h_2 site after geometry optimization.

[e]CH moves to the f_2 site after geometry optimization.

Table 5. C binding energies.

	Ni_4Fe					Ni				
	Sites	E_{bond} (Kcal/mol)	Opt. spin	Ni ave. spin	Fe ave. spin	sites	E_{bond} (Kcal/mol)	Calc. spin	Opt. spin	Ni ave. spin
C	t_1	unstable[a]				T	103.6	11	10.96	0.71
	t_2	unstable[b]								
	t_3	unstable[a]								
	b_1	unstable[c]				B	143.1	10	10.04	0.64
	b_2	unstable[c]								
	b_3	unstable[c]								
	b_4	unstable[d]								
	b_5	unstable[e]								
	b_6	unstable[d]								
	b_7	unstable[b]								
	f_1	137.0	20.59	0.52	3.08	F	153.2	10	9.87	0.64
	f_2	141.7	20.50	0.51	3.08					
	f_3	141.5	20.51	0.51	3.08					
	h_1	**142.9**	**20.35**	**0.51**	**3.06**	H	154.8	10	9.82	0.63
	h_2	**141.8**	**20.32**	**0.51**	**3.06**					
	h_3	140.0	20.34	0.50	3.10					

[a] C moves to the h_3 site after geometry optimization.

[b] C moves to the f_3 site after geometry optimization.

[c] C moves to the h_1 site after geometry optimization.

[d] C moves to the h_2 site after geometry optimization.

[e] C moves to the f_2 site after geometry optimization.

Table 6. H binding energies.

	Ni_4Fe					**Ni**				
	Sites	E_{bond} (Kcal/mol)	Opt. spin	Ni ave. spin	Fe ave. spin	sites	E_{bond} (Kcal/mol)	Calc. spin	Opt. spin	Ni ave. spin
H	t_1	unstable[a]				T	52.7	12	11.93	0.79
	t_2	53.9	22.52	0.64	3.09					
	t_{3-2}	51.9	22.42	0.64	3.06					
	b_1	unstable[b]				B	62.6	12	11.79	0.79
	b_2	unstable[c]								
	b_3	58.0	22.30	0.63	3.08					
	b_4	unstable[d]								
	b_5	unstable[e]								
	b_6	unstable[b]								
	b_7	unstable[b]								
	f_1	58.1	22.40	0.64	3.07	F	65.7	12	11.77	0.79
	f_2	**60.4**	**22.33**	**0.63**	**3.08**					
	f_3	59.2	22.24	0.63	3.07					
	h_1	**60.2**	**22.35**	**0.63**	**3.08**	H	65.4	12	11.78	0.79
	h_2	59.6	22.35	0.63	3.08					
	h_3	58.1	22.27	0.63	3.08					

[a] C moves to the h_3 site after geometry optimization.

[b] C moves to the f_3 site after geometry optimization.

[c] C moves to the h_1 site after geometry optimization.

[d] C moves to the h_2 site after geometry optimization.

[e] C moves to the f_2 site after geometry optimization.

8.3 Reaction Energy Barriers for Methane Conversion

8.3.1 *Ni_4Fe Catalyst*

Generally, efficiency of a catalyst much depends on reaction energy barriers. Having the binding energies calculated for the intermediates at various sites, we can now estimate barriers for the steps of the methane reforming reaction to describe the overall reaction mechanism.

Since the experimental barrier for CH_4 dehydrogenation is 17.7 Kcal/mol,[47] which is smaller than the subsequent reaction, we will ignore CH_4 dehydration but focusing on the subsequent reactions. We used CH_3 bound at the most preferable site, i.e. f_2 as the initial state and the decomposed CH_x which stayed at f_2 site as the initial state of the subsequent reactions because f_2 is still energy preferable site even though not the most one. The reason is because migration from f_2 site to the neighboring h_1 site will pass through the relatively high energy b_3 site, and the energy cost to overcome this barrier make this route is not preferable.

Table 7 summarize the reaction energy barriers for methane conversion on Ni_4Fe surface and make a comparison with pure Ni. The reaction barrier for $CH_{3\,(ad)} \rightarrow CH_{2\,(ad)} + H_{(ad)}$ on Ni_4Fe surface is 21.4 Kcal/mol, slightly higher than on pure Ni surface. However, for the rate- determination step (RDS), $CH_{(ad)} \rightarrow C_{(ad)} + H_{(ad)}$, the reaction energy barrier for Ni_4Fe is smaller than on pure Ni surface. Therefore, the catalytic activity of Ni_4Fe for CH_4 conversion may be greater than Ni activity, which was also reported in previous experimental result.[20] Furthermore, the lower C binding energy implies that the coking resistance on Ni_4Fe surface is better than on pure Ni, which conforms to previous experimental literature.[19,30]

Table 7. Reaction energy barriers (kcal/mol) for methane decomposition and carbon binding energy on Ni, Ni_4Fe, Ni_4Co, Ni_4Mo, and Ni_4Mn catalyst surfaces.

Reaction	Ni[47]	Ni_4Fe	Ni_4Co	Ni_4Mo	Ni_4Mn
$CH_3 \rightarrow CH_2+H$	18.4	21.2	21.4	17.9	23.8
$CH_2 \rightarrow CH+H$	8.3	9.4	10.2	8.1	10.9
$CH \rightarrow C+H$	32.8	31.4	33.7	34.9	29.9
Carbon binding energy	155	143	143	154.1	144.1

8.3.2 *Ni_4Co, Ni_4Mo, and Ni_4Mn Catalysts*

Because better activity for fuel oxidation at SOFC anode by some Ni alloys was predicted by previous theoretical literature,[33] we performed NEB calculations to evaluate the activity of Ni_4Co, Ni_4Mo, and Ni_4Mn alloys for CH_4 reforming reaction. Our segregation energy comparison of these three alloys between 5-6-12-13 (the segregated one) and 2-7-10-15 (non-segregated one) configuration showed that the segregated configuration still has lower energy than non-segregated one (see Table 8), therefore, we used the same 5-6-12-13 configuration as the slab structure for CH_4 reforming reaction. We did not perform the binding energy calculation for these three alloys because of the computational cost but assume that the CH_x species have the same most preferable binding sites as Ni_4Fe. Our simple tests for some fcc/hcp/bridge sites binding showed that the binding at fcc and hcp sites is more stable than on bridge sites and the difference between fcc and hcp site is insignificant as we observed at Ni_4Fe catalyst.

The reaction energy barriers for these three catalysts are listed in Table 7. The values of each step are similar to the values of Ni_4Fe and pure Ni catalysts. The RDS for CH_4 conversion on these

catalysts is $CH_{ad} \rightarrow C_{ad} + H_{ad}$, the same as Ni_4Fe and Ni. Only Ni_4Mn possesses both lower RDS barrier and C binding energy as Ni_4Fe. Ni_4Co has lower C binding energy but slightly higher RDS barrier than pure Ni. The results are summarized by Figure 4. Differs to the previous study,[33] our result on Ni_4Mo shows that this alloy should have a similar activity and C binding energy as pure Ni, and could not be proposed as a potential catalyst with better activity and coking resistance. This contradiction may be due to the surface segregation effect that did not taken into consideration or using only binding energy as the indicator for activity in previous literature.[35] To summarize, Ni_4Fe and Ni_4Mn have higher activity for CH_4 conversion and better coking resistance, thus could be potential catalysts for CH_4 reforming at SOFC anode.

Table 8. Ni_4X alloy surface segregation energies (eV).

Ni_4X alloys	Position of the X atoms	Relative energy (eV)*
Ni_4Fe	5-6-12-13	0.00
	2-7-10-15	0.57
Ni_4Co	5-6-12-13	0.00
	2-7-10-15	0.35
Ni_4Mn	5-6-12-13	0.00
	2-7-10-15	0.55
Ni_4Mo	5-6-12-13	0.00
	2-7-10-15	0.46

*The energy is relative to 5-6-12-13 configuration (the surface segregated structure) of each alloy.

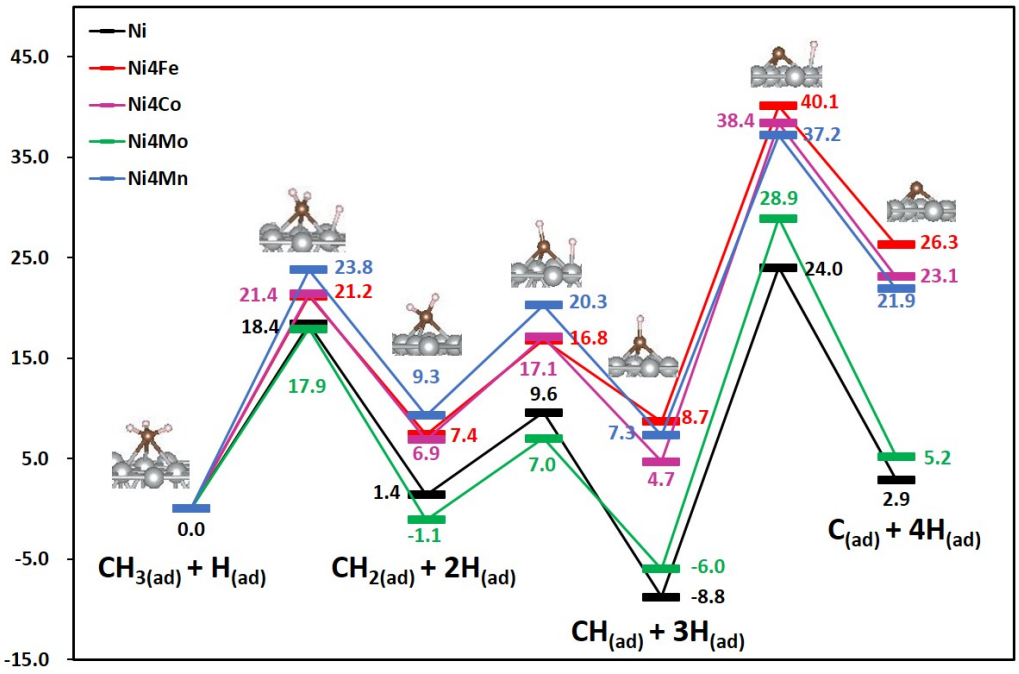

Figure 4. Energy pathway for CH_4 decomposition on Ni_4X surfaces (the insets show the decomposition occur on Ni_4Fe surface).

Chapter 9

Conclusions

SOFC is a clean energy technology with wide fuel adaptability. However, using hydrocarbon as the fuel has the coking problem and induce the poor stability. We studied the surface segregation for Ni_4Fe, and found that a Fe atom distribution of (0%, 50%, 25%, 25%, 0%) starting at the bottom layer with Ni segregation has the lowest energy. The binding energy calculations of CH_x species at various binding sites were performed and used as the initial state for CH_4 conversion reaction energy barrier calculation. The fcc and hcp sites are more preferable for binding than top and bridge sites. The binding energy results for CH_x species are pretty similar to pure Ni results but the C binding energy on Ni_4Fe is ~10 Kcal/mol less than on pure Ni surface. Our NEB calculation showed that Ni_4Fe also has lower RDS energy barrier. Further calculation for other Ni alloys and comparison with pure Ni results indicated that Ni_4Fe, Ni_4Co, and Fe_4Mn all have better coking resistance than pure Ni, but only Ni_4Fe and Ni_4Mn have slightly better activity than Ni, maybe good catalysts for CH_4 reforming at SOFC anode.

BIBLIOGRAPHY

[1] Singhal, S. *Solid State Ionics* **2000**, *135*, 305-313.

[2] Lu, X. C.; Zhu, J. H.; Bi, Z. H. *Solid State Ionics* **2009**, *180*, 265-270.

[3] McIntosh, S.; Gorte, R. J. *Chem. Rev.* **2004**, *104*, 4845-4866.

[4] Ishihara, T.; Yan, J.; Shinagawa, M.; Matsumoto, H. *Electrochim. Acta* **2006**, *52*, 1645-1650.

[5] Sheng, C. Y.; Dean, A. M. *J. Phys. Chem. A* **2004**, *108*, 3772-3783.

[6] Gorte, R. J.; Vohs, J. M. *J. Catal.* **2003**, *216*, 477-486. 305-313.

[7] da Paz Fiuza, R.; Aurélio da Silva, M.; Boaventura, J. S. *Int. J. Hydrogen Energy* **2010**, *35*, 11216-11228.

[8] Lin, Y.; Zhan, Z.; Liu, J.; Barnett, S. A. *Solid State Ionics* **2005**, *176*, 1827-1835.

[9] Ringuedé, A.; Fagg, D.; Frade, J. *J. Eur. Ceram. Soc.* **2004**, *24*, 1355-1358.

[10] Xie, Z.; Zhu, W.; Zhu, B.; Xia, C. *Electrochim. Acta* **2006**, *51*, 3052-3057. 1358.

[11] Zhu, H.; Kee, R. J.; Janardhanan, V. M.; Deutschmann, O.; Goodwin, D. G. *J. Electrochem. Soc.* **2005**, *152*, A2427-A2440.

[12] Ni, M.; Leung, M. K.; Leung, D. Y. *International Journal of Energy Research* **2009**, *33*, 943-959.

[13] Kim, T.; Liu, G.; Boaro, M.; Lee, S.-I.; Vohs, J. M.; Gorte, R. J.; Al-Madhi, O.; Dabbousi, B. *J. Power Sources* **2006**, *155*, 231-238.

[14] Huang, T.-J.; Wang, C.-H. *J. Power Sources* **2006**, *163*, 309-315.

[15] Hecht, E. S.; Gupta, G. K.; Zhu, H.; Dean, A. M.; Kee, R. J.; Maier, L.; Deutschmann, O. *Appl. Catal., A* **2005**, *295*, 40-51.

[16] Gross, M. D.; Vohs, J. M.; Gorte, R. J. *J. Mater. Chem.* **2007**, *17*, 3071-3077.

[17] Ju, Y.-W.; Eto, H.; Inagaki, T.; Ida, S.; Ishihara, T. *J. Power Sources* **2010**, *195*, 6294-6300.

[18] Tucker, M. C. *J. Power Sources* **2010**, *195*, 4570-4582.

[19] Kan, H.; Lee, H. *Catal. Commun.* **2010**, *12*, 36-39.

[20] Lu, X.; Zhu, J. *J. Power Sources* **2007**, *165*, 678-684.

[21] Fu, C.; Chan, S.; Ge, X.; Liu, Q.; Pasciak, G. *Int. J. Hydrogen Energy* **2011**, *36*, 13727-13734.

[22] Huang, B.; Wang, S.; Liu, R.; Wen, T. *J. Power Sources* **2007**, *167*, 288-294.

[23] Cowin, P. I.; Petit, C. T.; Lan, R.; Irvine, J. T.; Tao, S. *Adv. Energy Mater.* **2011**, *1*, 314-332.

[24] Gorte, R.; Vohs, J. *Curr. Opin. Colloid Interface Sci.* **2009**, *14*, 236-244.

[25] Cheng, Z.; Wang, J.-H.; Choi, Y.; Yang, L.; Lin, M.; Liu, M. *Energy Environ. Sci.* **2011**, *4*, 4380-4409.

[26] Gong, M.; Liu, X.; Trembly, J.; Johnson, C. *J. Power Sources* **2007**, *168*, 289-298.

[27] Yang, C.; Yang, Z.; Jin, C.; Xiao, G.; Chen, F.; Han, M. *Adv. Mater.* **2012**, *24*, 1439-1443.

[28] Kim, H.; Lu, C.; Worrell, W.; Vohs, J.; Gorte, R. *J. Electrochem. Soc.* **2002**, *149*, A247-A250.

[29] Baker, R. *Carbon* **1989**, *27*, 315-323.

[30] Zhu, H.; Wang, W.; Ran, R.; Su, C.; Shi, H.; Shao, Z. *Int. J. Hydrogen Energy* **2012**, *37*, 9801-9808.

[31] Horita, T.; Sakai, N.; Kawada, T.; Yokokawa, H.; Dokiya, M. *J. Electrochem. Soc.* **1996**, *143*, 1161-1168.

[32] Rossmeisl, J.; Bessler, W. G. *Solid State Ionics* **2008**, *178*, 1694-1700.

[33] An, W.; Gatewood, D.; Dunlap, B.; Turner, C. H. *J. Power Sources* **2011**, *196*, 4724-4728.

[34] Nikolla, E.; Holewinski, A.; Schwank, J.; Linic, S. *J. Am. Chem. Soc.* **2006**, *128*, 11354-11355.

[35] Ammal, S. C.; Heyden, A. *J. Phys. Chem. Lett.* **2012**, *3*, 2767-2772.

[36] Schultz, P. SeqQuest, Electronic Structure Code; Sandia National Laboratory, Albuquerque, NM, http://dft.sandia.gov/Quest/.

[37] Perdew, J. P.; Burke, K.; Ernzerhof, M. *Phys. Rev. Lett.* **1996**, *77*, 3865-3868.

[38] Perdew, J. P.; Zunger, A. *Phys. Rev. B* **1981**, *23*, 5048-5079.

[39] Ceperley, D. M.; Alder, B. J. *Phys. Rev. Lett.* **1980**, *45*, 566-569.

[40] Goddard, W. A., III *Phys. Rev.* **1968**, *174*, 659-662.

[41 Hamann, D. R. *Phys. Rev. B* **1989**, *40*, 2980-2987.

[42] Melius, C. F.; Goddard, W. A., III *Phys. Rev. A* **1974**, *10*, 1528-1540.

[43] Melius, C. F.; Olafson, B. D.; Goddard, W. A., III *Chem. Phys. Lett.* **1974**, *28*, 457-462.

[44] Redondo, A.; Goddard, W. A., III; McGill, T. C. *Phys. Rev. B* **1977**, *15*, 5038-5048.

[45] Mills, G.; Jonsson, H. *Phys. Rev. Lett.* **1994**, *72*, 1124-1127.

[46] Mills, G.; Jonsson, H.; Schenter, G. K. *Surf. Sci.* **1995**, *324*, 305-337.

[47] Mueller, J. E.; van Duin, A. C.; Goddard III, W. A. *J. Phys. Chem. C.* **2009**, *113*, 20290-20306.

[48] Tsai, H.-C.; Yu, T.; Sha, Y.; Merinov, B. V.; Wu, P.-W.; Chen, S.-Y.; Goddard III, W. A. *J. Phys. Chem. C.* **2014**.

[49] Tsai, H.-C.; Hsieh, Y.-C.; Yu, T.; Lee, Y.-J.; Wu, Y.-H.; Merinov, B. V.; Wu, P.-W.; Chen, S.-Y.; Adzic, R. R.; Goddard III, W. A. *ACS Catal.* **2015**.

Appendix

DFT Study of Doped Perovskite Ceramics as Proton Conducting Materials

Preface

The last part of my thesis includes preliminary results of work that is still in progress and certain issues still need to be clarified. Nevertheless, a summary of this study may be of interest for researchers working in the field of proton-conducting perovskite-ceramics. Since the results are preliminary, I decided to place them in the appendix rather than in the main body of the thesis.

Abstract

We used quantum mechanics calculations to study the doped perovskite oxides as proton-conducting ceramics for hydrogen permeation. A 2x2x2 $Ba_8X_7(OH)_1M_1O_{23}$ (X=Ce, Zr; M=Y, Gd, Dy) cell was used to study proton diffusion that both includes intra-octahedron and inter-octahedra proton transfers. Without any calculation restriction, we only observed intra-octahedron proton transfer with 0.26 eV barrier, which is smaller than experimental value 0.44 eV. For fixed O_{donor}-$O_{acceptor}$ distance, our calculations show that the Gd-doped BaCeO3 and Y-doped BaZrO3 oxides have slightly lower (0.03 eV) proton transfer barriers than the others, but the difference is not significant. It is well-known that the proton transfer barrier is proportional to the O_{donor}-$O_{acceptor}$ distance. During the thermal librations/vibrations, the O_{donor}-$O_{acceptor}$ distance becomes short enough and the proton may jump from one oxygen to another, i.e. the proton transfer will occur. As a matter of fact, the bulk proton conductivity of the oxides considered here are similar, therefore, a more

comprehensive study by ReaxFF reactive dynamics which includes the grain boundary conduction will be performed in the future based on our QM results.

Introduction

Integrated gasification combined cycle (IGCC) is an electricity generation technology that integrates the coal gasification and combined cycle. The gasification process transfers the coal or carbon based fuel into the syngas. Then the purification process removes the impurities and sulfur from the syngas before combustion. Therefore, IGCC system has lower emission with equal or higher efficiency than general coal combustion power plants.[1] Our strategic target is to develop a system that could capture the CO_2 for photocatalytic conversion and separate the useful H_2 gas for fuel cell operation, as illustrated in Figure 1. Figure 2 shows the system that we designed for H_2 separation. The cermet with porous ceramic substrate tube is used for H_2 permeation. The H_2 gas will be decomposed and oxidized to protons by the metal catalysts within the cermet. The protons then diffuse through the proton conducting ceramics and are reduced to hydrogen gas by combing with the electrons at the interface between the cermet and porous ceramic tube. The driving force is the concentration difference between two sides of the cermet membrane.

The perovskite-type oxides have attracted much attention because of various possible applications in various devices, such as sensors, hydrogen pumping/separation/extraction, steam electrolysis, fuel cells etc. due to their high protonic conductivity at elevated temperature.[2-9] Among these ABO_3-type perovskite oxides, $BaCeO_3$, $SrCeO_3$, $BaZrO_3$, and $CaZrO_3$ exhibit good conduction properties under hydrogen containing atmosphere at temperature which is lower than the operating temperature of solid oxide fuel cells based on O^{2-} ion conducting ceramics.[3,10,1110,12]

However, some of these oxides, for instance $BaCeO_3$, are not stable in the CO_2 containing environment[10,12,13] because of the following reaction:

$$BaCeO_3 + CO_2 \rightarrow BaCO_3 + CeO_2$$

In contrast to $BaCeO_3$, $BaZrO_3$ is much more stable in the CO_2 containing environment.[10,12,13] But the latter oxide has a lower total proton conductivity because of high resistivity resulting from the large amount of grain boundaries observed in this ceramics.[14] Therefore, to reach both good stability and high proton conductivity, combinations of these two oxides were used in some previous studies.[10,12,13] In addition to Y-doped $BaCeO_3$[5,10,13,15] and $BaZrO_3$,[4,16-18] proton-conducting oxides doped with other transition elements, such as Gd,[11,12,18-21] Nd,[12,18,22] or Dy,[23] were also reported in literature. Our study focuses on the Gd- and Dy-doped ceramics because high conductivity was reported for these doped perovskite oxides.[12,23] The composition of our perovskite ceramics for proton conduction is $BaCe_{0.4}Zr_{0.4}Gd_{0.1}Dy_{0.1}O_{3-x}$. The cermet applied for hydrogen permeation is a combination of $BaCe_{0.4}Zr_{0.4}Gd_{0.1}Dy_{0.1}O_{3-x}$ and Pd. However, the simulation that includes both ceramics and metals is extremely difficult, so we only performed the calculation for the perovskite oxides. Furthermore, it is hard to simulate grain boundary proton conduction using the DFT method, so here we only discuss the influences of dopants on the bulk conduction property. In this work, we studied the proton diffusion in Gd- and Dy-doped barium ceria/zirconia and compared it to proton diffusion in Y-doped barium ceria/zirconia.

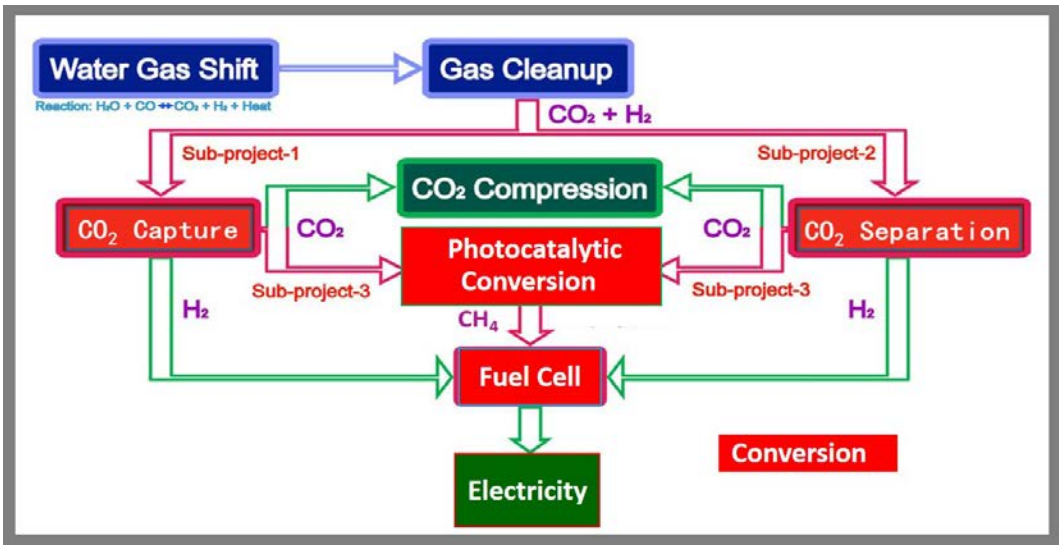

Figure 1. Illustration for the CO_2 capture/separation and fuel conversion idea.

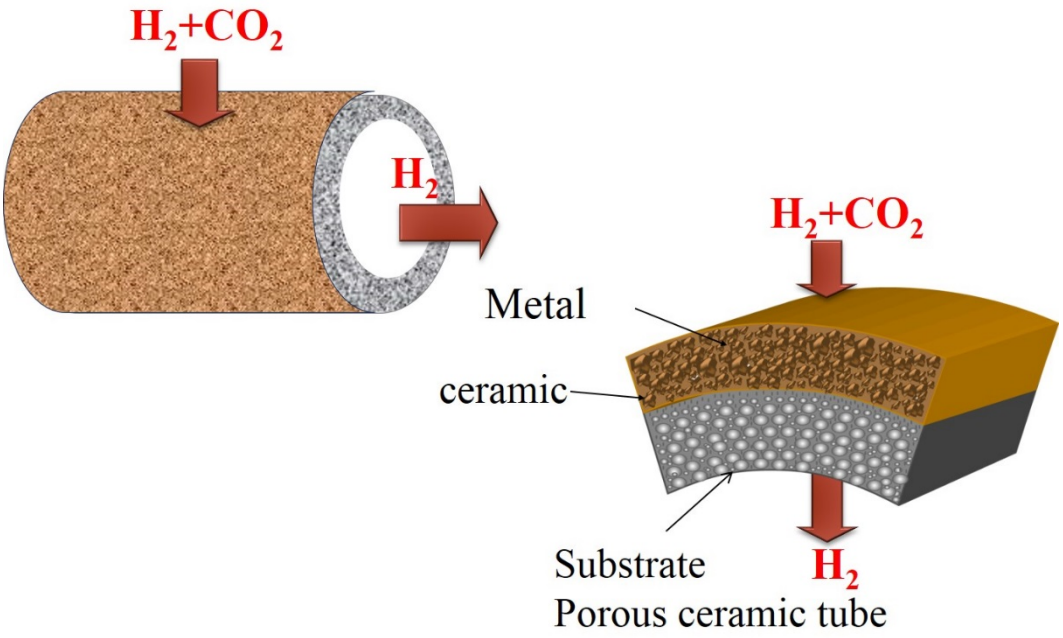

Figure 2. The design for H_2 permeation membrane.

Theoretical Methods

For our QM three dimensional periodic bulk calculation, we used Perdew−Becke−Ernzehof (PBE)[24] functional including low gradient London dispersion correction (PBE-ulg) in the generalized gradient approximation (GGA)[25,26] implemented in Vienna Ab-Initio Simulation Package (VASP)[27-29] to calculate the lattice constants and proton conduction barriers. The projector-augmented wave method was used to calculate the interaction between the core and valence electrons.[30] The reciprocal lattice is 4x4x4 Γ-centered Monkhorst−Pack grid with zero shift in our calculations. The cutoff energy for plane wave basis is 500 eV. The convergence criteria for electronic wave function and geometry optimization are $1x10^{-4}$ eV and $1x10^{-2}$ eV/Å force, respectively. For our calculation, 1x1x1 ABO_3 unit cells were used for non-doped perovskite lattice constant calculation, while 2x2x2 ABO_3 unit cells were used for doped perovskite lattice constants and proton conduction barrier calculations. Our $BaCeO_3$ and $BaZrO_3$ lattice constants are 4.47 Å and 4.26 Å, compared to experimental result 4.44 Å[31] and 4.19 Å[18], respectively (see Table 1).

$BaCe_{0.4}Zr_{0.4}Gd_{0.1}Dy_{0.1}O_{3-x}$ is not a simple stoichiometric ratio that could be constructed by a 2x2x2 cell; furthermore, there are too many possible configurations for $BaCe_{0.4}Zr_{0.4}Gd_{0.1}Dy_{0.1}O_{3-x}$ in the 2x2x2 cell. Therefore, we simplified our system to only one doped element in either cermet or zirconate (e.g. $Ba_8Ce_7GdHO_{24}$) and discussed the influence of different doping elements on proton diffusion. The hydrogen atom was placed into a position neighboring to an oxygen atom to form an OH bond, then the configuration built was computationally optimized. The optimized structures were then used as the initial and final states for a proton diffusion path in our nudged elastic band[32,33](NEB) calculation. The energy difference between the transition state found by NEB and the initial state was used as the barrier for proton diffusion along this path.

Table 1. Lattice constants comparison of barium cerate and barium zirconate.

	Calculated (Å)	Experimental (Å)
$BaCeO_3$	4.47	4.44[31]
$BaZrO_3$	4.26	4.19[18]

Table 2. Lattice constants of doped perovskites.

Composition	Lattice Constants (Å)
$BaCeO_3$ (1x1x1)	4.47
$Ba_8Ce_7YO_{24}$ (2x2x2)	8.92
$Ba_8Ce_7GdO_{24}$ (2x2x2)	8.93
$Ba_8Ce_7DyO_{24}$ (2x2x2)	8.92
$BaZrO_3$ (1x1x1)	4.26
$Ba_8Zr_7YO_{24}$ (2x2x2)	8.55
$Ba_8Zr_7GdO_{24}$ (2x2x2)	8.56
$Ba_8Zr_7DyO_{24}$ (2x2x2)	8.55

Results and Discussion

The lattice constants for $Ba_8X_7MHO_{24}$ (X=Ce or Zr, M=Y, Gd, Dy), are listed in Table 2. Doping does not significantly change the lattice constants compared to those for the undoped oxides.

In $Ba_8X_7MHO_{24}$ (X=Ce, Zr; M=Y, Gd, Dy), there are five various conduction paths for the proton transfer from one oxygen atom to another. These paths are shown in Figure 3. In path 1, the proton migrates along an edge of a ZrO_6-octahedron in the Zr-OH-Y configuration. The path 2 describes a similar proton transfer but in the Zr-OH-Zr configuration. Path 3 describes the intra-YO_6-octahedron proton transfer. Path 4 and 5 are inter-octahedra proton transfers between a ZrO_6 octahedron and YO_6 octahedron and two ZrO_6 octahedra, respectively. Complete proton diffusion paths may be composed from combination of paths 1-5 in which the proton returns to the geometrically equivalent position in our three dimension periodic cell. For example, a proton conduction route composed by paths 1→3→3→1 is a complete route because the proton attached to the crystallographically equivalent oxygen atom as shown in Figure 4. If we used the Boltzmann population ($F_{state} \propto e^{-E/kT}$) of the initial state energy of each path to determine the probability for proton to occupy a certain site at $700^{O}C$, the probability for the proton at the initial site of path 1, 2, 3, 4 is 0.246; whereas for path 5 it is only 0.014. Therefore, it is practically impossible for the proton to use path 5. The energy barriers for different proton transfer paths in Y-doped $BaZrO_3$ are tabulated in Table 3. Our NEB calculation also shows that the OH bond reorientation has 0.07 eV energy difference in the last two steps, which is comparable with the earlier reported value of 0.02 eV.[2]

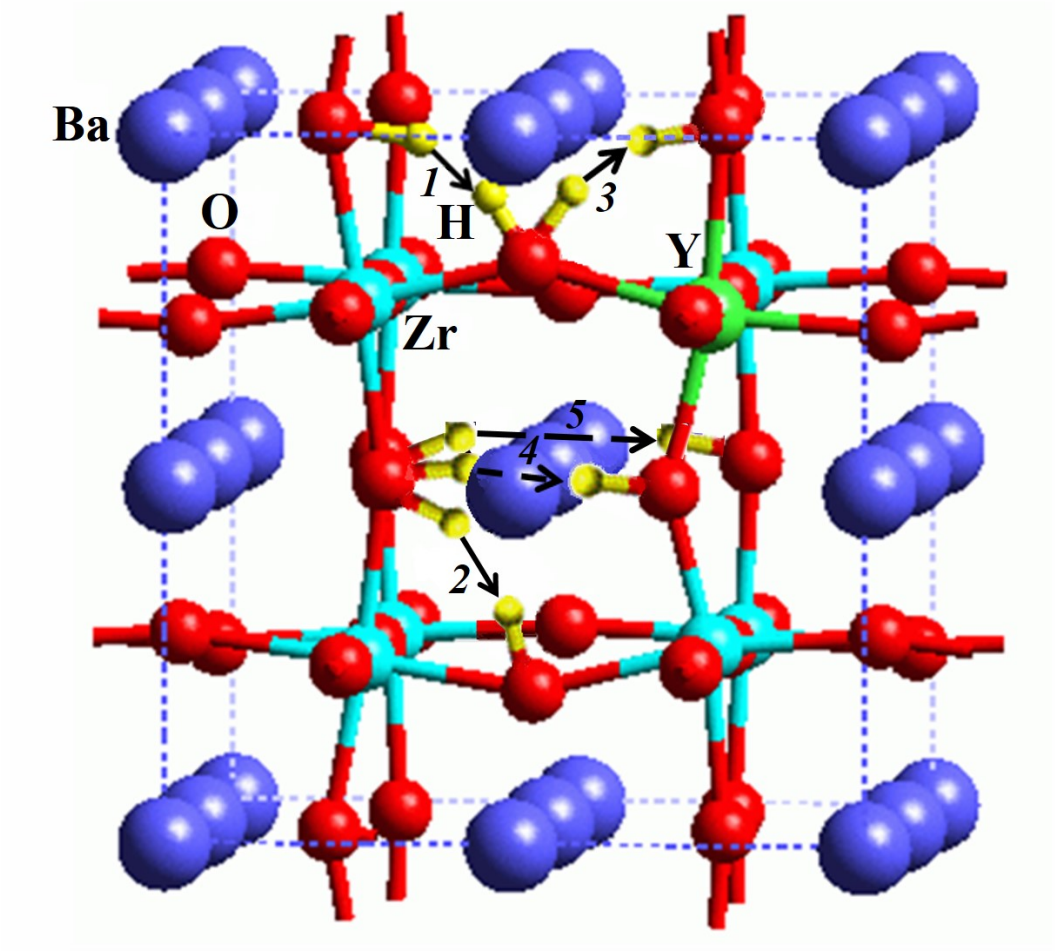

Figure 3. The proton conduction path in $Ba_8Zr_7YHO_{24}$ cell (copied and revised from Ref. 17).

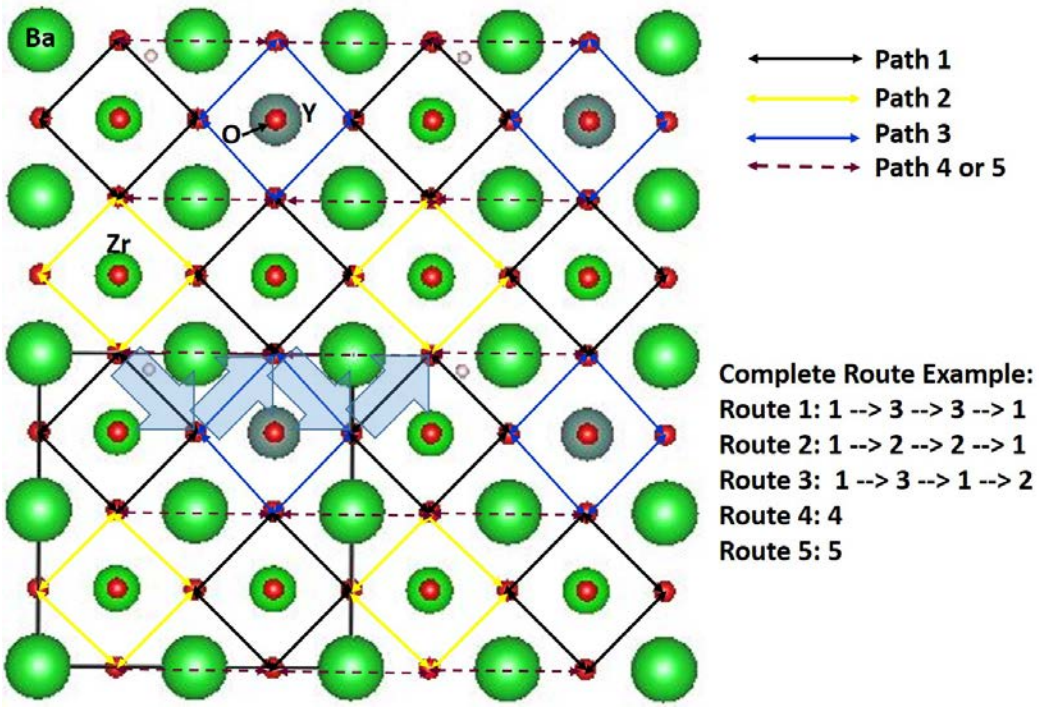

Figure 4. The proton conduction route example in $Ba_8Zr_7YHO_{24}$ cell.

Table 3. The relative energy corresponding to each step of various proton conduction paths in $Ba_8Zr_7YHO_{24}$.

Step\Path*	Path_1	Path_2	Path_3	Path_4	Path_5
0	0.00	0.00	0.00	0.00	0.00
1	0.22	0.21	0.07	0.09	0.06
2	0.04	0.29	0.19	0.05	0.30
3	0.24	0.13	0.32	0.11	0.08
4	0.19	0.44	0.19	0.26	0.08
5	0.07	0.11	0.07	0.05	0.08
6	0.00	0.00	0.00	0.00	0.03
barrier	**0.24**	**0.44**	**0.32**	**0.26**	**0.30**

*All energies are relative to “step 0” (initial state) energy of each path.

It was also found in our calculation that instead of the inter-octahedra proton transfer (path 4 and 5), we got two successive intra-octahedron proton transfers, as illustrated in Figure 5. Figure 6 shows

the potential energy surface of proton transfer in doped cerates with fixed donor oxygen and acceptor oxygen distances. We plot the energy versus the distance between the proton and donor oxygen atoms of barium ceria doped with Dy, Gd, and Y. As expected, the proton transfer barrier is proportional to the donor oxygen–acceptor oxygen distance. For 2.46 Å, the barrier is about 0.1 eV, while for 2.69 Å, the barrier is about 0.45 eV. The Gd-doped barium ceria has the slightly lower barrier than the Y- and Dy-doped analogues, which is in agreement with the reported higher proton conductivity of the Gd-doped $BaCeO_3$ oxide.[12]

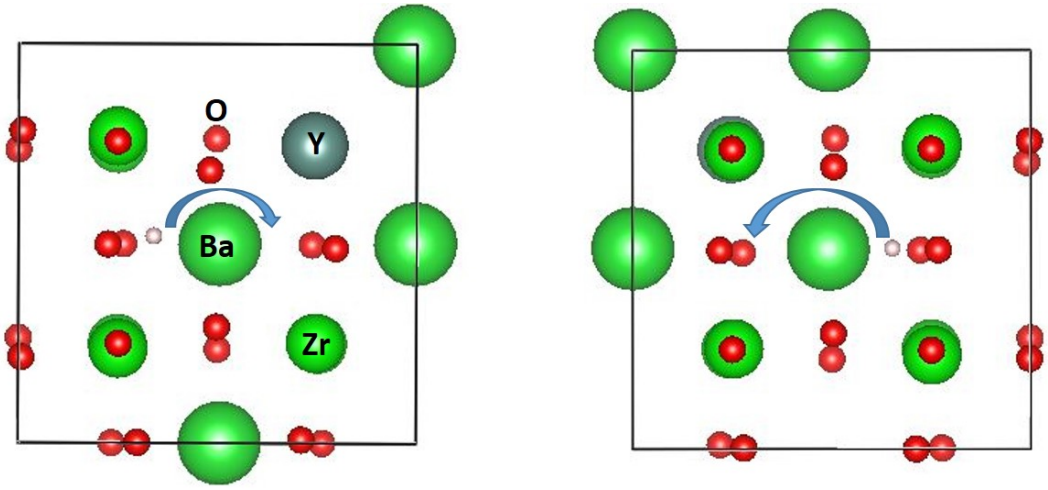

Figure 5. The calculated successive intra-octahedra proton transfer path in our $Ba_8Zr_7YHO_{24}$ cell.

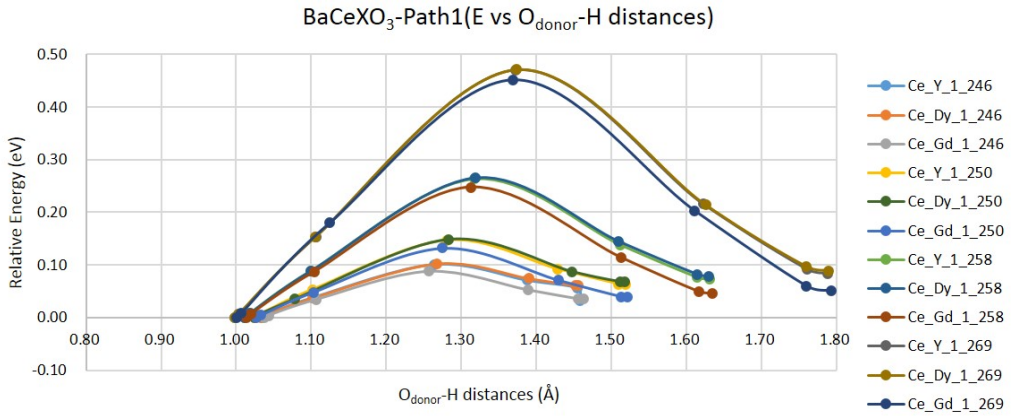

Figure 6. The energy versus O_{donor}-H distance of doped cerates with different fixed O_{donor}-$O_{acceptor}$ distance.

As for doped barium zirconates, the Y-doped sample seems to have the slightly lower proton diffusion barrier than the Gd- and Dy-doped zirconates. As the distance between the donor and acceptor oxygen atoms increases to ~2.69 Å, the proton diffusion barrier value becomes similar to the experimentally reported activation energy of 0.44 eV.[16] Furthermore, the doped zirconates have similar proton conductivity values. This is probably because our calculations consider only the bulk diffusion and do not include the proton diffusion through grain boundaries. Generally, the proton diffusion barriers for all materials studied here are very similar and it is hard to make conclusions about differences in this property based only on our calculation results. Therefore, more proper calculations, for example reactive force field molecular dynamics that will include both grain and grain boundary simulations are needed to get better insights in the problem we studied.

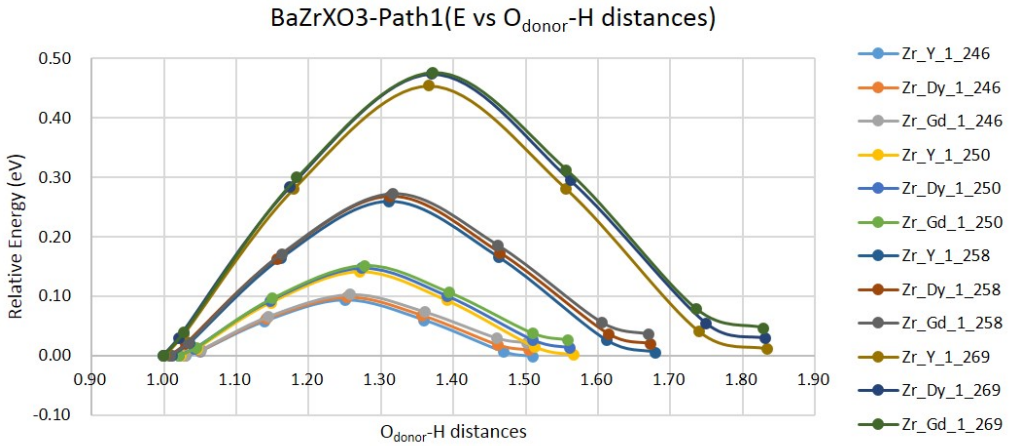

Figure 7. The energy versus O_{donor}-H distance of doped zirconates with different fixed O_{donor}-$O_{acceptor}$ distance.

Conclusions

Doped $BaCeO_3$ oxides have the highest total proton conductivity among the proton-conducting perovskite oxides, but in the CO_2 containing environment these materials react with CO_2 to form barium carbonates and ceria. To improve their chemical stability, mixtures with some barium zirconates might be used to reach a compromise between stability and conductivity. Our DFT calculation simulate the lattice constants close to the experimental values. We discussed possible proton transfer route for $Ba_8X_7(OH)_1MO_{23}$ (X=Ce or Zr, M=Y, Gd, Dy), and find that the proton transfer via path 5 is not preferable because of its high initial state energy. According to our calculation, inter-octahedra proton transfer paths 4 and 5 were substituted by two successive intra-octahedron proton transfers.

For fixed donor oxygen–acceptor oxygen distance calculations, the Gd-doped barium cerium oxides have the slightly lower proton transfer (0.02~0.03 eV) barrier than Y- and Dy-doped barium cerium oxides, while among the zirconate analoges, Y-doped $BaZrO_3$ has the lower energy barrier (0.02~0.03 eV) than the other two. The doped zirconates have the barrier value similar to the experimental value of the activation energy when the distance between the donor oxygen and acceptor oxygen is ~2.69 Å. Generally, from our calculations the doped cerates and zirconates have similar bulk proton diffusion barriers and more comprehensive work including the grain boundary proton diffusion simulations by ReaxFF reactive dynamics will be trained based on our QM results.

BIBLIOGRAPHY

[1] Frey, H. C.; Zhu, Y. Environ. Sci. Technol. 2006, 40, 1693-1699.

[2] Gomez, M. A.; Griffin, M. A.; Jindal, S.; Rule, K. D.; Cooper, V. R. *J. Chem. Phys.* **2005**, *123*, 094703.

[3] Schober, T. *Solid State Ionics* **2003**, *162*, 277-281.

[4] Gomez, M. A.; Chunduru, M.; Chigweshe, L.; Foster, L.; Fensin, S.; Fletcher, K. M.; Fernandez, L. E. *J. Chem. Phys.* **2010**, *132*, 214709.

[5] Guan, J.; Dorris, S.; Balachandran, U.; Liu, M. *Solid State Ionics* **1997**, *100*, 45-52.

[6] Zhu, Z.; Sun, W.; Yan, L.; Liu, W.; Liu, W. *Int. J. Hydrogen Energy* **2011**, *36*, 6337-6342.

[7] Iwahara, H. *Solid State Ionics* **1996**, *86*, 9-15.

[8] Iwahara, H.; Asakura, Y.; Katahira, K.; Tanaka, M. *Solid State Ionics* **2004**, *168*, 299-310.

[9] Iwahara, H. *Solid State Ionics* **1995**, *77*, 289-298.

[10] Katahira, K.; Kohchi, Y.; Shimura, T.; Iwahara, H. *Solid State Ionics* **2000**, *138*, 91-98.

[11] Gomez, M. A.; Chunduru, M.; Chigweshe, L.; Foster, L.; Fensin, S.; Fletcher, K. M.; Fernandez, L. E. *J. Chem. Phys.* **2010**, *132*, 214709.

[12] Ryu, K. H.; Haile, S. M. *Solid State Ionics* **1999**, *125*, 355-367.

[13] Fabbri, E.; D'Epifanio, A.; Di Bartolomeo, E.; Licoccia, S.; Traversa, E. *Solid State Ionics* **2008**, *179*, 558-564.

[14] Tao, S.; Irvine, J. T. *Adv. Mater.* **2006**, *18*, 1581-1584.

[15] Xie, K.; Yan, R.; Liu, X. *J. Alloys Compd.* **2009**, *479*, L40-L42.

[16] Bohn, H. G.; Schober, T. *J. Am. Ceram. Soc.* **2000**, *83*, 768-772.

[17] Merinov, B.; Goddard III, W. A. *J. Chem. Phys.* **2009**, *130*, 194707. 214709.

[18] Sundell, P. G.; Björketun, M. E.; Wahnström, G. *Phys. Rev. B* **2006**, *73*, 104112.

[19] Zając, W.; Rusinek, D.; Zheng, K.; Molenda, J. *Cent. Eur. J. Chem.* **2013**, *11*, 471-484.

[20] Hermet, J.; Torrent, M.; Bottin, F.; Dezanneau, G.; Geneste, G. *Phys. Rev. B* **2013**, *87*, 104303.

[21] Kreuer, K.; Schönherr, E.; Maier, J. *Solid State Ionics* **1994**, *70*, 278-284.

[22] Iwahara, H.; Uchida, H.; Ogaki, K.; Nagato, H. *J. Electrochem. Soc.* **1991**, *138*, 295-299.

[23] Wang, W.; Liu, J.; Li, Y.; Wang, H.; Zhang, F.; Ma, G. *Solid State Ionics* **2010**, *181*, 667-671.

[24] Perdew, J. P.; Burke, K.; Ernzerhof, M. *Phys. Rev. Lett.* **1996**, *77*, 3865-3868.

[25] Perdew, J. P.; Zunger, A. *Phys. Rev. B* **1981**, *23*, 5048-5079.

[26] Ceperley, D. M.; Alder, B. J. *Phys. Rev. Lett.* **1980**, *45*, 566-569.

[27] Kresse, G.; Hafner, J. *Physical Review B* **1993**, *47*, 558.

[28] Kresse, G.; Furthmüller, J. *Comput. Mater. Sci.* **1996**, *6*, 15-50.

[29] Kresse, G.; Furthmüller, J. *Phys. Rev. B* **1996**, *54*, 11169.

[30] Kresse, G.; Joubert, D. *Phys. Rev. B* **1999**, *59*, 1758.

[31] Knight, K. *Solid State Ionics* **1994**, *74*, 109-117.

[32] Mills, G.; Jonsson, H. *Phys. Rev. Lett.* **1994**, *72*, 1124-1127.

[33] Mills, G.; Jonsson, H.; Schenter, G. K. *Surf. Sci.* **1995**, *324*, 305-337.